AIAA SciTech Forum
12-16 January 2026, Orlando, FL
AIAA SCITECH 2026 Forum

10.2514/6.2026-0672

Recent Developments and Applications of Molecular Tagging Velocimetry for High-Speed Flow Measurements

Douglas W. Carter*
Illinois Institute of Technology, Chicago, IL 60616 USA
Sandia National Laboratories, Albuquerque, NM 87123 USA

Mark Gragston†
The University of Tennessee-Knoxville, Knoxville, TN 37996 USA
The University of Tennessee Space Institute, Tullahoma, TN 37388 USA

Boris S. Leonov ‡
Texas A&M University, College Station, TX, 77843 USA

Nicholaus J. Parziale§
Stevens Institute of Technology, Hoboken, NJ 07030, USA

Neil S. Rodrigues¶
NASA Langley Research Center, Hampton, VA 23681 USA

This document provides a detailed discussion of various aspects of molecular tagging velocimetry (MTV), with a particular focus on applications to high-speed flow measurements. The discussion includes details on photophysics for the most common tracers, approaches and considerations for performing MTV measurements, and techniques for reducing experimental data for extracting velocity and secondary quantities. Examples are also provided to demonstrate the successes of MTV in high-speed flow measurements, before highlighting current challenges and limitations of the diagnostic technique.

Contents

*Assistant Professor, Department of Mechanical, Materials, and Aerospace Engineering, AIAA Member
†Assistant Professor, Mechanical and Aerospace Engineering, AIAA Senior Member
‡Research Assistant Professor, Department of Aerospace Engineering, AIAA Member.
§George Meade Bond Professor, Mechanical Engineering, AIAA Associate Fellow.
¶Optical Physicist, Advanced Measurements and Data Systems Branch, AIAA Senior Member.

I. Introduction

Velocity and associated transport parameters, such as vorticity, are key variables for the characterization of fluid flow and have spurred the development of various velocimetry techniques throughout the historical study of fluid dynamics. Enabled by the development of advanced light sources and detection capabilities, non-intrusive methods were also developed to provide high-quality data or information in regions where traditional probes could not be used. Particle image velocimetry (PIV) is perhaps the most common example of a non-intrusive velocimetry technique, and is typically the standard approach to velocimetry for most aerospace environments.

However, significant interest in high-speed flows in recent years, largely fueled by interests pertaining to the development of hypersonic flight capabilities, has increased the demand for high quality measurements and data, including velocimetry, to support the development and validation of computational modeling capabilities (*e.g.*, RANS turbulence models). For such flow fields, it has been shown that PIV and other particle seeding techniques are limited in utility. Experiments by Brooks *et al.* [1] looking at fluctuations in a Mach 3 turbulent boundary layer showed that particle lag effects caused substantial variations in the measured fluctuations of the wall-normal component of velocity. Thus, even at Mach 3 there could be issues with trusting PIV to provide important information about local turbulent kinetic energy and Reynolds stress values, which are key pieces of information for developing approaches to scale production and dissipation terms in RANS turbulence models. In total, Brooks [2] was able to show that the particle lag effects in PIV effectively acted as a low-pass filter for turbulent supersonic flows. This lag effect has also been observed across shockwaves, resulting in a particle slip with respect to the local flow, strong non-uniformity of particle seeding distribution, and particle-image blurring [3]. These issues were also explored via computational means by Aultman *et al.* [4] using DNS to generate synthetic PIV data. Those results showed that wall-normal velocity fluctuations were sensitive to particle lag effects and that the interrogation window sizes used in the cross-correlation portion of PIV data processing significantly affected all determined Reynolds stress components for the Mach 4.9 turbulent boundary layer when compared to the baseline DNS used to generate the synthetic data. While these results show the limitation of PIV for high-speed flow velocity measurements, additional aspects to consider include the difficulty in seeding particles into hypersonic wind tunnels (many of which are impulse facilities), the potential for particles to slowly degrade surfaces (model and tunnel), and the possibility that particles will occlude viewports/windows given the relatively high freestream velocities.

To avoid many of the issues with PIV, many researchers have begun to use molecular tagging velocimetry (MTV), which is a technique that uses intense light to excite natural or seeded molecular species in a gaseous flow and determines local velocity by tracking the displacement of the emitting molecules. MTV dates back to the late 1960s with experiments focused on liquid flows [5], but only after the development of better light sources (*e.g.*, commercially available high-power lasers) and imaging technology (*e.g.*, high-speed intensified cameras), MTV became usable in the much less dense gaseous flows in high-speed wind tunnels. For instance, as early as 1977, in his paper on quantitative density visualization, Epstein discussed the potential to use fluorescence from seeded species to "crudely" measure the

velocity in a gaseous flow following a description very similar to the one stated above for MTV [6]. However, to the best of our knowledge, this was not implemented experimentally until 1984 when Hiller *et al.* demonstrated the first MTV in a gas seeded with biacetyl [7]. Only a few years later, in 1987 and 1989, Miles *et al.* first demonstrated MTV in unseeded air (RELIEF) and then presented the first MTV measurement in high-speed flow (Mach 4), marking the beginning of the subject of this review [8, 9]. Despite decades of development, MTV in high-speed flows is continuously evolving, fueled by the new technological capabilities of lasers and detectors, as well as by the ever-growing demands and requirements of the high-speed aerodynamics community. Though generally more complicated in setup compared to PIV, MTV has no known lag effects in most flows since the tracers are the molecules comprising the fluid instead of macroscale particles, which also implies MTV does not have any appreciable filtering effects (beyond the averaging associated with the convection distance between imaging frames). Furthermore, the seeding of gaseous tracer molecules can be done for various kinds of high-speed tunnels (blowdown tunnels, Ludwieg tubes, shock tunnels, expansion tunnels, etc.) and in some cases naturally occurring species can be targeted (*e.g.*, molecular nitrogen or nitric oxide).

Thus, inspired by the need for better velocimetry capabilities for high-speed flows and the appropriateness of molecular tagging velocimetry for these conditions, this document aims to provide a detailed review of common MTV target species for high-speed flows, experimental setup and data collection considerations, details surrounding data processing, including error estimation, and more. The authors acknowledge that many more molecular tagging techniques exist in literature, which target other species (*e.g.*, iodine, ozone, oxygen, sodium, and imidogen) or use unique photophysical processes to target species discussed in this section, as presented in the following few references [10–17]. However, species and methods discussed here were chosen considering modern usage, prevalence in high-speed flow literature, practicality, and simplicity.

II. Common MTV Target Species

In this section, relatively common target gases used in molecular tagging velocimetry in high-speed flows are discussed along with the associated photophysics.

A. Krypton - Kr

Krypton Tagging Velocimetry (KTV) is a tagging velocimetry technique ('atomic' rather than 'molecular') where Kr atoms are seeded into a flow of interest, tagged via laser excitation, and tracked. KTV uses a nominally chemically inert tracer, metastable or ionized Kr, so the signal is largely decoupled from the flow chemistry. Unlike many conventional tracers, krypton is chemically inert, which makes the method adaptable to environments where composition evolves or is hard to predict, including combustion and nonequilibrium gas dynamics. The atomic structure of Kr is well characterized, and the relevant two-photon transitions are reachable with standard, commercially available lasers and optics, lowering implementation barriers [18–21].

KTV was originally conceived as a scheme that required two pulsed dye lasers [20] via excitation at 214.7 nm (Fig. 1b). Later work demonstrated that KTV could be executed with a simple solid-state continuous-wave (CW) read laser, or eliminating the read laser altogether [22–24]. The choice between a single or dual laser setup and excitation wavelength is setup dependent. If one is only using a single laser, then the (2+1) resonantly-enhanced multiphoton ionization (REMPI) process at 212.556 nm is likely the best option (Fig. 1a). If one has a tunable laser near 769 nm, then excitation at 216.667 nm and re-excitation from the metastable state at 769.454 nm might be the best option (Fig. 1c). The re-excitation laser is more valuable at lower pressures where the metastable state of Kr is quenched at a reduced rate. For more discussion, see Shekhtman [24] and Shekhtman et al. [25].

In application, the seeding concentration of krypton is usually a few percent by partial pressure. Since krypton is an atomic species, it has thermodynamic properties that are quite different from the values for air. Figure 2 shows the impact that krypton has on the specific heat ratio and the speed of sound when mixed with air at room temperature. Clearly, the small partial pressures of Kr typically used in KTV do not alter these quantities in any meaningful way.

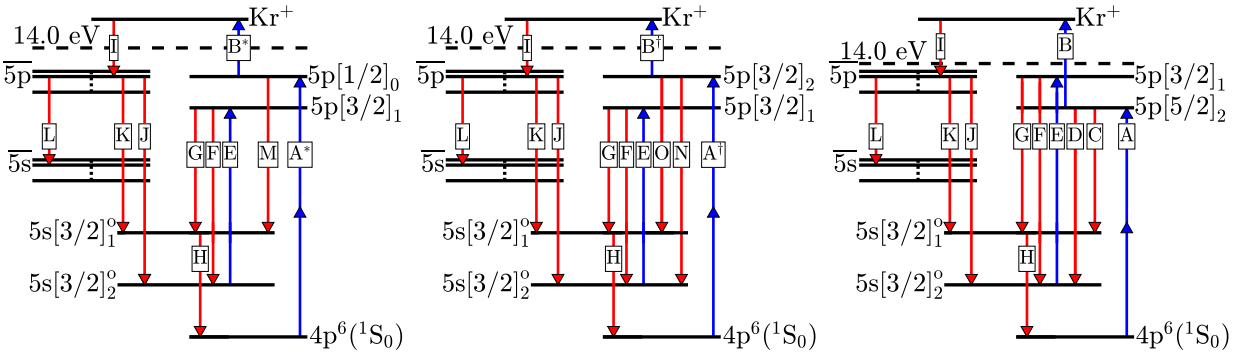

(a) 212.556 nm Excitation **(b) 214.767 nm Excitation** **(c) 216.667 nm Excitation**

Fig. 1 Energy diagrams (not to scale) with Racah nl[K]$_J$ notation for the three excitation schemes. (a) 212.556 nm. (b) 214.769 nm. (c) 216.667 nm. Transition details are in Table 1. States $\overline{5p}$ and $\overline{5s}$ represent the numerous 5p and 5s states that are created by the recombination process, I. Transitions J, K and L represent the numerous transitions in the 5p-5s band. 14.0 eV marks the ionization limit of Kr. From Shekhtman [24] with permission.

Table 1 Relevant NIST Atomic Spectra Database Lines Data [26] with labels matching Fig. 1. Racah nl[K]$_J$ notation. Transition I is not listed because it represents the recombination process. Transitions J/K/L, which represent numerous transitions in the 5p-5s band, have ranges and order of magnitude estimates as entries. Subscripts i and j denote the upper and lower energy levels respectively. From Shekhtman [24] with permission.

Transition	λ_{air} (nm)	Nature	Lower Level	Upper Level	A_{ij} (1/s)	E_j (cm^{-1})	E_i (cm^{-1})
A	216.670	Two-Photon	$4s^24p^6$, $^1S_0$	$5p[5/2]_2$	(-)	0	92307.3786
A†	214.769	Two-Photon	$4s^24p^6$, $^1S_0$	$5p[3/2]_2$	(-)	0	93123.3409
A*	212.556	Two-Photon	$4s^24p^6$, $^1S_0$	$5p[1/2]_0$	(-)	0	94092.8626
B	216.667	Single-Photon	$5p[5/2]_2$	Kr+	(-)	92307.3786	112917.62
B†	214.769	Single-Photon	$5p[3/2]_2$	Kr+	(-)	93123.3409	112917.62
B*	212.556	Single-Photon	$5p[1/2]_0$	Kr+	(-)	94092.8626	112917.62
C	877.675	Single-Photon	$5s[3/2]_1$	$5p[5/2]_2$	2.2×10^7	80916.7680	92307.3786
D	810.436	Single-Photon	$5s[3/2]_2$	$5p[5/2]_2$	8.9×10^6	79971.7417	92307.3786
E/F	769.454	Single-Photon	$5s[3/2]_2$	$5p[3/2]_1$	4.3×10^6	79971.7417	92964.3943
G	829.811	Single-Photon	$5s[3/2]_1$	$5p[3/2]_1$	2.9×10^7	80916.7680	92964.3943
H	123.584	Single-Photon	$4s^24p^6$, $^1S_0$	$5s[3/2]_1$	3.0×10^8	0	80916.7680
J/K/L	750-830	Single-Photon	$\overline{5s}$	$\overline{5p}$	$10^6 - 10^7$	80000.0000	90000.0000
M	758.950	Single-Photon	$5s[3/2]_1$	$5p[1/2]_0$	4.31×10^7	80916.7680	94092.8626
N	760.364	Single-Photon	$5s[3/2]_2$	$5p[3/2]_2$	2.732×10^7	79971.7417	93123.3409
O	819.230	Single-Photon	$5s[3/2]_1$	$5p[3/2]_2$	1.1×10^7	80916.7680	93123.3409

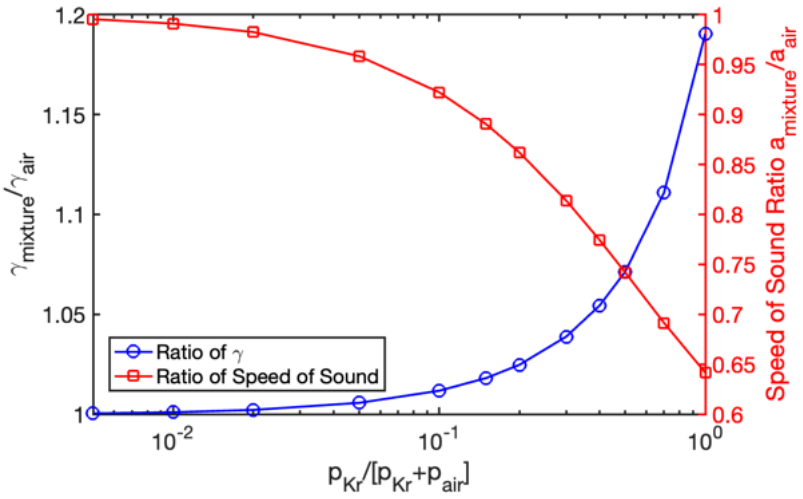

Fig. 2 A plot showing the effect krypton has on the specific heat ratio γ and the isentropic speed of sound based on the relative pressure of Kr to absolute static pressure. Note the horizontal axis is equivalent to krypton mole fraction. Calculations are for room temperature.

B. Molecular Nitrogen - N_2

Femtosecond and picosecond lasers may be used to tag molecular nitrogen by focusing the laser beam to a point or a line to create a tagged "filament" of weakly ionized plasma. The key aspect of tagging nitrogen is the short time-scale of the laser which produces multiphoton nonresonant excitation without the generation of a laser spark that is observed in nanosecond lasers. This technique is known as femtosecond laser electronic excitation tagging (FLEET) or, if using a picosecond laser, PLEET. The former is generally favored over the latter for the reduced perturbation of the gas. FLEET was invented nearly fifteen years ago [27] and has since seen a rise in popularity owing to many of its attractive properties [28]. Unlike other MTV techniques, FLEET does not require tuning to a specific frequency band which greatly simplifies its implementation. Since FLEET typically targets nitrogen, and nitrogen is the most common gas on earth, it generally does not require any special seeding and is therefore widely applicable.

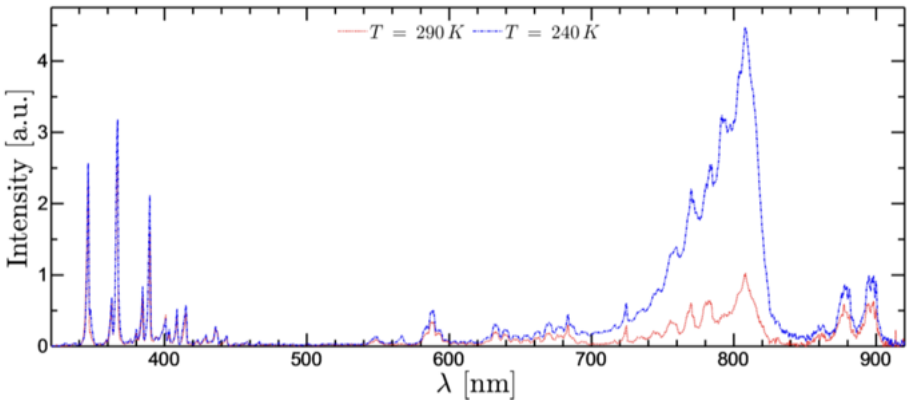

Fig. 3 Typical calibrated emission spectra of FLEET excitation in nitrogen at two temperatures [29]. Adapted from [29]. Work of the U.S. Government.

The physical process by which FLEET occurs is not fully understood. Discussion regarding the underlying process of excitation and photoemission is available in the literature [28, 30–32] and the hypothetical process will be briefly summarized here. The molecular nitrogen experiences dissociation, ionization and electronic excitation due to the incoming photons of the focused femtosecond laser beam. The recombination is delayed to high energy levels and

eventually returns to the molecular ground state during which photons are emitted. Fluorescence of the nitrogen originates from the first positive $N_2(B^3\Pi_g) \rightarrow N_2(A^3\Sigma_u^+) + h\nu$, first negative $N_2^+(B^2\Sigma_u^+) \rightarrow N_2^+(X^2\Sigma_g^+) + h\nu$, and second positive systems $N_2(C^3\Pi_u) \rightarrow N_2(B^3\Pi_g) + h\nu$. The first negative and second positive systems occur rapidly (sub-microsecond), whereas the first positive system (from B to A states) has the longest lifetime on the order of microseconds and emits in the yellow-red portion of the visible spectrum. A typical emission spectrum is shown in Fig. 3. The rate-limited first positive system is the long-lasting fluorescence that enables FLEET velocimetry. The temporal fluorescence decay has a bi-exponential behavior, with short and long time-scales whose precise value depends on the composition and thermodynamic state of the test gas [27]. The FLEET signal is greater in pure nitrogen than air. In air, the excitation is quenched by the presence of molecular oxygen [32, 33] and the signal-to-noise ratio decreases by approximately one order of magnitude. It is important to note that the ionization (and the generated shock) is relatively weak compared to, for example, the laser spark (and shock) associated with cascade ionization induced by nanosecond lasers. This key feature is because the femtosecond pulse is on the order of the time scale for an electron to separate from its ionized source [34] and makes FLEET an attractive option for MTV.

There are several options for the selection of a laser for FLEET. Two popular choices are regeneratively amplified Ti:Sapphire (*e.g.*, the Solstice Ace from Spectra Physics) lasers [35–37] which emit at a fundamental wavelength of 800 nm, and more recently Yb:KGW (*e.g.*, the PHAROS by Light Conversion) lasers [38] that are centered at 1030 nm. In the case of PLEET, the fundamental output of a Nd:YAG system has been used at 1064 nm [39]. At larger wavelengths the number of photons required to achieve excitation is greater than at shorter wavelengths; therefore, frequency doubling, tripling, and quadrupling has been explored using beta barium borate crystals (BBO) to achieve the desired fluorescence with minimized gas disturbance [40–42]. In the case of a Ti:Sapphire laser, this corresponds to a doubling at 400 nm, tripling at 267 nm, and quadrupling at 202.25 nm. The quadrupling is known as selective two-phase absorptive resonance FLEET (STARFLEET) [40], and although it minimizes the required energy (and has an entertaining acronym) it has practical difficulties for implementation due to the sensitivity of the optical setup. For the best compromise of minimal disturbance and simple optical implementation, the frequency-tripled 267 nm is recommended. Frequency doubled, tripled, and further harmonics of Yb:KGW lasers are commercially available, but an exploration of their performance for FLEET is currently lacking. However, these lasers do have the advantage of pulsing rates up to 50 kHz or more (compared to the 1-10 kHz of Ti:Sapphire lasers) and have recently found success in identifying the frequency content of an underexpanded jet [38]. Nevertheless, the pulse energy at 50 kHz for commercially available Yb:KGW lasers range is currently relatively low at 0.2-0.4 mJ and it remains to be seen whether successful measurements can be made at large-scale facilities, which often require longer focal lengths.

C. Nitric Oxide - NO

Nitric oxide (NO) is one of the common molecular tracers utilized for measurements in high-speed flow environments [43]. A few features of nitric oxide make it an attractive choice for the research community. First, nitric oxide is naturally formed in air at elevated temperatures exceeding 1800 K, with an equilibrium mole fraction near 4% at 3300 K and atmospheric pressure [44]. Hence, it is present in the freestream of many types of ground testing facilities, such as shock tunnels, and is formed near test bodies and behind shock waves in medium to high enthalpy flows produced by expansion tunnels [45–47]. Second, in cases when NO is not naturally formed, it can be seeded externally due to its relative stability without long-term exposure to oxygen, which makes it a viable option for low-enthalpy applications, please see Sec. VI.A for more details on gas seeding [48]. Since NO is a diatomic molecule, such external seeding does not impact the resulting test gas ratio of specific heats for air or nitrogen flows, $\gamma = 1.4$ at STP. Additionally, nitric oxide possesses a very similar molecular mass and diffusivity to nitrogen and oxygen and tends to avoid stratification due to buoyancy. Third, a single photon electronic excitation in the γ ($A^2\Sigma^+ \leftarrow X^2\Pi$) band is routinely done at a broad range of wavelengths near 226 nm with either a dye laser or an Optical Parametric Oscillator (OPO) based laser source. Furthermore, it was recently demonstrated that both γ and β ($B^2\Pi \leftarrow X^2\Pi$) transitions of nitric oxide conveniently overlap with the 5th harmonic output of an Nd:YAG laser near 213 nm [49, 50]. Absorption spectra for nitric oxide generated with LIFBASE, the open-access software [51], are shown in Fig. 4(a). These features make nitric oxide a convenient and readily accessible option for many laser diagnostic applications, including molecular tagging velocimetry. The typical amount of nitric oxide required for MTV applications in high-speed flows does not exceed a few percent by volume, with some cases demonstrating NO-MTV with only a few hundred parts-per-million (PPM) of NO in air and nitrogen flows [52, 53].

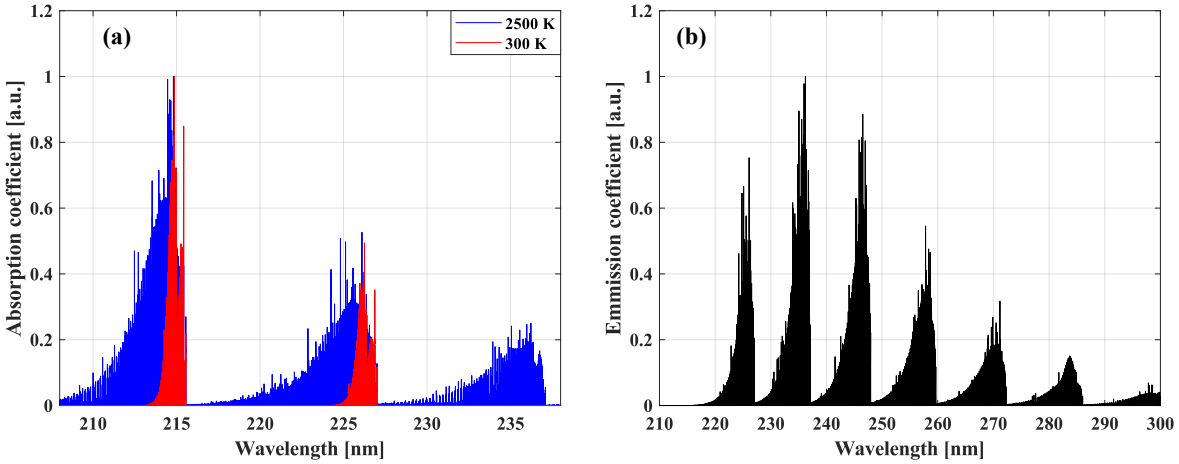

Fig. 4 Nitric oxide γ ($A^2\Sigma^+ \leftrightarrow X^2\Pi$) electronic transition spectra from LIFBASE: (a) absorption spectra at different temperatures; (b) emission spectra after the most common 226 nm excitation.

The first demonstration of molecular tagging velocimetry with nitric oxide was reported more than 20 years ago in 2003 by Danehy *et al.* [54]. In this work, the authors used a frequency-doubled excimer-pumped dye laser to excite a line of naturally formed nitric oxide within the boundary layer in a hypersonic flow at 226 nm and observed the NO fluorescence over a few hundred nanoseconds as the flow convects the excited molecules downstream from the laser beam line. One of the significant demonstrated advancements was the simplicity of the experimental setup. It relied on a single nanosecond tunable laser to "write" a pattern in the flow and a single intensified camera to observe it over time, while the vast majority of flow tagging techniques at the time required either two or three independently tunable and delayable laser systems to effectively "write" and subsequently "read" the tagged pattern [9]. After the initial electronic excitation, as the tagged molecules are convected by the flow, they emit photons in the identical spectral region as normal nitric oxide planar laser-induced fluorescence through electronic de-excitation into different vibrational and rotational states of the ground electronic state ($X^2\Pi$). Examples of emission spectra from electronically excited nitric oxide can be found in the following references [49, 50, 55] or simulated by LIFBASE, as shown in Fig. 4(b). The NO-MTV signal is typically collected in the "red-shifted" spectral region, 230 nm - 270 nm, by an intensified camera with a varying temporal delay with respect to the laser pulse. However, such emission brings an inherent drawback to the single-photon NO-MTV method: short fluorescence lifetime. The NO-MTV signal lifetime, τ_{NO-MTV}, the time it takes for the signal intensity to drop to $\frac{1}{e} \approx 0.37$ of its original level through exponential decay, is limited by the upper electronic state depopulation mechanisms, which are primarily dominated by spontaneous emission and collisional quenching. It can be approximated as shown in Eq. 1:

$$\tau_{NO-MTV} = \frac{1}{\sum_{v"} \mathcal{A}_{v'v"} + Q}, \tag{1}$$

where $\sum_{v"} \mathcal{A}_{v'v"} = 4.95 \times 10^6\ s^{-1}$ is a spontaneous emission coefficient summation [56] and $Q\ [s^{-1}]$ is a collisional quenching rate summation over all species present [57]. Considering the above, NO MTV lifetime cannot exceed 200 ns even in a low-pressure inert environment, and decreases to only a few nanoseconds for high-enthalpy hypersonic air flows [47]. Such a short signal lifetime typically prohibits NO-MTV utilization in reacting environments, prevents combining two intensifier gates on a single camera image due to tagged line overlap or blurring, and keeps the temporal camera image spacing at relatively short values of $\leq$ 500 ns in colder flows. This also prevents observing the tagged flow over spatially extended regions and dictates "writing" multi-line patterns to spatially cover the flow-field, unlike other long-fluorescence MTV alternatives.

Despite this limitation, NO-MTV received widespread utilization over the years with a multitude of examples across the aerospace industry with ever-increasing number of tagging laser beams and repetition rates to improve our understanding of the interrogated flow-field spatial and temporal morphology, respectively. For instance, Inman *et al.* used a microlens array to generate 25 NO-MTV lines produced by a 10 Hz Nd:YAG-pumped dye laser with 2 mm spacing to measure axial velocity in the HYMETS arcjet facility upstream of a material sample [58]. Later, Rodrigues *et al.* extended this number to 75 lines using a 1D diffractive optical element (DOE), which allowed them to capture fine

changes in the velocity field spanning 120 mm by 120 mm [59]. An example of the 10 Hz NO MTV 75-line pattern is shown in Fig. 5. In terms of high repetition rate, the required excitation wavelength is conventionally generated with high-repetition-rate Nd:YAG-pumped optical parametric oscillators in both their seeded (narrow linewidth - near 0.01 cm^{-1}) and unseeded (broadband - near 10 cm^{-1}) operation modes. A few examples of high-repetition-rate NO MTV include works by Jans *et al.* achieving an effective velocity measurement rate behind a free-flight model in a large-scale high-enthalpy facility of 20 kHz [60] and Rodrigues *et al.* demonstrating 100 kHz velocity measurements of multiple lines [52]. While the discussion of high-repetition-rate burst-mode OPOs as a laser source for nitric oxide MTV and PLIF can be lengthy, the following references may be a good starting point for additional reading [61–63].

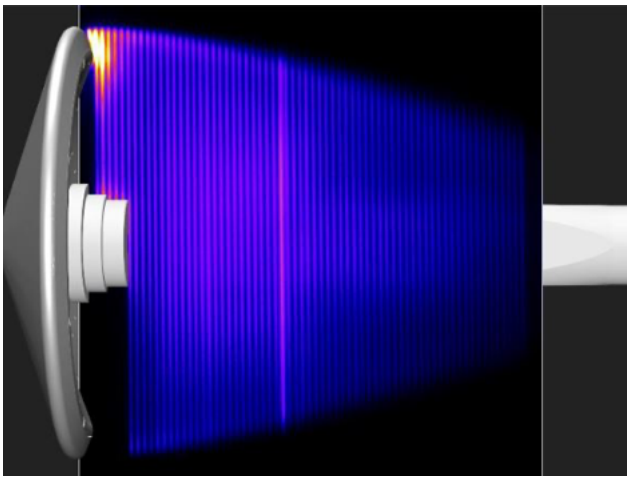

Fig. 5 An NO-MTV image generated by the diffractive optical element with up to 75 lines generated. Adapted with authors' permission from [59]. Work of the U.S. Government.

The discussion of nitric oxide MTV, especially in its high-repetition-rate form, is incomplete without introducing its earlier variant - nitrogen dioxide, or NO_2, MTV. This method relies on the photodissociation of NO_2 ($NO_2(X^2A_1) + h\nu \rightarrow NO(X^2\Pi) + O(^3P)$) with either a 355 nm or 308 nm laser beam, which produces a localized nitric oxide population at the laser beam location. As was discussed above, nitric oxide is relatively stable, making the patterns written by photodissociation traceable with conventional NO planar laser-induced fluorescence over significantly longer timescales than NO-MTV (on the order of milliseconds). The first demonstration of NO_2 MTV was reported by Orlemann as early as 1999 and utilized a combination of an excimer laser to "write" a line in the NO_2 seeded flow and an excimer-pumped dye laser to probe the convected NO [64]. This technique was advanced by Hsu *et al.* in 2009 with a 2D velocity measurement in an underexpanded jet with a 15 by 25 line grid and showed a strong agreement with CFD results [65]. Later, Jiang *et al.* utilized NO_2 MTV in 2011 for one of the highest repetition rate velocity measurements in literature at 500 kHz, setting a high bar for future MTV development [66]. Despite these promising results, longer signal lifetimes, and the overall push in the MTV development, NO_2 MTV remained a niche diagnostic due to the complexity of two-beam alignment and higher NO_2 toxicity. However, it became a stepping stone for the development of another diagnostic - Vibrationally Excited NO Monitoring (VENOM). In their original works on VENOM in 2011 and 2012, Sanchez-Gonzalez *et al.* [67] extended the works by Hsu *et al.* [65] and demonstrated simultaneous two-component velocity and temperature measurements in a gaseous supersonic flow-field by sequentially probing two different rotational states of the vibrationally excited nitric oxide pattern produced by NO_2 photodissociation, as shown in Fig. 6. Such coupled measurements of transport parameters and thermodynamic properties are essential for understanding complex nonequilibrium flow-fields, such as those within high-speed turbulent boundary layers. However, VENOM required an even more complex laser system consisting of one Nd:YAG laser outputting its 3rd harmonic (355 nm) and two tunable Nd:YAG-pumped dye lasers with two mutually delayed UV outputs near 224 nm with a slight spectral shift in between. Later implementations of VENOM supplemented NO_2 seeding for the less toxic and corrosive NO, which also had the added advantage of a lower condensation temperature than NO_2, but now required all three beams to be produced by mutually delayed tunable Nd:YAG-pumped dye lasers [68]. While this technique provided insight into correlating fluctuations in velocity and scalar parameters of non-equilibrium flows, it has yet to receive broad utilization in the aerodynamic measurement technology community due to its experimental complexity.

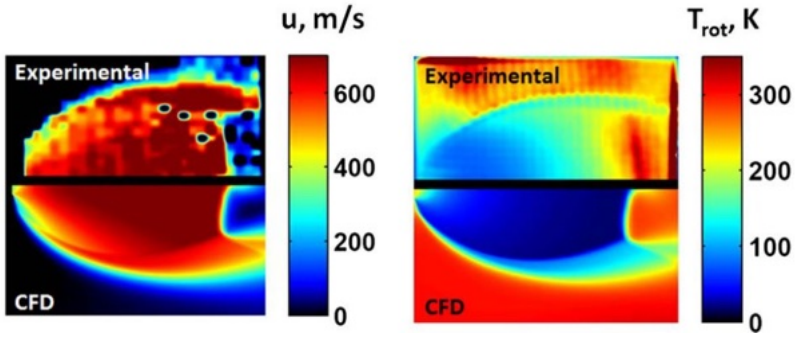

Fig. 6 VENOM velocimetry results in an underexpanded jet averaged over 100 shots and compared with CFD: (left) streamwise velocity map; (right) rotational temperature map. Reprinted with permission from [67] © Optical Society of America.

.

The next leap in nitric oxide MTV development started in 2023, when Leonov *et al.* first achieved flow tagging with two to three orders of magnitude longer fluorescence lifetime than conventional NO-MTV by resonantly ionizing nitric oxide and observing the resulting fluorescence in the visible-NIR spectral region [69]. This new method was given the name Nitric-oxide ionization-induced Flow Tagging and Imaging (NiiFTI). Similar to the conventional NO-MTV, NiiFTI is a single-laser technique with the first demonstration using a 250 kHz repetition rate, nanosecond, broadband 226 nm output of a burst-mode OPO to effectively tag NO-seeded hypersonic air flow. Unlike conventional NO-MTV, which utilizes single-photon laser-induced fluorescence, NiiFTI is a multi-photon (1+1) MTV technique that requires somewhat higher laser intensity (typically around 1 mJ/pulse) to drive the multi-photon process. While the exact explanation of NiiFTI's photophysics requires additional rigorous study, Fig. 7 shows the energy diagram of processes hypothesized to occur in three phases: resonant two-photon ionization of nitric oxide [70]; delayed energy transfer from nitric oxide ions to molecular nitrogen resulting in its electronic excitation; photon emission (similar to FLEET's) from N_2 $(B^3\Pi_g) \rightarrow N_2$ $(A^3\Sigma_u^+)$ electronic transitions of nitrogen, also known as the First Positive System (FPS) [71]. Based on the measurement in a flowing cell, the resulting 500-900 nm fluorescence exhibits a triple exponential decay with typical lifetimes of: 10s of nanoseconds, 100s of nanoseconds, and 10s to 100s of microseconds [69]. The third, longest decay component was found to be a growing function of nitric oxide number density when mixed with air or nitrogen, and vanished in pure nitric oxide, pure nitrogen, and nitric oxide - carbon dioxide mixtures. It is worth noting that the NiiFTI signal, despite its spectral and temporal similarity to FLEET, does not suffer in oxygen-rich environments, such as air, due to a different limiting reaction. It is hypothesized that FLEET's limiting reaction is the atomic nitrogen recombination into electronically excited molecular nitrogen, which suffers from the competing nitric oxide formation due to atomic nitrogen recombination with oxygen. NiiFTI's limiting reaction is hypothesized to be a direct energy transfer from nitric oxide ions into molecular nitrogen; hence, it is independent of the oxygen presence [69]. In 2024, Jiang *et al.* reported an alternative version of NiiFTI that was developed independently, utilizing ultraviolet signal collection [72].

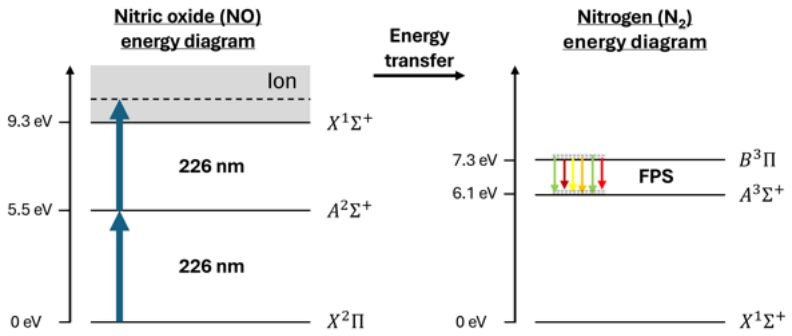

Fig. 7 A simplified energy diagram showing photophysical processes associated with NiiFTI.

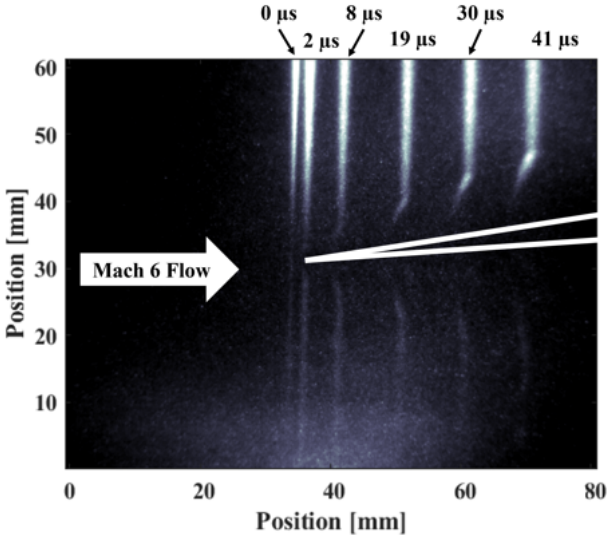

Fig. 8 An example NiiFTI image acquired with the single laser beam propagating upstream of a sharp tip wedge model (outlined in white) in a Mach 6 air flow seeded with 1% nitric oxide. Multiple tagged lines were recorded by integrating 6 intensifier gates on a single camera image. The region below the model is fainter due to uneven NO distribution within the flow.

To date, NiiFTI has been used in a few ground testing facilities, including both "cold" hypersonic and high-enthalpy hypersonic wind tunnels. In the case of "cold" air flows, nitric oxide was externally seeded with the mole fraction not exceeding 1%, which is typical for these types of facilities. The resulting fluorescence of nearly 50 μs allowed observing the tagged pattern at multiple locations and circumvented the need for a laser beam array, which was required for NO-MTV as discussed above [69]. Figure 8 shows a representative use case of NiiFTI for both freestream and boundary layer velocimetry performed in near Mach 6 flow with static temperature of 60 K. Recently, a seedless application of NiiFTI was demonstrated by a collaborative effort of Texas A&M University and Spectral Energies, LLC. for boundary layer profiling in the large-scale Hypervelocity Expansion Tunnel (HXT) [73]. The flow conditions (Mach 8.5-10 flow with total enthalpy near 4 MJ/kg) were sufficient to naturally form nitric oxide within the boundary layer and behind strong shock waves with the local NO mole fraction of up to a few percent. Under these relatively hot flow conditions (static temperature exceeded 3,000 K near the blunt nose), the NiiFTI signal lifetime reduced to 4 μs.

Regarding laser systems, NiiFTI has been demonstrated with both 10 Hz narrowband dye lasers outputting near 1 mJ per pulse of 226 nm radiation and high-speed burst-mode optical parametric oscillator (both seeded and unseeded) with similar pulse energy levels [74]. It is also suggested to utilize longer focal length lenses for the "pattern writing" stage to further improve the signal level. It is worth noting that in the cold flow case, some signal saturation effects were observed with narrowband pulse energies exceeding 0.5 mJ/pulse. NiiFTI was also recently demonstrated with a 5th harmonic output (213 nm) of the pulse-burst laser, which significantly simplified the experimental setup and provides a straightforward avenue to increase the repetition rate beyond 1 MHz in the future [75]. Regarding imaging setups, traditional NO-MTV relies on the UV signal collection, which primarily narrows the intensifier selection to options with a GEN II S20 photocathode (Q.E. near 20% at 230 nm). NiiFTI can utilize a wider range of intensifiers with higher sensitivity in the visible range, including GEN II S25 (Q.E. near 15% at 550 nm) as well as GEN III GaAsP (Q.E. near 50% at 550 nm) and GaAs (Q.E. near 30% at 550 nm). At this time, intensified relay optics based on the GEN III GaAs photocathode are considered the optimal choice for both FLEET and NiiFTI due to its sensitivity extending further into the NIR region up to 900 nm.

D. Acetone - $(CH_3)_2CO$

Historically, acetone has been a common chemical tracer in flow diagnostics for several decades [76], and its fluorescent properties have been studied since the 1930-40s [77, 78]. As discussed by Lozano *et al.* [79], acetone has relatively low working toxicity and is not a known carcinogen. It does have a relatively low auto-ignition temperature of 738 K and flammability limits in air are 2.6% (lower explosive limit) and 12.8% (upper explosive limit) by volume.

The vapor pressure of acetone will determine the concentration that mixes into air and its temperature dependence is relatively well described by the empirical equation by Ambrose *et al.* [79, 80]:

$$\log_{10}(p\ [torr]) = 7.125267 - \frac{1214.208}{T\ [K] - 43.148} \tag{2}$$

The photophysics of acetone are relatively well documented in literature; however, there are inconsistencies due to competing chemical processes (such as the generation of biacetyl, another tracer used for flow diagnostics, phosphorescence versus fluorescence, *etc.*) that depend on the environment and excitation source [79]. Figure 9 shows the UV absorption band of acetone, and it is easily observed that the fourth harmonic of an Nd:YAG laser provides adequate excitation. This is perhaps the noteworthy benefit for acetone versus other techniques, because no complicated light conversion processes (*e.g.*, use of a dye laser or an optical parametric oscillator) are needed. Note however, various types of excitation sources have been used in literature, including the Nd:YAG 4th harmonic output, KrF excimer laser light at 248 nm, and XeC1 excimer laser light at 308 nm [79]. Since the excitation process is driven by single-photon absorption, excitation and tagging of acetone molecules in the flow will occur along the entire beam path if acetone is globally seeded. This can lead to significant beam attenuation over large scales and should be considered during experiments.

Figure 9 also shows the fluorescence emission yield with 266 nm excitation, as reported by Brunzendorf *et al.* [81], which shows peak emission in the blue range of the color spectrum. Since the emission band is relatively well separated from most of the excitation band, simple optical filtering can be used to isolate the fluorescence from the laser scatter background.

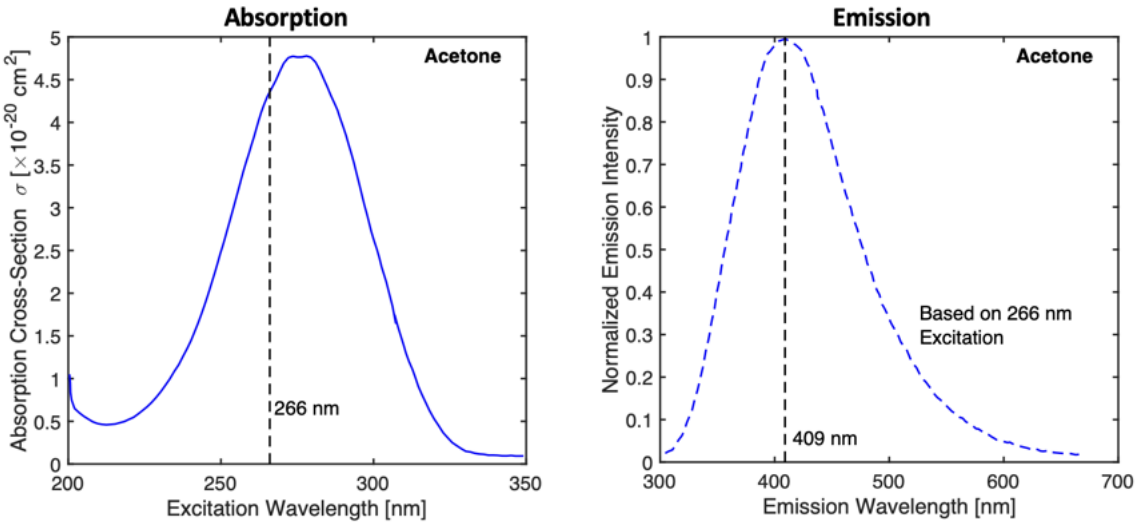

Fig. 9 (Left) The absorption cross-section of acetone in the UV range based on data from Lozano *et al.* [79], and (Right) the emission spectrum from acetone with 266 nm excitation based on data from Brunzendorf *et al.* [81]. The 266 nm line references the 4th-harmonic output of an Nd:YAG laser.

A few efforts have been made to model the processes resulting in light yield from acetone excitation [79, 82, 83], and a simplified energy level diagram is provided in Fig. 10 that captures the key features. As shown, the fluorescence yield results from a relatively straightforward process of excitation, vibrational relaxation, followed by the larger energy level changes. Alternatively, intersystem crossing can occur, and energy exchange processes then progress in a manner that produces a slightly different emission wavelength, which is fundamentally the difference between phosphorescence and fluorescence. Most importantly, the lifetime of fluorescence is typically around a few tens of nanoseconds at best, whereas phosphorescence is typically around 100 µs. Both emission processes have reportedly been used for flow tagging, with Lempert *et al.* [84] using the pure fluorescence process, while Gragston and Smith [85] and Andrade *et al.* [86] used the phosphorescence (hypothesized based on observed signal lifetimes). These works have led to continued interest and study of acetone for flow tagging measurements [87]. Also noted in Fig. 10 are the effects of quenching. Like most gas-phase fluorescent techniques, oxygen is a significant source of quenching.

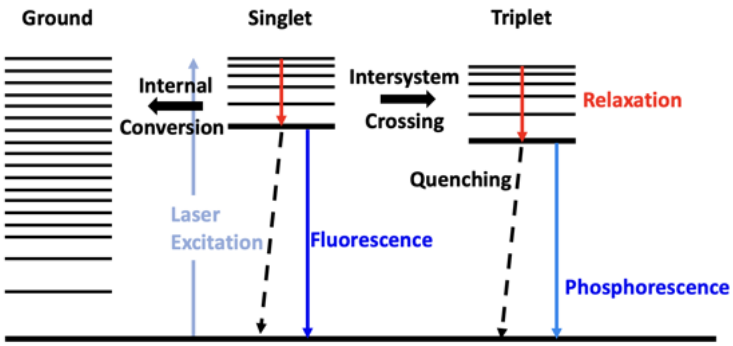

Fig. 10 A simplified diagram showing the photophysical processes associated with acetone fluorescence and phosphorescence.

Lastly, it is important to note the impacts acetone can have on the test gas, flow conditions, and the facility hardware when used as a tracer. The vapor pressure of acetone should also be considered to prevent its condensation, particularly in low temperature flows. Figure 11 shows the impact acetone has on the specific heat ratio γ and the isentropic speed of sound relative to the partial pressure of acetone expressed as a percent of net pressure. These calculations were also done in the work by Gragston and Smith [85], where tracking of expansion waves in the driver section of the Ludwieg tube were used to verify the speed of sound of the air-acetone mixture at room temperature stagnation conditions. In all, since relatively low partial pressures of acetone ($\leq$5%) are likely to be used, no substantial effect on gas thermodynamics are likely to occur.

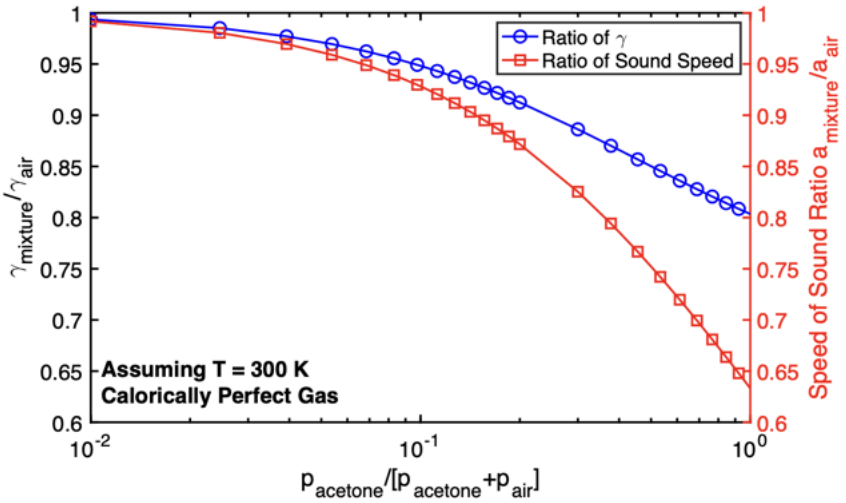

Fig. 11 A plot showing the effect acetone has on the specific heat ratio γ and the isentropic speed of sound based on the relative pressure of acetone to absolute static pressure. Note that the horizontal axis is equivalent to acetone mole fraction.

E. Hydroxyl - OH

Hydroxyl tagging is a technique well suited for measurements in high-speed flows with combustion occurring, such as simulated scramjet or ramjet internal flows, or with combustion being used in the air heating process for high-speed facilities, such as AEDC's APTU [88] and NASA's High Temperature Tunnel [89]. However, there have been applications in colder flow environments as well [90, 91], though such flows tend to have much less natural water content by design. As shown in Fig. 12, water molecules generated by the combustion of hydrocarbons or hydrogen are dissociated by deep-UV light and the resulting OH molecules are excited by a separate UV laser sheet to yield

laser-induced fluorescence, with the wavelength of this light chosen based on an appropriate ro-vibrational band of OH [92, 93]. In most applications thus far, an ArF laser is used for the dissociation of water since the $X \rightarrow \tilde{A}$ absorption band is broad [94]. For the "read" wavelength, the choice will depend on the temperature of the target gas and the available laser hardware. In early work by Pitz [92], a KrF laser was used to target the $A^2\Sigma^+ - X^2\Pi(3 \leftarrow 0)$) OH transition, which focused on applications to flame environments. Later works have used dye lasers, with read laser wavelengths of approximately 308 nm [91, 94–96] (work done in room temperature air flow and hydrogen flames) and 282 nm [90, 97] (work done in RC-19 wind tunnel). OH tagging has also been demonstrated with femtosecond laser systems [98].

The full spectroscopic details for OH tagging are discussed at length in the work by Ribarov *et al.* [95], which features a comparison of 248 nm, 282 nm, and 308 nm read laser wavelengths on signal quality. The signal-to-noise ratios determined for each of these were 2.4, 17, and 38, respectively, though different lasers were used. However, the conclusion was that while 308 nm provided the best overall capability for MTV measurements, it also featured strong potential for Mie scattering background when applied to an environment with particulates. The 248 nm read wavelength was deemed highly inefficient due to relatively weak fluorescence yields and higher potential to dissociate the target OH molecules.

A short review on OH tagging is provided by Pitz [93], which gives extended literature on the photophysics and applications to supersonic flows and aerospace relevant combusting flows.

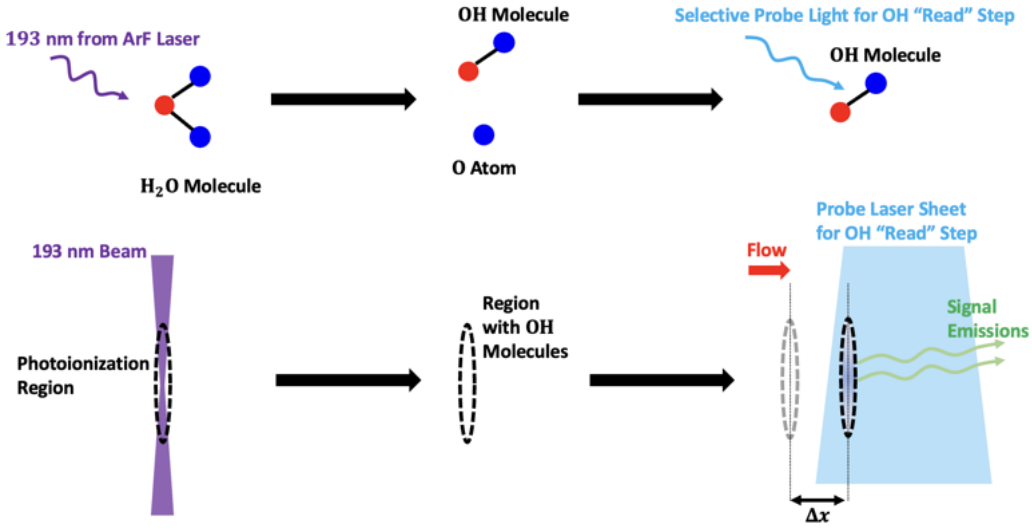

Fig. 12 An illustration of a basic approach to OH tagging, in which deep UV light from an ArF laser is used to photodissociate water molecules, which yields OH molecules that can be "read" by laser-induced fluorescence excited by another laser.

III. MTV Basic Setup

Here, the basic aspects of a typical MTV setup are discussed in a canonical sense, and information is provided regarding camera gating and intensifier selection for contextual purposes.

A. General Setup

To facilitate understanding of upcoming discussions, a canonical MTV setup is described here. As shown in Fig. 13, a laser beam is usually routed to the region of interest with mirrors and focused into the probe region using a plano-convex lens. Note that best practice is to align the collimated initial laser to the target region and then place the focusing lens to maintain the same optical axis as the initial beam. As discussed later, care should be taken to minimize laser-induced plasmas from the laser-surface interaction. The need for very short optical gates and the typically low-level emission from the decaying tagged lines typically requires the use of an intensified camera. Also, it is best practice to use an optical filter in the collection optics to remove laser scattering from surfaces or particulates. This filtering can be

done efficiently using a laser notch filter, however, a bandpass filter that excludes the laser wavelength but transmits the signal wavelengths can also be used. In the event that a filter is not available and significant laser scattering is present, a time delay for the first image can be used since fluorescence timescales are typically longer than the pulse duration of laser commonly used for MTV.

Finally, though not shown in Fig. 13, some techniques (see for example [22, 90]) utilize an additional laser beam as part of a "read" step. This beam is typically turned into a laser sheet and guided into the probe region.

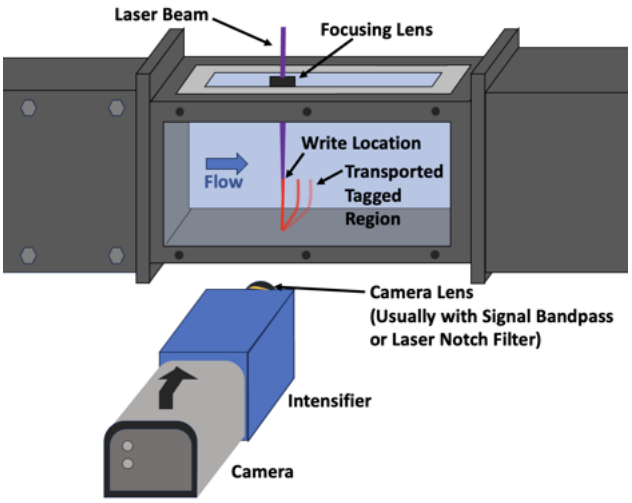

Fig. 13 An illustration of a basic MTV setup. Note that in some techniques, a laser sheet generated from a separate "read" laser may be needed.

B. Signal Collection Considerations

Signal collection for MTV has a myriad of considerations. Generally, lenses used to collect the emissions from the tagged region should have high throughput efficiency (*e.g.*, large aperture). This is especially important for MTV measurements that have a large standoff detection distance (i.e., the distance between the tagged region and the signal collection lens) because the signal intensity has an inverse square dependence with distance. Furthermore, it is advantageous to have high imaging resolution to reduce uncertainty in tracking convecting tagged regions. As shown in Fig. 14, a low resolution (with resolution described here by pixels per physical length) results in profiles that are jagged and non-Gaussian in shape compared to a higher resolution case. The quality of these line profiles will impact the uncertainty and effectiveness of the displacement tracking methods used to determine velocity.

Unlike PIV, the signal for most MTV techniques comes from a form of fluorescence, phosphorescence, or broadband spontaneous emission from recombination and de-excitation processes, which means that it is typically at least an order of magnitude weaker than scattering and is a decaying signal with respect to the laser excitation. This means that an intensified camera is often needed to see the tagged region as it convects with the flow, especially since the signal decays in time. The choice of intensifier comes down to gating speed requirements and wavelengths of interest, with the latter affecting the choice of photocathode material to maximize quantum efficiency in the signal wavelength range. For instance, the most common types of photocathodes in MTV applications are: Gen II S20 for ultraviolet wavelengths, Gen II S25 and Gen III GaAs for visible and near-IR wavelengths, and Gen III GaAsP, which is the commercially-available option with the highest quantum efficiency for wavelengths between approximately 400 and 650 nm. It is worth noting that Gen II photocathodes are typically more robust to damage due to overexposure but have lower peak quantum efficiencies. The most commonly utilized phosphor option for high-speed MTV is P46 due to its relatively swift decay time of around 1 μs (minimal ghosting effect for most applications) and predominantly green fluorescence, which is compatible with most cameras. A faster type of phosphor, P47, while providing even more rapid fluorescence decay on the order of a few hundred nanoseconds, has lower quantum efficiency and produces predominantly blue fluorescence centered at 400 nm, which may hinder its utilization with some cameras. Experimentalists can often examine the spectral quantum efficiency of their intensifiers using curves from the manufacturers and verify in the laboratory if needed.

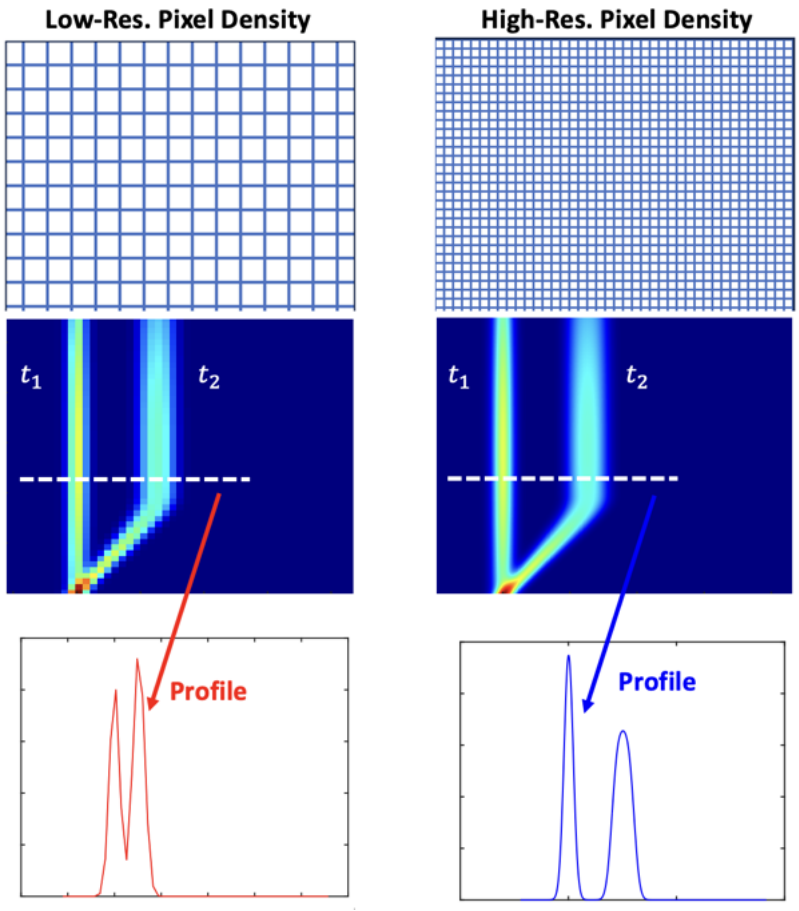

Fig. 14 A representation of how image resolution (pixels per physical length) affects resulting MTV images and line profiles used for tracking displacement.

Timing and setup of the exposure sequence for molecular tagging velocimetry experiments is highly dependent on equipment and the aspects of the measurements (i.e., excitation scheme, flow velocity, etc.). Here, a general discussion is provided with a focus on how exposure sequence setup can impact data processing and how to estimate reasonable parameters for the gate delay.

Two basic approaches are available for MTV measurements, as shown in Fig. 15. The first approach is shown in Fig. 15(a), where an intensifier is used as a fast electronic shutter within a longer camera exposure. The result is a single image containing two lines for displacement tracking (usually the pre-convected and convected MTV lines). The second approach, Fig. 15(b), uses some process (typically PIV-like frame straddling) to get two separate images. Technically, a third viable approach is simply to image the write line prior to the flow commencing and then dedicate image acquisition to capture only the convected line, but this approach is not optimal since guided beams typically shift around during wind tunnel operation due to vibrations (especially for impulse facilities) [74].

While some form of the first of these approaches is typically used in modern MTV measurements, it suffers from limited accuracy for low-displacement regions of the flow. This aspect is obviously limiting near a surface, where the no-slip condition applies, but it is also an issue for instantaneous MTV data in turbulent flows and can lead to slight errors in turbulent statistics. However, this approach is convenient in data analysis of high-speed flows, as all information needed for processing is contained in a single image, and it also helps reduce data storage for cameras. The second approach avoids all major issues of the first approach, but requires the use of a camera with a sufficiently short interframe spacing time with respect to the lifetime of the MTV signal. Interframe times less than 300 ns are possible with modern CMOS and sCMOS cameras.

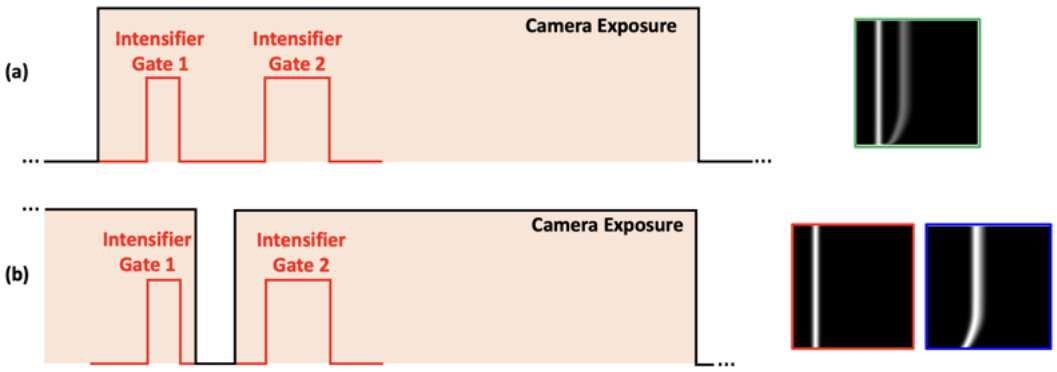

Fig. 15 Example of two basic gating approaches for basic molecular tagging velocimetry. (a) Multiple intensifier subexposures inside a single camera exposure. (b) Frame straddling to get two unique images.

Other aspects of exposure timing include the estimation of a duration Δt between intensifier exposures and the duration choices for each gate. While these values are highly dependent on the MTV technique of choice and the experimental setup, Eq. 3 provides a simple formula for estimating an appropriate Δt if a maximum velocity U_{max} from the target region can be estimated. The only other inputs are desired pixel displacement Δ_p (chosen to ensure the two MTV lines can be distinguished for tracking) and camera resolution R_{camera} in physical units per pixel. Alternatively, Eq. 3 can also be used to estimate pixel displacement if camera resolution and Δt are known.

$$\Delta t \approx \frac{\Delta_p \, R_{camera}}{U_{max}} \tag{3}$$

Regarding the duration of each exposure gate, note that MTV signals typically decay in intensity in an exponential manner. Thus, variable gate durations are typically used to prevent saturation for early acquisition times relative to the excitation pulse, while longer exposures are typical for delay times further away from the excitation pulse. However, as discussed in Section V, exposure times that are too long can lead to motion blurring effects that must be considered in data analysis.

IV. MTV Data Processing

A. Displacement Tracking Methods

The velocity is calculated from displacement per change in time, and for typical MTV experiments, the change in time is determined by the imaging setup. Hence, the key to obtaining velocity is the successful determination of the displacement of the tagged region. Table 2 shows a list of several approaches that can be used for MTV image analysis, along with general pros and cons for each method.

In most one-dimensional MTV applications (the primary focus here), such displacement determination is also done along each image pixel row within the tagged region (see Fig. 14). Peak intensity tracking can be used in this case if local data smoothing is appropriate and the focus is on mean data. However, this method will run into issues in low displacement scenarios where a second peak is obscured by the profile of the first line. It is also extremely unreliable for instantaneous data, where the tagged region often has specular and diffuse characteristics that lead to anomalous peaks. Therefore, it is not recommended for use, as the curve fitting approach is often more robust and can be equally simple.

Table 2 A table showing several different methods for displacement tracking in conventional MTV image data.

Method	Pros	Cons
Profile Peak Intensity Tracking	Simple to implement.	Very sensitive to noise; Not useful for instantaneous images; Limited by camera pixel resolution; Struggles in low-displacement scenarios.
Profile Curve Fitting	Simple to implement; Robust in terms of data applicability; Sub-pixel resolution; Most common approach in literature	Has some potential to work in low-displacement scenarios; Very difficult to apply in 2D.
Profile Cross-Correlation	Reasonably simple to implement; Similar to PIV methodology; Easier higher-dimensional data use	Limited to pixel resolution; Difficult to use on low-signal data; Struggles in low-displacement scenarios.
Optical Flow Analysis	Easier use for two-dimensional data; Can theoretically estimate planar components of velocity in 1D data.	Specialized analysis framework; Limited use in literature.

Curve fitting is the most common approach for 1D MTV data. Since laser beams are typically spatially Gaussian in intensity, a reasonable assumption is that the intensity profile of the tagged regions will also be close to Gaussian. This leads to a summed Gaussian fitting approach [99–102]:

$$I_{fit}(x) = \sum_{n=1}^{N} a_n e^{-(x-b_n)^2/c_n^2} \tag{4}$$

The number of terms N is equal to the number of lines that need to be tracked, but sometimes $N+1$ is used, with the additional Gaussian used to compensate for localized background. During application, it is also wise to bound the fit constants to reasonable values to facilitate better fitting. The Gaussian fitting approach can also be easily modified for tracking MTV "dots" as discussed by Burns *et al.* [29].

Another common fit choice is a psuedo-Voigt function $V_{ps}(x)$ [28, 59, 60, 103], which is a weighted superposition of Gaussian and Lorentzian functions:

$$V_{ps}(x) = a_n + b_n\left[\eta G(x;\mu_n,\sigma_n) + (1-\eta)L(x;\mu_n,\sigma_n)\right] \tag{5}$$

In Eq. 5, a_n and b_n are fit constants and η is a weighting parameter bound between 0 and 1 that is also determined via curve fitting. $G(x;\mu_n,\sigma_n)$ and $L(x;\mu_n,\sigma_n)$ represent Gaussian and Lorentzian functions, respectively, that are centered at μ_n and have widths described by σ_n. This fitting routine can be applied in multi-term summation like Eq. 4 to capture displacement of multiple tagged lines. The pseudo-Voigt fitting gives flexibility for sharper intensity decreases along the intensity profile and can theoretically do better than the standard Gaussian fitting. However, pseudo-Voigt functions may not be native to most curve fitting packages, whereas, summed Gaussian fitting typically is available, which simplifies error analysis.

The final two methods in Table 2 are typically only used for two-dimensional forms of molecular tagging velocimetry [90, 104, 105], and readers are encouraged to check literature for specific details on implementing these approaches. For example, the optical flow approach requires significant image pre-processing, as discussed in Gevelber *et al.* [104].

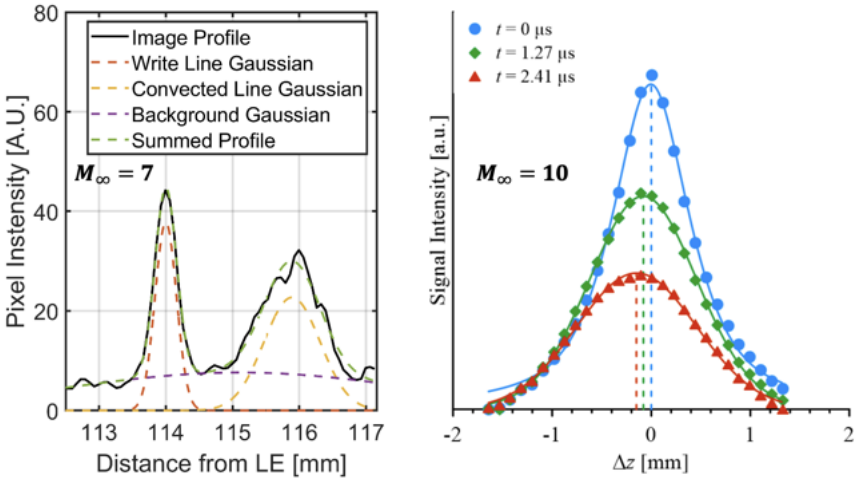

Fig. 16 Examples of intensity profile fits from (left) Webber *et al.* [101] and (right) Rodrigues *et al.* [59], which use fittings based on summed Gaussian functions and psuedo-Voigt, respectively. Adapted in part from [101] and [59] with permission from the authors.

B. Measurement Uncertainty Contributions

Estimating the overall uncertainty of MTV measurements is not straightforward due to the numerous possible sources of error that contribute to each source of uncertainty. For a single velocity component, the velocity as measured in the image may be expressed as:

$$u = M\frac{\Delta x}{\Delta t} \tag{6}$$

where M is the camera magnification (typically in mm/pixel), Δx is the measured displacement in pixels, and Δt is the prescribed time delay [43]. The relative uncertainty in the velocity is the result of the contributions to the uncertainty from each term in Eq. 6 as:

$$\frac{\sigma_u}{u} = \sqrt{\left(\frac{\sigma_M}{M}\right)^2 + \left(\frac{\sigma_{\Delta x}}{\Delta x}\right)^2 + \left(\frac{\sigma_{\Delta t}}{\Delta t}\right)^2} \tag{7}$$

where σ_u, σ_M, $\sigma_{\Delta x}$, and $\sigma_{\Delta t}$ are the corresponding confidence intervals. The confidence intervals themselves are impacted from a variety of sources of errors. Typically, errors in the magnification M ($\sim$ 1%) and time interval Δt $<$ 1% are sub-leading, as they are well-captured by image calibration and precision-timing electronics respectively. Of note is the reasonable argument that the uncertainty in M is systematic in nature, rather than random, and could be separated from the others as a fixed uncertainty.

The uncertainty in the measured displacement Δx is generally dominant (1% or greater), but the displacement itself can be subject to several effects. The line (or dot) size simultaneously impacts the precision of the sub-pixel fitting and the spatial filtering effect from averaging the motion of molecules within the illuminated line width or spot size. With a larger illuminated region, the sub-pixel accuracy may improve but the spatial filtering is more significant. The velocity computed from the line displacement is technically the average motion over the prescribed interval Δt, therefore a spatial filtering is also inherent as a function of the chosen interval time. As the interval time grows larger, other effects such as the influence of diffusion or flow accelerations can begin to bias the sub-pixel peak location of the second (or n-th) exposure. Quantitative insight on these effects is currently under-explored. In order to reduce the effect of averaging for planar velocimetry, multiple laser lines written into the flow are preferred over a single tagged line captured over several exposures.

Additional effects to consider also include motion blurring due to finite-length gated exposures (addressed in the next section), signal-to-noise ratio, intensifier electronic noise (particularly for extreme environments, *e.g.* a plasma torch) and intensifier resolution. Image intensifiers are constructed using micro-channel plates (MCP) between the photocathode and anode that fundamentally limit the image resolution to the number of micro-channels. Caution must

be exercised when the image sensor resolution is greater than the MCP resolution: the measurement spatial resolution is limited by the MCP in this case.

Typical pixel displacements depend on the flow of interest and the imaging implementation. For multiple gates within one image, the displacement should be enough to clearly distinguish between the lines or dots from successive gates (see Eq. 3). In freestream flows without shear layers, the displacement can be tens of pixels. In shear flows such as wakes or boundary layers, smaller displacements may be needed to reduce errors from flow accelerations. It is best practice to use a high-speed camera or a dual-pulse camera and frame-straddle the gates between successive images in these cases.

C. Motion Blur and Signal Decay Corrections

Since MTV requires imaging of a region of tagged molecules in transport by the flow, the motion of these molecules during an exposure can result in blurring effects in the resulting image. The blurring in the image can then artificially inflate determined velocities by making it seem like the line convected slightly more during the time between frames. This effect was explored through synthetic data by Gragston [106], and an estimate of the effect of motion blurring can be determined by considering how much the tagged molecules displace during an exposure.

$$\Delta_{p,Blur} \approx \frac{u\, t_G}{R_{camera}} \tag{8}$$

In Eq. 8, the pixel displacement $\Delta_{p,Blur}$ from motion during the exposure of duration t_G for a local velocity of u can be estimated, with R_{camera} being the imaging resolution (in units of physical distance per pixel). Thus, clearly the contributing factors to motion blurring are the local velocity, the exposure duration, and the camera resolution. For either higher velocities, higher-imaging resolution, or longer duration exposures, more blur can be expected. As discussed in the work by Gragston [106], the emission lifetime is also an important factor for motion blur effects.

Since motion blur is prominent in high-speed flow applications of MTV, it is important to understand how to account for it during data analysis in order to get the correct velocities. Approaches for dealing with motion blur effects have been discussed by Danehy *et al.* [54], Bathel [107], and Gragston [106], each with different assumptions. The most commonly adopted approach follows the reasoning outlined by Danehy *et al.* [54] and computes the time delay (Δt) as the difference between the "write" line and the "convected" line imaging exposure gate centers. The blur-corrected velocity is then calculated as presented in Eq. 9:

$$u = \frac{\Delta x}{t_d + (t_{G1} + t_{G2})/2}, \tag{9}$$

where Δx [m] is the measured displacement between the MTV lines, t_d [s] is the delay between the corresponding intensifier gates, t_{G1} [s] is the first gate width, and t_{G2} [s] is the second gate width. Danehy *et al.* [54] pointed out that a key assumption for this approach was that the emission decay time constant was much longer than the exposure (*i.e.*, the emission of the convecting line was effectively constant during the camera exposure period). This assumption is critical for very short signal lifetime MTV methods, such as NO MTV or FLEET in air. For instance, Bathel *et al.* [108] showed that the error introduced by signal decay of NO MTV ($\tau_{NO\ MTV} \leq 200$ ns) may artificially lower the measured velocity by upwards of 10%. However, as the signal lifetime increases, the introduced error decreases. Pehrson *et al.* [99] calculated the error of around 3% introduced by FLEET signal decay in air ($\tau_{FLEET} \approx 400$ ns at the specific conditions reported in [99]), which is still significant and has to be accounted for. In the high-enthalpy flow environment NiiFTI has a moderate decay of around $\tau_{NiiFTI} \approx 4\mu s$, as presented by Leonov *et al.* [73], and its effect was calculated not to exceed 0.5% and was deemed negligible for the application. In long fluorescence cases ($\tau \gg t_G$), such as acetone MTV, FLEET in nitrogen flows, NiiFTI in cold flows, and many multi-beam methods, the measurement error introduced by fluorescence decay is found to be statistically insignificant and is universally omitted from the analysis [69, 85, 86]. The MTV signal decay can be estimated *in-situ* based on the ratio of the integrated line intensities normalized by the corresponding gate widths.

The method recently discussed by Gragston [106], on the other hand, mathematically models the imaging process of an idealized MTV experiment using convolutions, with the model exactly replicating motion blur and fluorescence decay effects. He then creates a linear mapping between the measured velocity (which is errant due to blur effects) and the actual velocity (a MATLAB® code that computes the mapping is provided as supplemental material in that paper). Gragston successfully tested his approach using synthetic MTV data, as shown in Fig. 17, showing successful correction of motion blurred results compared to the theoretical values and also showed the impact motion blurring can

have on skin-friction values determined from MTV data. Finally, he also demonstrated his model, which naturally included considerations of finite emission lifetimes, simplified back to the gate centering approach discussed by Danehy *et al.* if MTV line emissions were long-lived compared to the camera gate widths. It is worth noting that both the motion blur and signal decay effects drop out if the intensifier gates used for capturing the MTV original and convected line position are of equal widths ($t_{G1} = t_{G2}$).

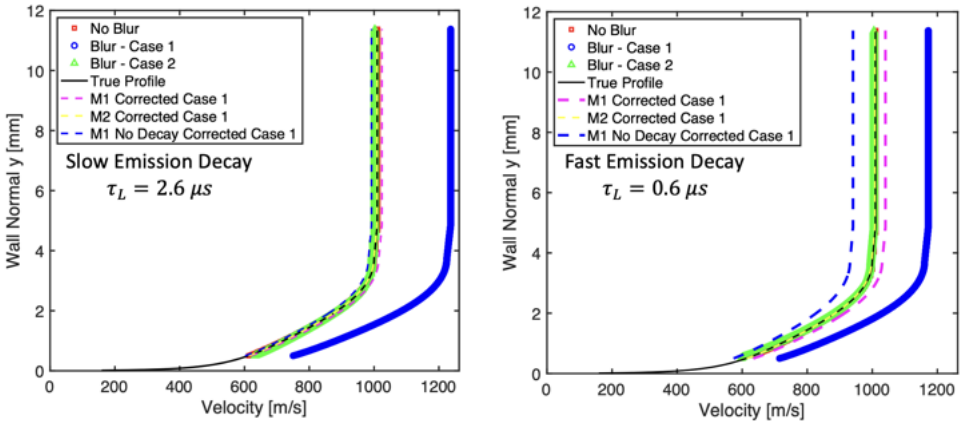

Fig. 17 (Left) Effect of motion blur on velocity extraction for slow emission decay and (right) fast emission decay. Calculations are based on synthetic MTV data as discussed by Gragston [106]. Note that "M1 No Decay Corrected Case 1" is identical to the gate centering approach, while "M2 Corrected Case 1" is the method recommended by Gragston. Adapted with author permission from [106] © Mark Gragston.

D. Estimating Secondary Quantities

While MTV provides velocity values and typically profiles, there is often a need to know additional fluid dynamic quantities. This section focuses on using the velocity information to infer those additional quantities (*e.g.*, skin-friction, static temperature, or density).

1. Wall Shear Stress

Wall shear stress is an important engineering quantity since it directly provides information about drag forces and, when converted to skin-friction, it can be used in many situations with the Reynolds analogy to estimate surface heating. This section focuses on basic approaches to calculating wall shear stress from MTV velocity profile data (though these methods apply to any velocity measurements).

For laminar boundary layers, there is no preferred or sophisticated approach to obtaining the wall shear stress. Since high-speed laminar boundary layer profiles with zero or mildly favorable pressure gradients are largely linear in shape near the wall, the simplest approach is to apply a linear fit in the suitable region and determine the wall shear stress from the slope, $\tau_w = \mu \frac{du}{dy}$, where μ is the dynamic viscosity. In strong pressure gradients (favorable or adverse) a Pohlhaussen [109] type of polynomial can be used instead or scaled forms of Falkner-Skan [109] style profiles.

For turbulent boundary layers, estimation of the wall shear stress can be done in two ways: the Clauser method [85, 110] and the fitting to a theoretical profile, which for this work will be the Sun-Childs profile [111, 112] (the authors note that there is a significant typo in Sun and Childs' original formulation for the theoretical profile). Both approaches are in fact fundamentally fit procedures, but the Clauser method is more restrictive.

The most basic form of the Clauser method utilizes the inner (viscous) coordinates formalism of the turbulent boundary layer profile, which in its simplest form, uses the basic log-law:

$$u^+ = \frac{1}{\kappa} \ln(y^+) + B \tag{10}$$

For this relation, $u^+ = u/u_\tau$, κ is a constant (usually taken as 0.41), $y^+ = u_\tau y/\nu_w$, and B is a constant (usually taken as between 5 and 5.5). Since Eq. 10 gives a "universal" piece of the turbulent boundary layer profile, the Clauser

method seeks to fit it to velocity data by adjusting τ_w, which changes u_τ, until the data and log-law overlap. This is best accomplished via least-squares procedures, but note that the log-law applies to a limited range of y^+ values.

However, this formalism can only be extended to compressible flows by means of the van Driest transformations, which are [113]:

$$u_{eff} = \frac{U_e}{A}\sin^{-1}\left(\frac{2A^2\frac{\bar{u}}{U_e} - B}{C}\right) + \frac{U_e}{A}\sin^{-1}\left(\frac{B}{C}\right) \tag{11}$$

$$A = \left(r\frac{\gamma-1}{2}M_e^2\frac{T_e}{T_w}\right)^{1/2} \tag{12}$$

$$B = \frac{T_{aw}}{T_w} - 1 \tag{13}$$

$$C = (B^2 + 4A^2)^{1/2} \tag{14}$$

These equations can then be applied to the log-law with $u^+ = u_{eff}/u_\tau$ and $u_\tau = \sqrt{\tau_w/\rho_w}$. Figure 18 summarizes the basic steps for using the Clauser method, and Fig. 19 shows an example of the technique applied to MTV data to determine the friction velocity and wall shear stress [85].

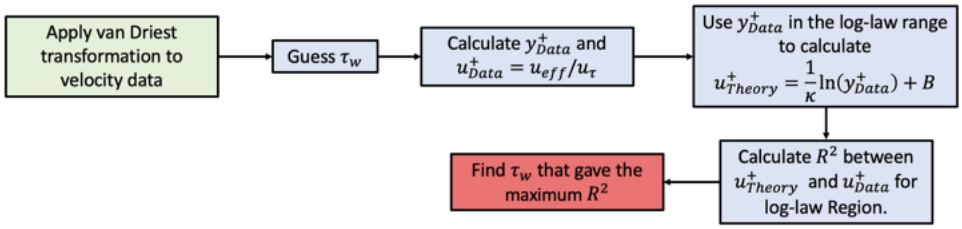

Fig. 18 A flowchart describing the steps for using the Clauser method to determine wall shear stress.

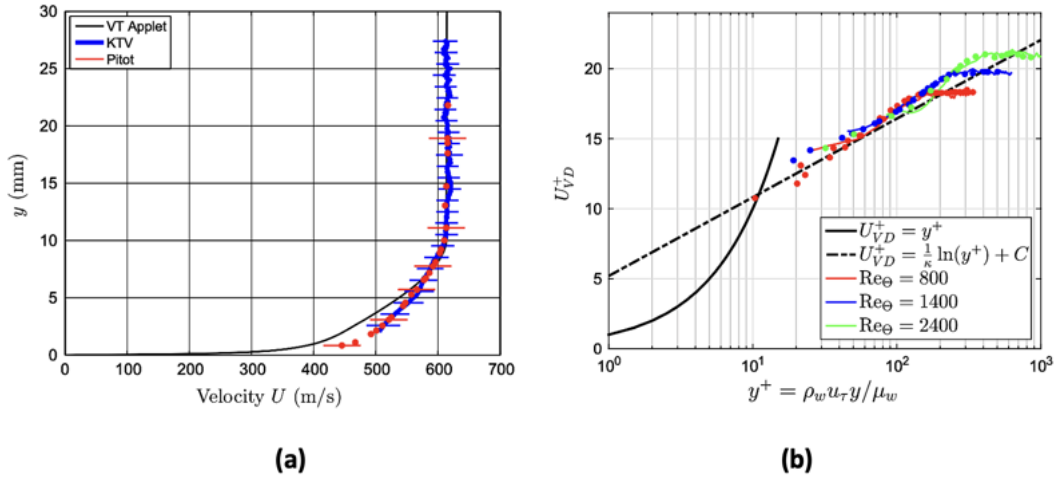

Fig. 19 Results from application of the Clauser method to krypton tagging velocimetry measurements of a turbulent boundary layer by Zahradka *et al.* [100]. Adapted with permission from [100] © Springer-Verlag Berlin Heidelberg 2016.

As discussed by Wei *et al.* [110] there are limitations to the Clauser method for high-speed flows. First, the log-law region must be resolved in the measurement. Second, the van Driest transformation fundamentally relies on the Morkovin hypothesis [113] that compressible turbulence can be treated similar to incompressible turbulence, which can

be invalid at very high edge Mach numbers. Finally, it assumes the log-law (or whichever base profile is used in the theoretical calculation) holds over some finite region, and ignores effects at locations closer to the wall. To circumvent the latter of these restrictions, one may use Spalding's law of the wall [109, 114] instead as the fit in the (y^+, u^+) domain.

$$y^+ = u^+ + e^{-\kappa B}\left[e^{\kappa u^+} - 1 - \kappa u^+ - \frac{(\kappa u^+)^2}{2} - \frac{(\kappa u^+)^3}{6}\right] \tag{15}$$

Spalding's law uses the entire inner-layer velocity profile information for fitting, making the residual calculation much simpler for the least squares fitting. This approach is highly recommended over use of the log-law if much of the inner layer is resolved, but it is restricted to zero pressure gradient flows. If only the outer layer and log-layer are resolved in the measurements, Coles' law [109, 115], which has a wake term, might be best, as hypersonic turbulent boundary layer flows are known to exhibit strong wake features.

The Sun-Childs [111] curve fitting approach directly tries to fit the velocity data with a theoretical compressible turbulent profile. It is a semi-empirical extension of the Cole's wake law combined with the van Driest transformation and works best for near-adiabatic wall conditions. The profile is expressed in terms of a dimensionless wall coordinate $\eta = y/\delta$:

$$\begin{aligned}\frac{\bar{u}}{U_e} = \frac{C}{2A^2}\sin\left(\sin^{-1}\left(\frac{2A^2 - B}{C}\right)\right.\left[1 + \frac{1}{\kappa}\frac{u_\tau}{U_e^*}\left(\ln(\eta) + \frac{2(1-\eta^a)^{1/2}}{a} - \frac{2}{a}\ln(1+\sqrt{(1-\eta^a)})\right)\right. \\ \left.\left. - \frac{\Pi}{\kappa}\frac{u_\tau}{U_e^*}(1+\cos(\pi\eta))\right]\right) + \frac{B}{2A^2}\end{aligned} \tag{16}$$

The quantities Π/κ and U_e^*/u_τ are given by the relations:

$$\frac{\Pi}{\kappa} = \frac{1}{2}\left[\frac{U_e^*}{u_\tau} - \frac{1}{\kappa}\ln(\delta^+) - 5.1 + \frac{0.614}{a\kappa}\right] \tag{17}$$

$$\frac{U_e^*}{u_\tau} = \frac{U_e}{u_\tau}\frac{1}{A}\sin^{-1}\left[\frac{2A^2 - B}{C}\right] \tag{18}$$

With the parameter a fixed to unity or infinity (i.e. a large number), the fit technically only requires δ and τ_w (the latter is in the shear velocity $u_\tau = \sqrt{\tau_w/\rho_w}$). Therefore, assuming that the boundary layer thickness is known, the only fit parameter is the wall shear stress. This fit can then be implemented in a least squares process.

For transitional boundary layer profiles, there is no theoretical formalism for profile fitting via the Clauser method approaches discussed previously. As discussed in the recent work by Webber *et al.* [102], there is precedent [116, 117] to fit data to $u^+ = y^+$ in the viscous sublayer region of $y^+ < 10$, but this approach requires a resolution near the surface that is often difficult to obtain. Webber *et al.* [102] utilized a Clauser method profile fitting scheme based on scaling of nondimensionalized, CFD generated transitional profiles, which compared well with (limited) theory and agreed well with the viscous sublayer fitting approach. The benefit of this approach was the ability to use more data throughout the boundary layer for fitting, and it was also shown to have less uncertainty than just fitting the viscous sublayer.

2. Temperature and Density

While velocity is often a key quantity, information about temperature and density can be just as valuable. For both laminar and turbulent boundary layer flows, a useful relation exists to provide a relatively accurate mapping of the velocity profile to a temperature profile $T(y)$. This relation is called the Crocco-Busemann relation and is given by White and Majdalani [109]:

$$\bar{T} \approx T_w + (T_{aw} - T_w)\frac{\bar{u}}{U_e} - r\frac{\bar{u}^2}{2c_p} \tag{19}$$

In Eq. 19, T_w is the wall temperature, T_{aw} is the adiabatic wall temperature, r is the temperature recovery factor, $u(y)$ is the velocity, U_e is the local boundary layer edge inviscid velocity, and c_p is the specific heat of the gas. This relation holds for Pr near unity (such as for air) and for weak pressure gradients. It is common to use $r = \sqrt{Pr}$ for laminar flows and $r = Pr^{1/3}$ for turbulent flows. Another minute detail to remember is that the thermal boundary layer thickness is not equal to the velocity boundary layer thickness, and for air, it is actually slightly larger than the velocity boundary layer thickness. For laminar flows, it can be shown through similarity solution that the ratio of thermal and

velocity boundary layer thicknesses is approximately $Pr^{-1/3}$. Thus, the temperature profile given by Eq. 19 will not have the correct thermal boundary layer thickness.

With temperature information given by the Crocco-Busemann relation, the density profile can be determined from utilizing the fact that both laminar and turbulent boundary layers have negligible wall normal pressure gradients, which implies the static pressure is constant in the wall normal direction. Thus, the ideal gas law can be used to relate the temperature ratio T/T_e to the density ratio ρ/ρ_e:

$$\frac{\rho}{\rho_e} = \frac{T_e}{T} \tag{20}$$

Hence, if the Crocco-Busemann relation is used to determine the velocity profile and the inviscid edge conditions are known, the density profile can be determined.

These exact methods were used in MTV work by Smith *et al.* [112] on fitted MTV data, as shown in Fig. 20. The combined velocity and temperature data was then used to estimate the Mach number profile. The Mach number profile can be used to determine information about the sonic point in the boundary layer, which has important implications for the dynamics of shockwave-boundary layer interactions.

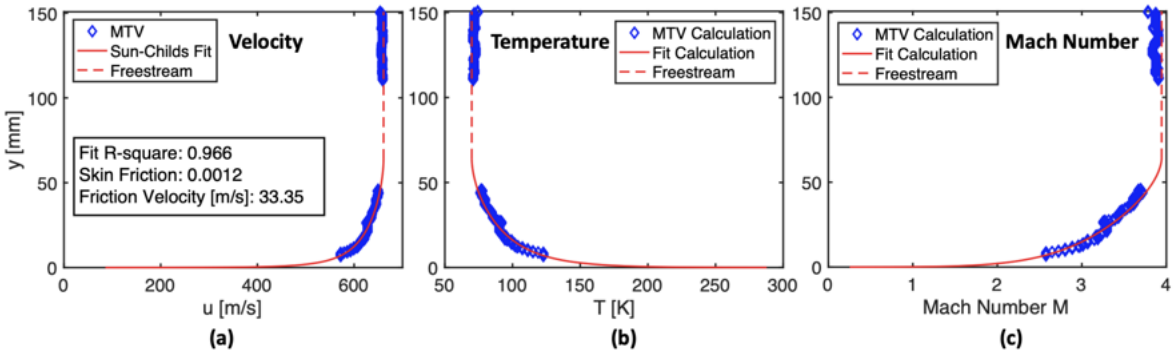

Fig. 20 Application of the Crocco-Busemann relation calculation to fitted acetone MTV data from Smith *et al* [112]. Adapted with permission from the authors [112]. Copyright 2023 by the American Institute of Aeronautics and Astronautics.

For inviscid flow regions like the freestream in a wind tunnel, temperature estimation can be inferred from either the known Mach number of the facility (typically found via pitot probes or total-to-static pressure ratios) or via the adiabatic assumption for inviscid flow. In the first case, the static temperature is determined by the known local Mach number and gas properties using:

$$T = \frac{u^2}{\gamma R M^2} \tag{21}$$

For the adiabatic assumption approach, the total enthalpy relation gives the static temperature for a known total (specific) enthalpy:

$$T = \frac{h_t}{c_p} - \frac{u^2}{2c_p} \tag{22}$$

.

Equation 21 is useful if the Mach number of the tunnel is well characterized and is especially useful if pitot probe measurements are done in tandem with MTV to characterize a freestream flow since it provides the freestream static temperature. Equation 22 can also be used if the total temperature or the total enthalpy h_t is better known than the Mach number (for example, in an expansion tunnel). These equations provide a natural framework for using MTV alongside traditional pressure probes to characterize wind tunnel flow. An example of Eq. 21 being applied to analysis of a Ludwieg tube is shown in Fig. 21, where the static temperature from Eq. 21 is compared to stagnation probe measurements.

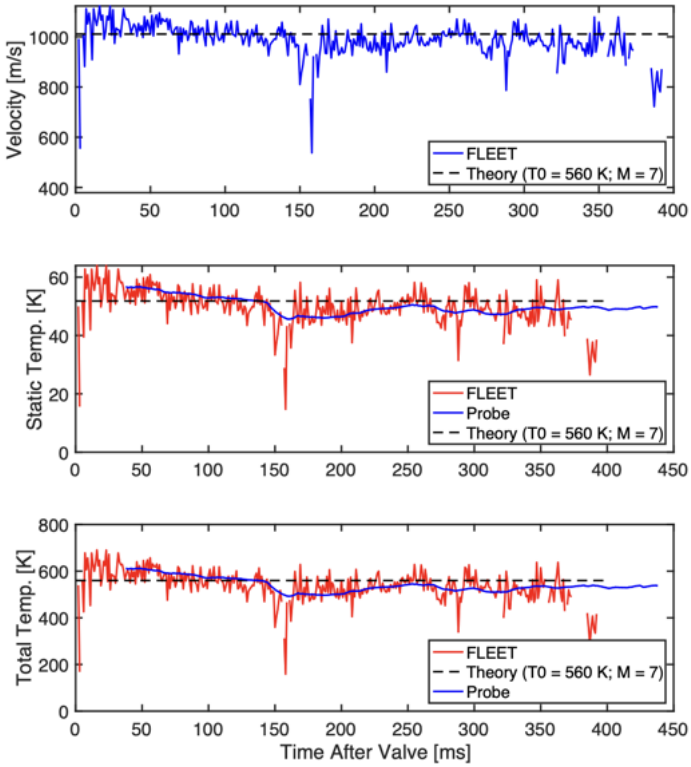

Fig. 21 Application of 1 kHz FLEET velocimetry to analyze the temporal evolution of static and total temperatures in a Mach 7 Ludwieg tube, with comparison to stagnation probe measurements. Note that the large drops in velocity signify wave passage dynamics, which occur around every 100 ms.

V. Example Applications in High-Speed Flows

A. Freestream Flows and Tunnel Characterization

In this section, we will discuss a few examples of freestream flow characterization in high-speed ground testing facilities, presented in chronological order. These examples will represent a gradual evolution of convenience and measurement frequencies for MTV techniques, from 10 Hz dye lasers to kHz-rate femtosecond lasers, and finally to hundreds of kHz burst-mode lasers. Achieved advancements in ground testing will also be highlighted. Precise freestream flow characterization is of utmost importance for the community to provide accurate inputs for CFD validation studies and to develop trustworthy empirical scaling equations. Since none of the high-speed experimental facilities are capable of perfectly simulating the true flight environment, facility characterization is instrumental in identifying potential limitations, properly interpreting experimental data, and validating computational models.

In the first example, Inman *et al.* present the very first application of molecular tagging velocimetry in an arcjet facility [58]. Overall, arcjets are capable of producing high-enthalpy flows to study interplanetary entry conditions and test thermal protection system materials. However, this presents a challenge for laser diagnostic applications as the freestream flow in arcjets often possess high levels of dissociation and background luminescence. Here, nitric oxide molecular tagging velocimetry was applied to provide the baseline for both Earth and Mars atmospheric entry test conditions in the long-runtime 400 kW Hypersonic Materials Environmental Test System (HyMETS) at NASA Langley. In comparison to other MTV methods, NO-MTV has the advantage of strong signal intensity, enabling the use of very short camera gates, which helps to overcome the strong background luminescence produced by the facility. The MTV experimental setup was similar to those presented earlier in Sec. II.C, consisting of a nanosecond 10 Hz Nd:YAG-pumped dye laser producing a 226 nm output and an intensified UV-sensitive PIMAX-II camera. Figure 22

presents a summary of the experimental results with (a) and (b) clearly showing the spatial shift in the tagged lines between the undelayed image and the one delayed by 550 ns, respectively. The resulting axial velocity 2D field is presented in Fig. 22(c) and shows the velocities as high as 3400 m/s with around 8% fluctuations in the core flow. The maximum velocity uncertainty was quantified at 62 m/s. The radial velocity component, shown in Fig. 22(d), was measured with Doppler-resolved NO-PLIF. While performed in the same test entry, the techniques were not applied simultaneously. The important outcomes of the paper were the quantification of the uneven spatial distribution of nitric oxide and large velocity gradients in the radial dimension of the flow.

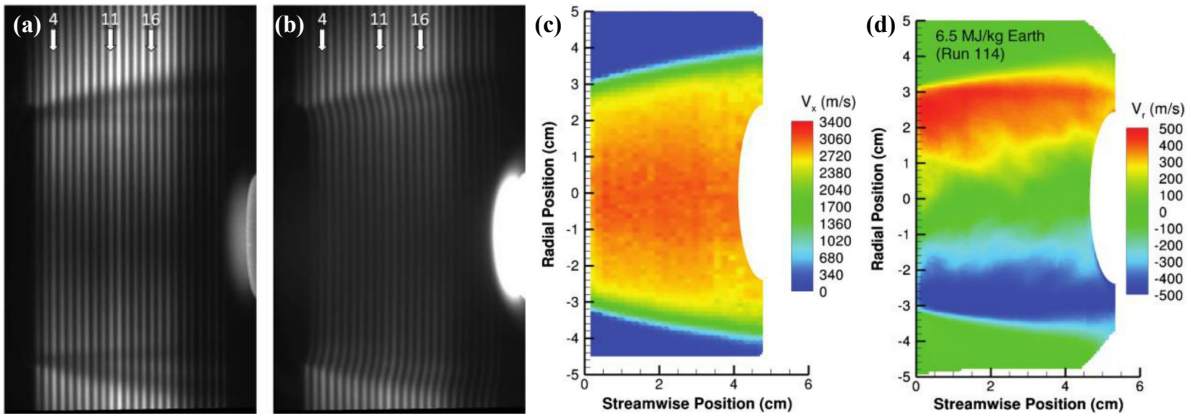

Fig. 22 Summary of the NO-MTV results from the arc-jet campaign by Inman *et al.*: (a) undelayed average image; (b) delayed image showing the tagged lines spatial shift induced by the flow; (c) extracted axial velocity field; (d) extracted radial velocity field. Adapted with permission from [58]. Work of the U.S. Government.

Validation of predicted flow conditions is another common goal for MTV applications in freestream flows, especially when these conditions are expected to change during the test time. The experimental investigations performed by Mustafa *et al.* [118] and Dogariu *et al.* [103] at the Arnold Engineering Development Complex (AEDC) Hypersonic Wind Tunnel 9 are such examples. Hypersonic Wind Tunnel 9 is a large-scale (5 feet in diameter) facility capable of generating high Mach numbers (up to 18) and Reynolds numbers (up to 1.6×10^8 1/m) by expanding heated and compressed nitrogen through a contoured nozzle over a long test time (a few seconds). However, due to the tunnel construction and plenum heating, while the Mach number is held constant through the test time, the static temperature within the core flow is predicted to increase, resulting in a varying freestream velocity. To verify such behavior, Mustafa *et al.* applied Krypton Tagging Velocimetry to measure the freestream velocity at 10 Hz with measurement uncertainty of 3% and achieved good agreement with predicted values to within approximately 2% across the test time. This method required two independent high-power Nd:YAG-pumped dye lasers for a "write-read" MTV configuration and 1% krypton flow seeding to achieve the result. Later, Dogariu *et al.* [103] improved on the previous work by applying a 1 kHz FLEET system across a similar range of conditions, with selected results shown in Fig. 23. In general, FLEET benefited from low static temperatures (≈55 K) and a pure nitrogen flow environment produced by Tunnel 9, which produced MTV lines traceable for tens of microseconds. Such a long temporal separation of the camera gates, in combination with high SNR, allowed for a reduction in single-shot relative measurement uncertainty to below 0.5%. Additionally, FLEET's experimental setup consisted of a single femtosecond laser and an intensified camera capable of collecting data at a 1 kHz rate, making it easier to operate and capture temporal flow fluctuations.

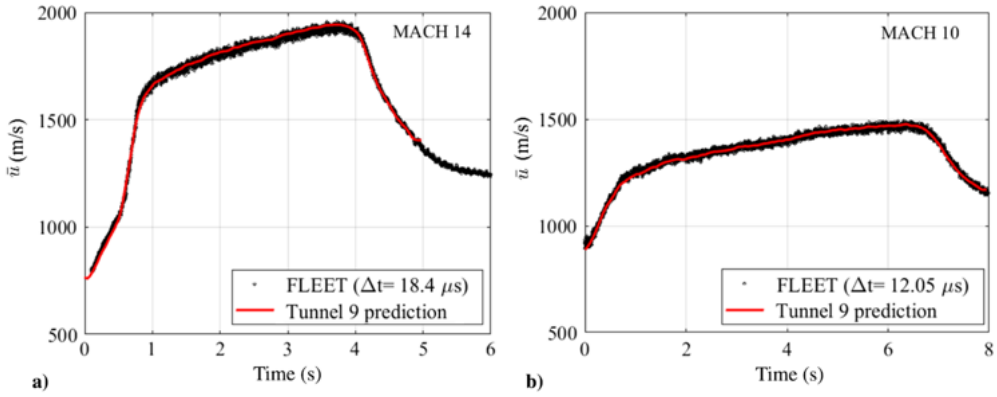

Fig. 23 Single-shot velocity measurement in AEDC Tunnel 9 with 1kHz FLEET for Mach 14 (a) and Mach 10 (b) flow conditions shown in black and the predicted velocity overlaid in red. From [103]; reprinted by permission of the American Institute of Aeronautics and Astronautics, Inc.

.

A similar FLEET system was also utilized by Gopal *et al.* to characterize the freestream flow in the 1.6 MW ONR-UTA arcjet plasma wind tunnel at the University of Texas at Arlington [119]. Similarly to the HyMETS example above, the ONR-UTA arcjet produces high-enthalpy hypersonic flow with a substantial level of background luminescence from plasma and molecular de-excitation within the flow itself, which causes problems for long-exposure diagnostic implementation, such as FLEET. Since the arcjet is capable of running with a variety of test gases, for this first demonstration of FLEET in an arcjet, Gopal *et al.* opted for lower bulk enthalpy within the operation range (2.2 MJ/kg), Mach 6.5, and pure nitrogen to mitigate some of the issues associated with FLEET, as outlined in Sec. II.B. Additionally, one of the unique features of the work was tailored spectral filtering that the authors employed to overcome strong background luminescence. Figure 24(a) shows the result of the optical emission spectroscopy collected from the region of interest and indicates the 725 nm to 900 nm spectral region chosen for optimal collection of FLEET signal. Such filtering suppressed the background luminescence by nearly 72% and allowed collection of around 32% of all single-shot images with sufficient SNR for velocity measurement. Figure 24(b) presents the single-shot tagging results with the "first" camera gates shown on the top and the "second" gates delayed by 4 μs shown on the bottom. Overall, the time-averaged velocity was measured to be 1788 m/s for these test conditions with the standard deviation of 209 m/s and the measurement uncertainty of 2.6%, indicating a significant freestream velocity fluctuation in the shock-diamond region.

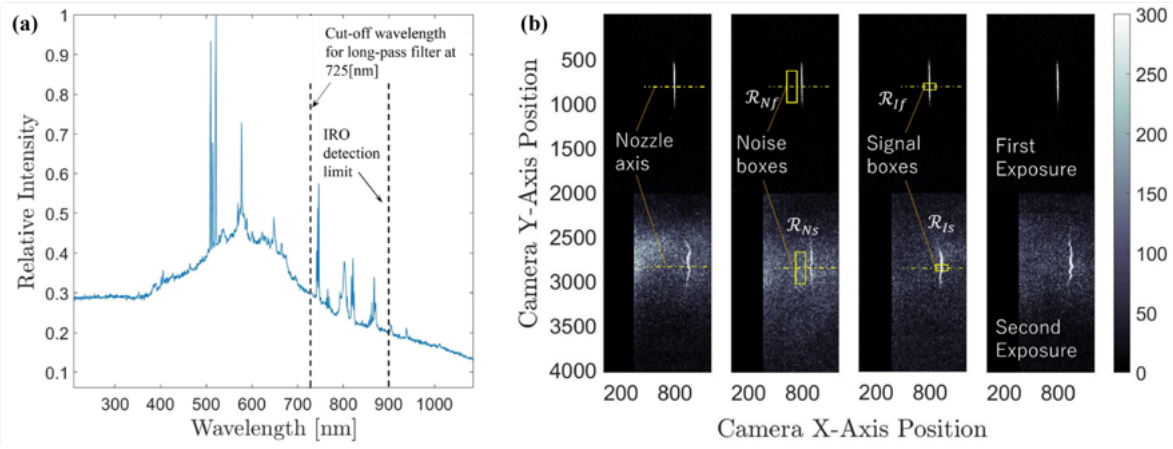

Fig. 24 Results from the FLEET implementation in the 1.6 MW ONR-UTA arcjet plasma wind tunnel at the University of Texas at Arlington. (a) Optical emission spectroscopy from the region of interest with indicated spectral region for FLEET signal collection; (b) a set of representative single-shot FLEET images with high SNR. Adapted with permission of authors from [119].

Another type of hypersonic ground-testing facility that is challenging for conventional MTV implementation is shock-driven facilities, including shock tubes, reflected-shock tunnels, and expansion tunnels. The challenges are typically associated with their short run time (on the order of a few milliseconds) and highly transient test conditions, in addition to the overwhelming chemiluminescence and optical quenching effects discussed above for arc-jet facilities. Such a short test time often implies a single laser pulse generation during the run for conventional laser systems, limiting the amount of useful data extracted from a single run. This was the case for the KTV application for the freestream characterization of the T5 Reflected-Shock Tunnel at Caltech reported by Shekhtman et al. [120, 121]. The goal of the campaign was to experimentally measure freestream velocity profiles and validate the anticipated facility test conditions, which are calculated based on the shock velocity and pressures in the driver and expansion sections of the tunnel at the time of run. Such characterization and anticipated condition validation are of utmost importance for future computational efforts in nonequilibrium thermochemistry and Navier-Stokes equations, which heavily rely on currently limited experimental data. For this experimental campaign, the authors simplified the KTV experimental setup compared to the AEDC example above, utilizing a single UV pulse at 216.67 nm from a tunable Nd:YAG-pumped dye laser to "write" the line and a continuous-wave laser diode outputting 769.455 nm to "read" the tagged line displacement. Despite only a single velocity profile being extracted from a given tunnel run, the campaign yielded an extensive characterization of the facility across its operation envelope. An example of the experimental results from the highest stagnation enthalpy run conditions tested (16 MJ/kg) is shown in Fig. 25. There, the freestream velocity was measured at 4940 m/s. Overall, the measurements conducted in both synthetic air/krypton and nitrogen/krypton flows agreed well with the computationally predicted test conditions to within the experimental uncertainty, which ranged between 5-10%.

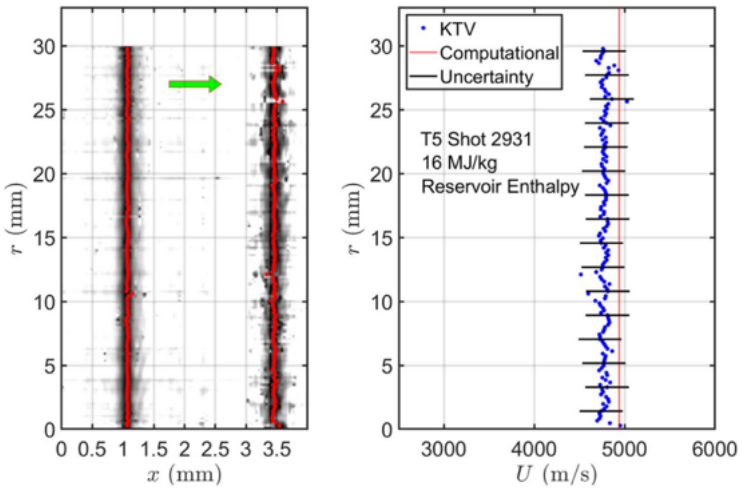

Fig. 25 KTV implementation results from one of the T5 Reflected-Shock Tunnel runs showing both post-processed MTV image and the extracted velocity profile. Adapted with authors' permission from Shekhtman *et al.* [121].

All the freestream characterization examples above represented low-repetition-rate implementations of MTV in high-speed ground testing, which are incapable of capturing some of the high-frequency phenomena, such as mixing and embedded acoustic disturbance propagation, which may have frequencies exceeding 100s of kHz [122]. Additionally, low acquisition rate measurements in short runtime ground-testing facilities, such as shock-driven tunnels, are incapable of providing sufficient statistics required for RANS-based modeling validation. However, as ultra-high-speed pulse-burst technology started to mature, the MTV techniques advanced to the required repetition rates to address the aforementioned need [123]. For instance, in the work by Jiang *et al.* [124], the authors present both 100 kHz PLEET and 100 kHz KTV measurements performed at the AEDC Tunnel 9. A custom 100-picosecond pulse-burst laser outputting 1064 nm radiation was used for the high-speed PLEET part of the work and successfully tagged the Mach 18 nitrogen flow after focusing the beam with a 1000 mm focal length lens across a 10 ms burst. For KTV, the authors utilized a modified "single UV pulse + CW Near-IR beam" scheme by producing a 1 ms burst of 212.6 nm radiation with a custom burst-mode OPO and re-exciting krypton atoms with a CW 769 nm diode laser for enhanced MTV signal. The results of these measurements are summarized in Fig. 26. Overall, the velocity measurements agreed well with the tunnel estimates and suggested maximum freestream velocity fluctuations do not exceed 1.5% in time. The computed velocity

fluctuation was limited by the measurement uncertainty and as a result represents the upper bound of the true flow-field temporal fluctuations.

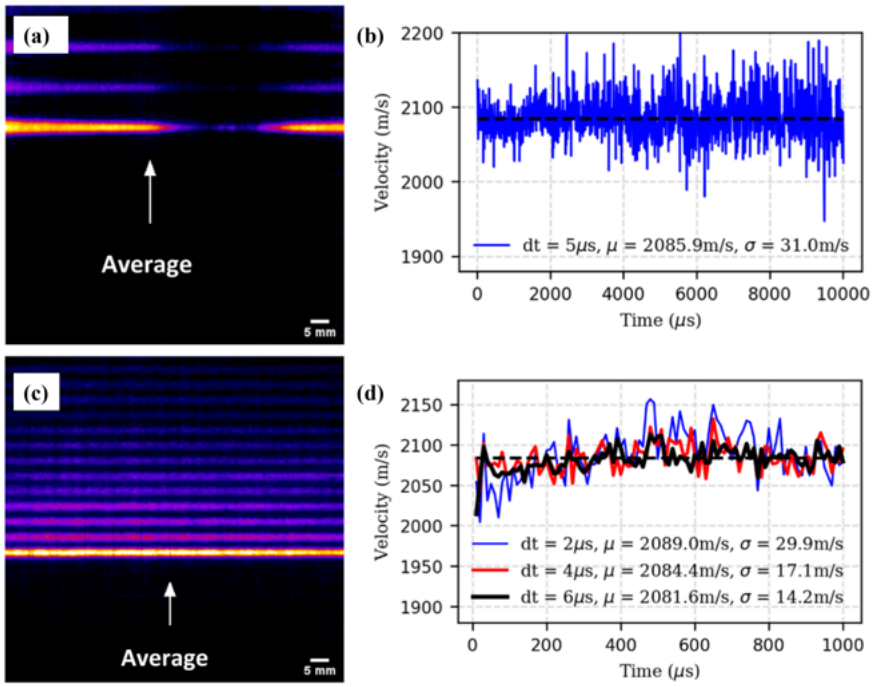

Fig. 26 Experimental results summary of 100 kHz PLEET (a)-(b) and 100 kHz KTV (c)-(d) measurements performed in the AEDC Tunnel 9 Mach 18 nitrogen freestream. Subfigures (b) and (d) show the instantaneous velocity fluctuations averaged over the whole region of interest for PLEET and KTV, respectively. Adapted with author permission from Jiang *et al.* [124]. © 2023 Optica Publishing Group.

The most recent example of this section continues the theme of temporal characterization of high-frequency freestream fluctuations and doubles as the first experimental demonstration of Nitric-oxide ionization-induced Flow Tagging and Imaging (NiiFTI). In the work by Leonov *et al.* [69], the authors implemented two-photon resonant ionization of nitric oxide with subsequent observation of long-lived visible/near-IR fluorescence for 250 kHz velocimetry. The work was done in a low-enthalpy Mach 6 air flow seeded with nitric oxide in the Texas A&M Actively Controlled Expansion Tunnel (ACE). Seeding levels did not exceed 1%. The experimental setup consisted of a Spectral Energies QuasiMODO Nd:YAG MOPA pulse burst laser pumping a custom OPO to generate the 226 nm radiation and a single intensified high-speed camera equipped with 500 nm long-pass filters. Figure 27 summarizes the results of NiiFTI implementation for 250 kHz flow tagging. The persistence of the phosphorescent emission, which lasts for 45 μs under the freestream conditions of 57 K and 413 Pa, enables multiple lines to be tagged and followed, with preceding lines seen displaced by the flow. Additionally, the long fluorescence lifetime alleviated the need for fluorescence decay correction discussed in Sec. IV.C. The camera gate times are delayed by 200 ns and 1.4 μs with respect to the laser pulse, thereby avoiding direct exposure to the scattered laser light and strong nitric oxide ultraviolet fluorescence. The spatially-integrated single-shot freestream velocity of 860 m/s was measured with a shot-to-shot standard deviation of as low as 3.4 m/s, corresponding to 0.4% velocity fluctuations. Considering that the typical freestream fluctuations measured in this tunnel are around 1.5%, this measurement suggests a small spatial scale and low temporal frequency of the dominant freestream fluctuations.

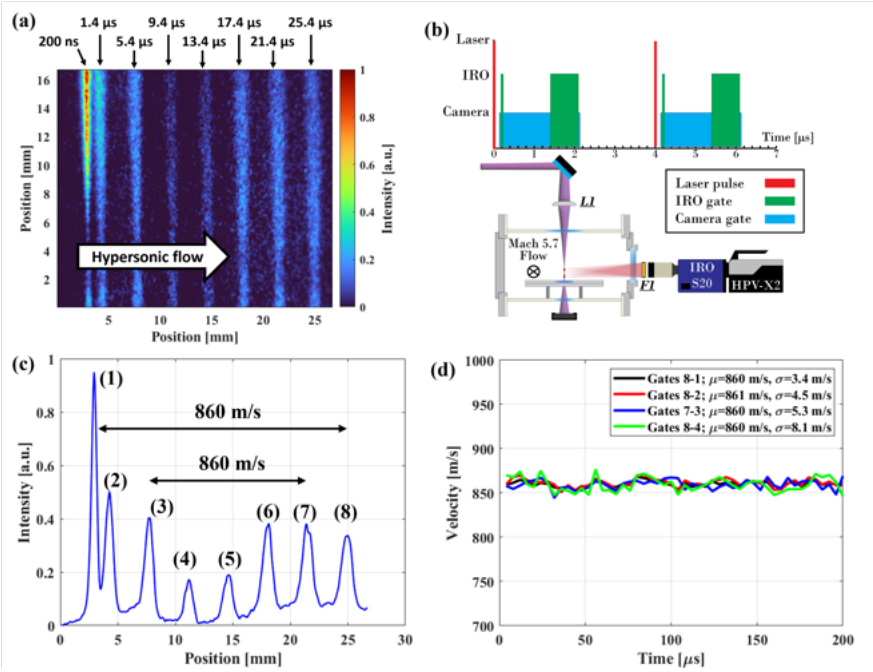

Fig. 27 Summary of 250 kHz NiiFTI demonstration in Mach 5.7 flow: (a) average NiiFTI image, (b) schematic of the experimental setup and the time diagram, (c) spatially integrated NiiFTI signal showing line displacement, (d) single-shot velocity measured across the laser burst. Adapted with permission from Leonov *et al.* [69] © Optica Publishing Group.

.

B. Boundary Layers

Boundary layers are perhaps the primary area of aerodynamic concern in modern high-speed aerothermodynamics because they are directly in contact with the vehicle surface and set the boundary conditions and requirements for thermal protection systems, vehicle control systems, and other key aspects of high-speed vehicles. From a measurement perspective, high-speed boundary layers present numerous challenges, including their relatively small scale, the reduced density as temperature increases while flow slows due to frictional forces, and the potential for transitional and turbulent fluctuations at a range of temporal and spatial scales. The following examples provide a small sample of the successful applications of molecular tagging velocimetry for characterization of high-speed boundary layer flows. Many other works also feature boundary layer measurements [85, 86, 99, 101, 125–127].

One of the early successes of the FLEET technique in an applied environment was its application for measuring the turbulent boundary layer on a hollow cylinder model in AEDC Tunnel 9 at Mach 10 conditions, which was done by Dogariu *et al.* [103]. Results from the measurement are shown in Fig. 28, with comparisons to PIV and basic RANS CFD showing excellent agreement. This experiment was also among the first to utilize a tangent orientation of the beam to mitigate laser-surface interactions (see Section V for more on this topic). The FLEET technique was especially well suited for Tunnel 9 due to its operation with pure molecular nitrogen as the test gas instead of air to avoid liquefaction. However, the large scale of the tunnel still made signal collection a challenge.

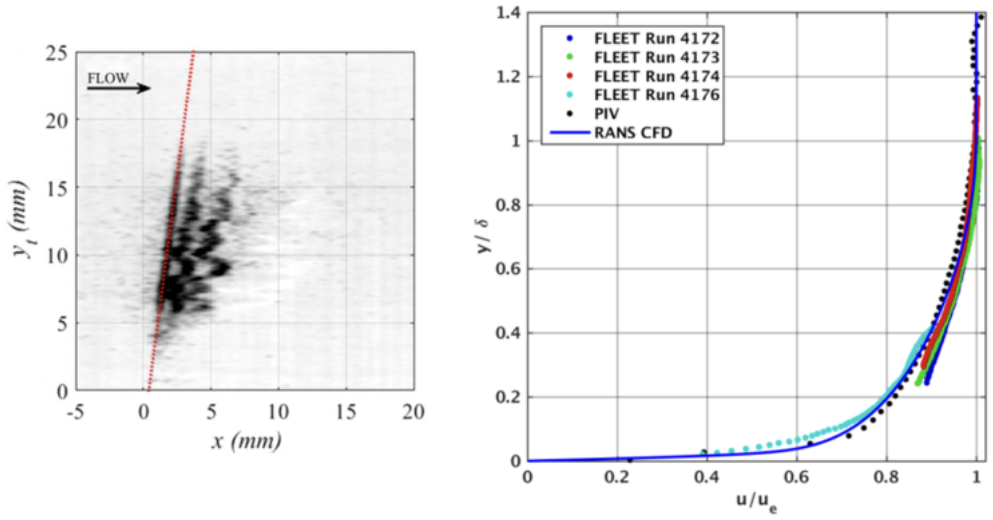

Fig. 28 Results from Dogariu et al. [103] showing FLEET measurements of a turbulent boundary layer on a hollow-cylinder model in Mach 10 flow at AEDC Tunnel 9. Adapted from Dogariu *et al.* [103] © 2019 by the American Institute of Aeronautics and Astronautics. Work of the U.S. Government.

Figures 29 and 30 show results by Segall *et al.* [128], where the turbulent boundary layer region on a hollow-cylinder-flare geometry was measured in the Stevens Shock Tunnel [129]. The tagging was done by targeting acetone seeded into the driven tube prior to the tunnel firing. The velocity profiles are presented in viscous units in Fig. 29 utilizing the van Driest transformation (see Section VII for a general discussion of that process) and show that near-wall measurements were able to be made as low as $y^+ \approx 3$. Figure 29 also shows that the data was in good agreement with log-law and viscous sublayer expected trends, as well as results for DNS. Figure 30 provides information from analysis of instantaneous measurements from the same experiment to examine the validity of Morkovin's hypothesis. The acetone tagging results show good agreement with PIV and DNS, but show slightly better agreement with DNS than the PIV does near $y/\delta \approx 0.1$. Values at $y/\delta \approx 0.04$ are believed to be corrupted by laser-surface interactions and measurement uncertainty.

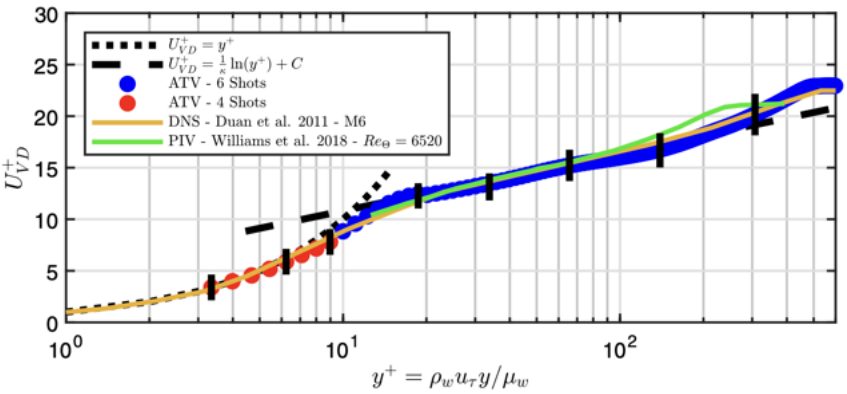

Fig. 29 Acetone tagging velocimetry results by Segall *et al.* [128], with the mean turbulent velocity profile plotted in viscous units and compared with PIV and DNS results. Measurements are made as low as $y^+ \approx 3$. Adapted with author permission from [128] © B. Segall, D. Shekhtman, A. Hameed, J. Chen, and N. Parziale.

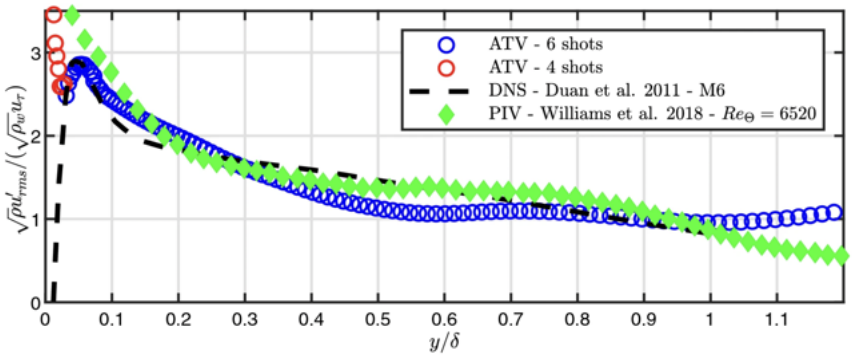

Fig. 30 Work by Segall *et al.* [128] comparing measured turbulent boundary fluctuations with an applied Morkovin scaling to DNS and PIV results. Adapted with author permission from [128] © B. Segall, D. Shekhtman, A. Hameed, J. Chen, and N. Parziale.

Segall et al. [130, 131] report boundary-layer profiles of the streamwise mean and streamwise/wall-normal RMS fluctuations, $(\overline{u}, \overline{v}, u'_{\mathrm{RMS}}, , v'_{\mathrm{RMS}})$, obtained with Krypton Tagging Velocimetry (KTV) at 100 kHz in a hypersonic, turbulent, zero-pressure-gradient boundary layer. A novel wall-normal measurement strategy is included as Fig. 31. They examine two operating conditions: a 'cold-flow' case with ($M_\infty = 6.4$, $T_w/T_r = 0.54$, $Re_\tau = 450$) and an 'enthalpy-matched' case with ($M_\infty = 6.0, T_w/T_r = 0.17, Re_\tau = 780$). Nondimensional profiles down to $y^+ \approx 3-6$ are available Fig. 32. After applying Morkovin scaling to account for mean-density variation across the boundary layer, they show that the KTV and DNS data collapse onto incompressible laser-Doppler anemometry (LDA) benchmarks within experimental uncertainty down to $y/\delta \approx 0.1$. They conclude that these, shown in Fig. 33, support Morkovin's hypothesis for supersonic and hypersonic compressible turbulence and constitute, to their knowledge, the first wall-normal fluctuation measurements to substantiate the 1962 hypothesis.

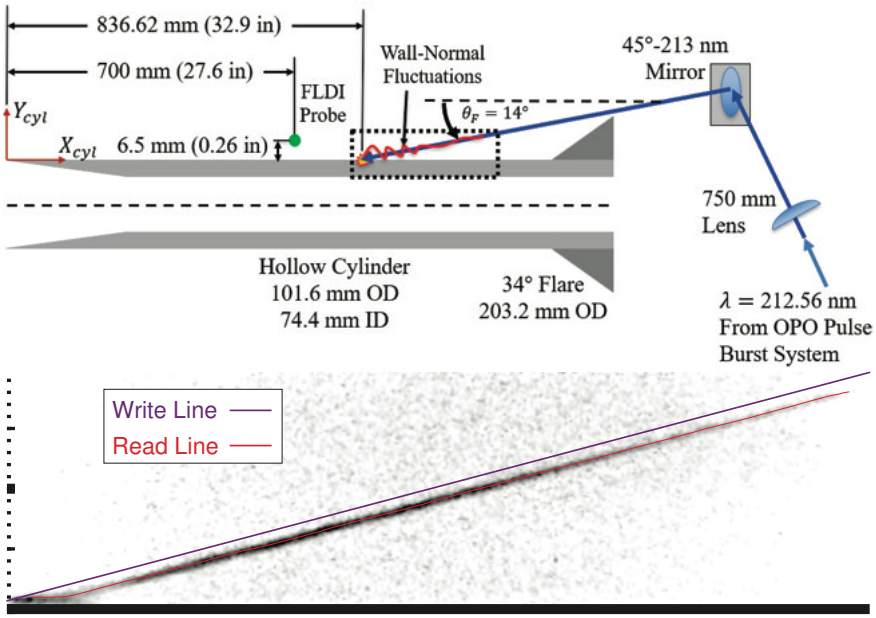

Fig. 31 Schematic of KTV wall-normal fluctuation measurement in Segall et al. [131]. Top: Side view of HCF and wall-normal fluctuation setup. Bottom: Sample wall-normal exposure with fitted line.

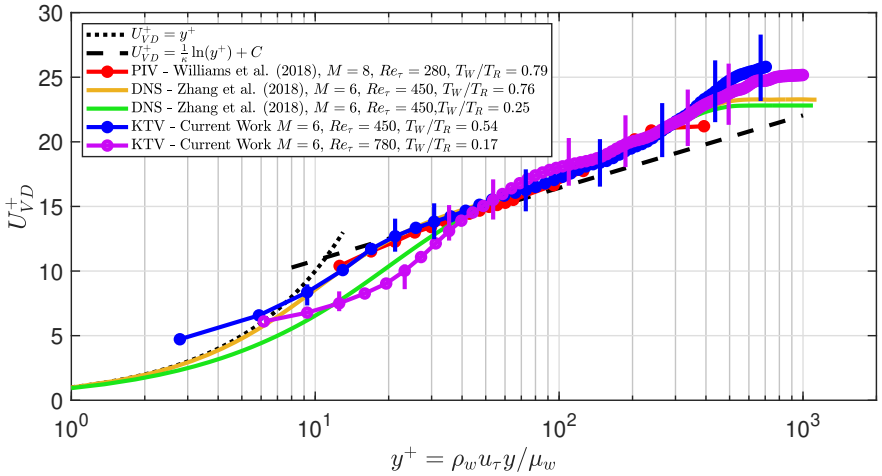

Fig. 32 van Driest non-dimensionalization of KTV data from Segall et al. [131] and comparison to DNS.

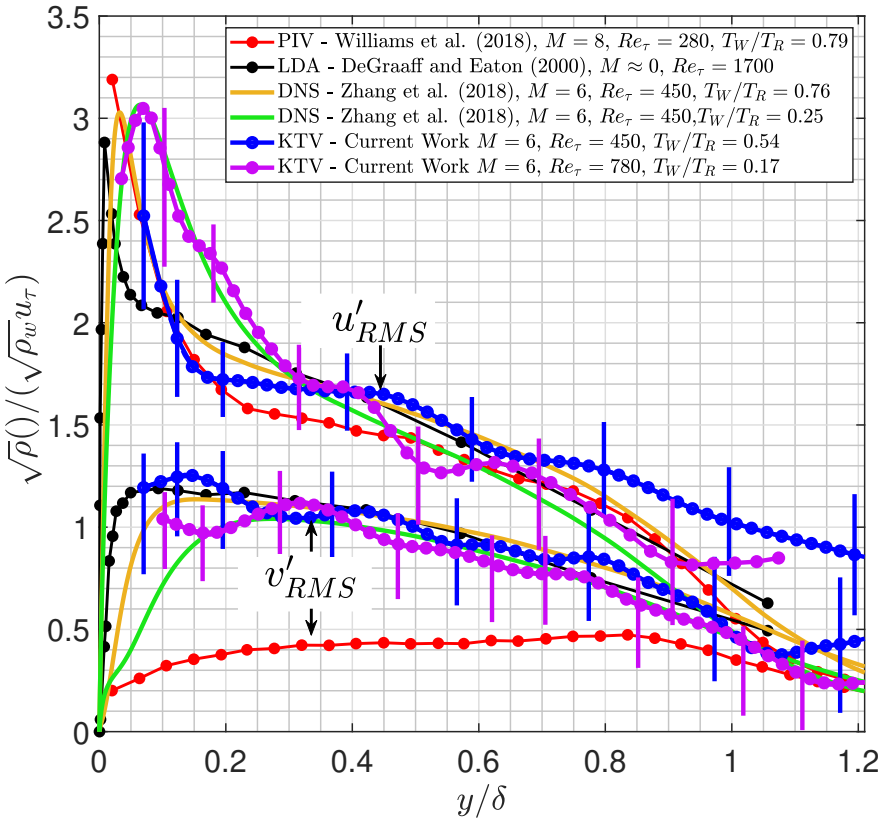

Fig. 33 Morkovin scaled $u'_{\mathbf{RMS}}$ and $v'_{\mathbf{RMS}}$ for KTV experimental data (present work plotted every fifth point) compared to DNS, LDA, and PIV (plotted every other data point) from Segall et al. [131].

MTV has also been used to study high-speed transitional boundary layers [102, 132]. Hill *et al.* [132] used FLEET velocimetry to study the effect of nose bluntness on boundary layer transition in a Mach 6 Ludwieg tube. Work by Webber *et al.* [102] is shown in Fig. 34, where FLEET velocimetry was used to measure the boundary layer velocity profiles at several positions in the transitional region on a hollow cylinder in Mach 7 flow. The velocity data is presented as a color map in Fig. 34(b) to show that the redistribution of momentum towards the surface coincides with increasing skin-friction values determined from the fitting of velocity profiles.

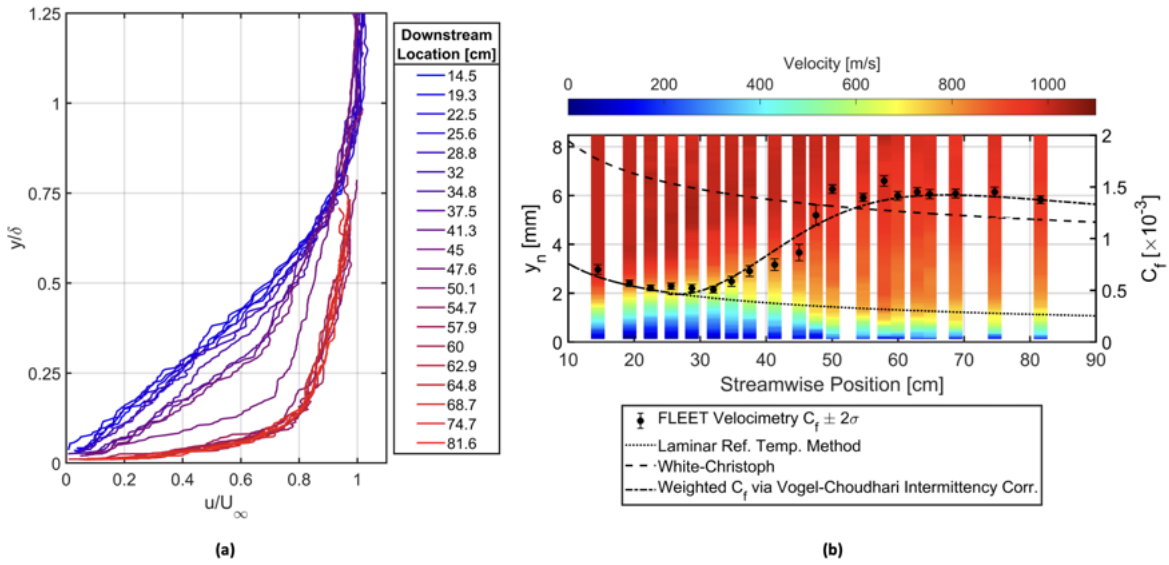

Fig. 34 FLEET velocimetry results by Webber *et al.* [102, 133] in the transitional boundary layer region on a hollow-cylinder model in Mach 7 flow. (a) Shows normalized velocity profiles at each location and (b) shows a color map of the transitional region based on velocity, with skin-friction computed from the velocity data shown on the right axis. Adapted with author permission from Webber *et al.* [102, 133].

Recently, NiiFTI was also applied for near-surface boundary layer velocimetry in both low and high enthalpy conditions in a blowdown and expansion tunnels [73, 74]. An ogive hypersonic model was chosen as it provides a favorable pressure gradient, and a platform for studying competing mechanisms in turbulence production processes. In this example, a 10 Hz dye laser was employed to generate the 226 nm beam, while the rest of the optical and diagnostics setup remained the same as in the example in the section above. By passing the laser at grazing incidence across the ogive test article, the flow was tagged simultaneously at varying distances up to less than a millimeter from the model surface while avoiding laser generated surface ablation, which is typical in experiments where the laser beam intersects with the model surface. Figure 35 shows the tagged flow at two temporal delays from which the boundary layer velocity profile can be acquired. Here, the velocities near 870 m/s were calculated outside the boundary layer. The boundary layer was profiled as close as 0.25 - 0.5 mm from the model surface, corresponding to the minimum recorded velocity of 122 m/s.

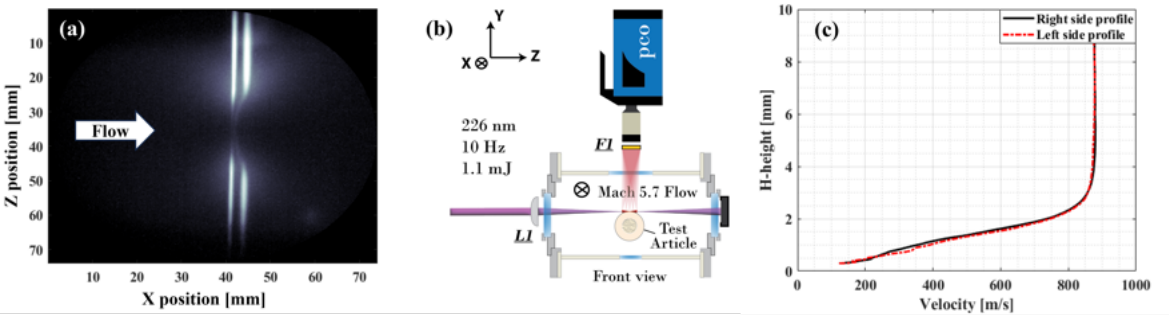

Fig. 35 Near-surface flow tagging and boundary layer velocimetry for an ogive mode using 10 Hz NiiFTI. Adapted with permission from Leonov *et al.* [74]

C. Wakes

Wakes are an extremely important region of many high-speed-flow fields, as they often are associated with flow separation, transitional-turbulent free shear layers, nonequilibrium thermochemistry, and potentially even sparse gas behavior, all of which are still challenging phenomena for modern CFD. Measurements in wakes are therefore critical to developing better computational modeling tools, and several researchers have used MTV to extract velocity information in these regions [59, 60, 134, 135].

Figure 36 shows an excellent example of MTV being used to study the wake region behind a hypersonic sphere in the Sandia reflected shock tunnel [60]. Due to the total enthalpy of the flow, the measurement made use of naturally produced NO, eliminating the need for gas seeding. Qualitative comparison of results with CFD in Fig. 36(c) shows relatively good agreement. Note that for such a facility, it would be impractical to attempt a PIV measurement due to the nature of the impulse-style tunnel as well as the high Mach number.

Another successful application of MTV for wake measurements is shown in Fig. 37, based on work at the NASA Langley Research Center. This measurement was done in the NASA Langley Mach 10 blowdown facility, which lacks the total enthalpy to naturally produce NO via dissociation of air molecules. Thus, NO was seeded into the flow. A diffractive optic was used to split the single excitation beam into 75 laser beams, which greatly increased the measurement field per laser shot. Radial profiles of the streamwise velocity component are shown in Fig. 38 for several axial positions from the velocity map in Fig. 37.

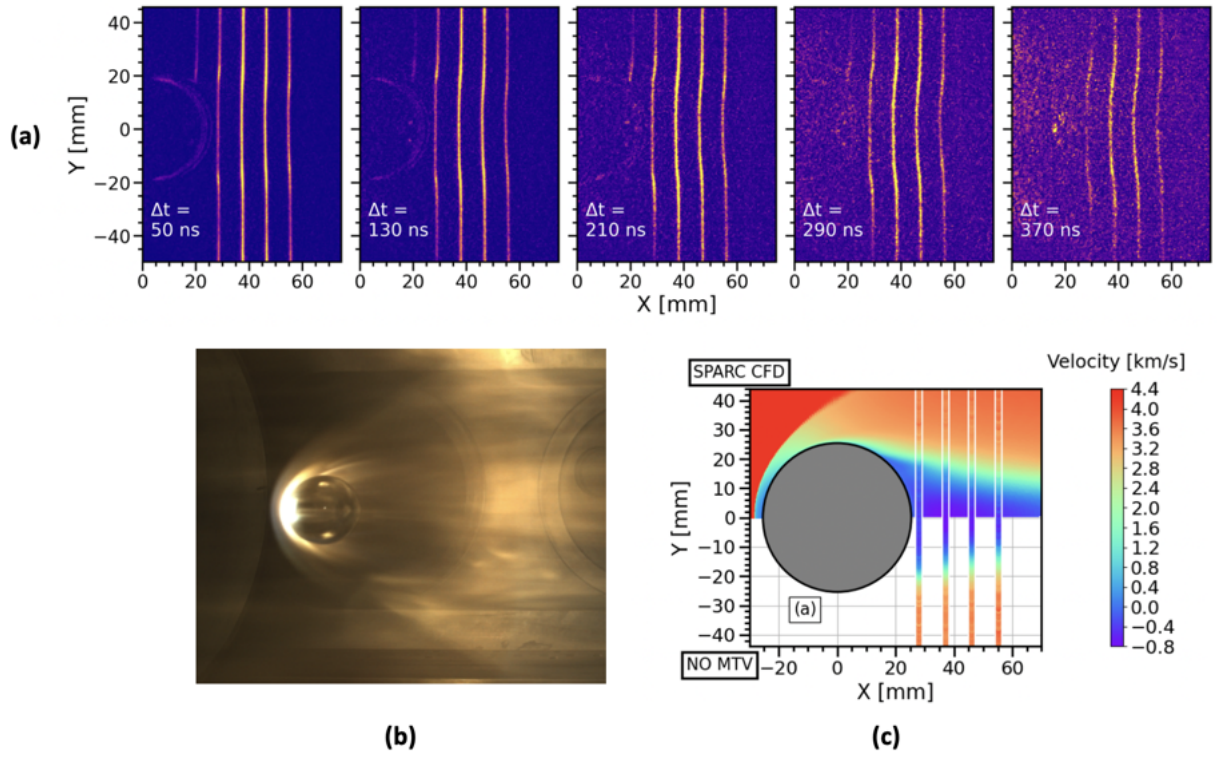

Fig. 36 Work by Jans et al. [60] in the Sandia reflected shock tunnel where NO molecular tagging velocimetry was used to measure the wake on free-flight sphere. (a) shows images of the tagging relative to the sphere, (b) shows an actual image of the model during the tunnel run, and (c) shows a comparison of the data with CFD. Conditions were at Mach 8.8 with a total enthalpy greater than 10 MJ/kg. Adapted with permission from [60] © 2025 Optica Publishing Group.

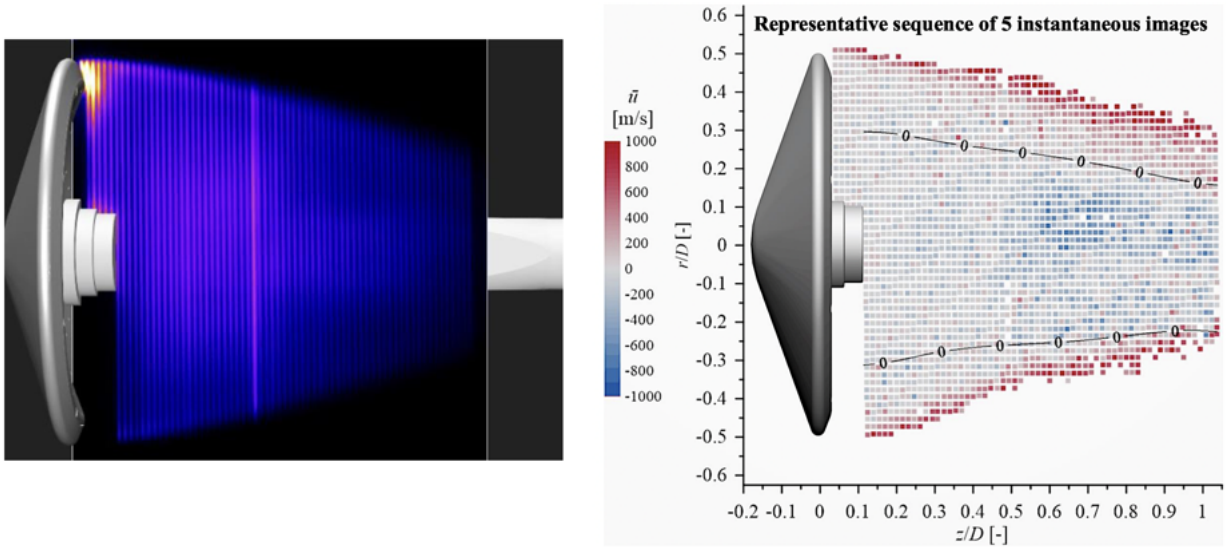

Fig. 37 Work by Rodrigues *et al.* [59] in the NASA Langley Mach 10 facility using NO tagging to measure the wake region behind a sphere-cone model. A diffractive optic was used to simultaneously write over 70 lines with one pulse. Adapted with author permission from [59]. Work of the U.S. Government.

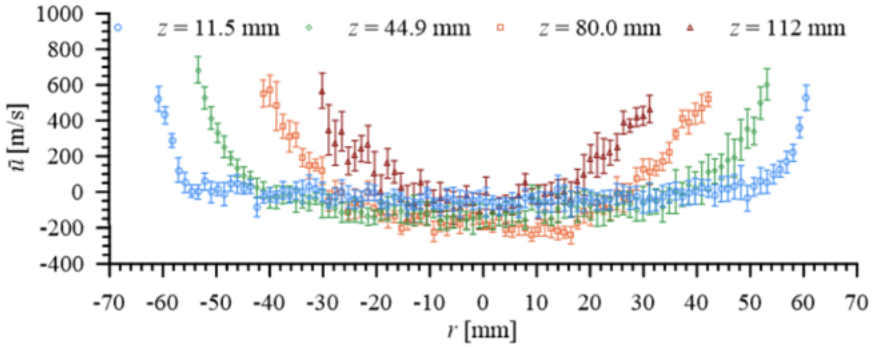

Fig. 38 A plot of wake velocity profiles from various axial locations in Fig. 37. Adapted with author permission from [59]. Work of the U.S. Government.

D. Propulsion Related Flow-Fields

There is limited application of MTV to high-speed propulsion flow-fields, especially with active combustion. However, the technique is extremely well suited for such measurements, given that water and OH can be naturally generated by hydrogen and hydrocarbon combustion.

An example of OH tagging applied in a non-reacting high-speed flow relevant to hypersonic air-breathing propulsion comes from the work of Lahr *et al.* [90]. The flow-field of interest in that work was a relatively large cavity, which is typically used in ramjet and scramjet propulsion to increase fuel residence time, increase mixing, and as a flame holder to stabilize ignition. As shown in the schlieren image and diagram in Fig. 39(a), the backward-facing step results in a large free shear layer across the top of the cavity and the cavity itself has a recirculation aspect to it, along with some degree of vortex shedding. In all, it is a very complicated flow-field with various scales of unsteadiness and transport. As shown in Fig. 40, a two-dimensional OH tagging approach was used to obtain mean and instantaneous velocity fields across the span of the cavity, with measurements repeated at several wall-normal heights relative to the top of the cavity. The resulting velocity profiles for several positions in the cavity are presented in Fig. 41, which the reversed flow inside the cavity associated with the recirculation region and the forward flow in the free shear layer.

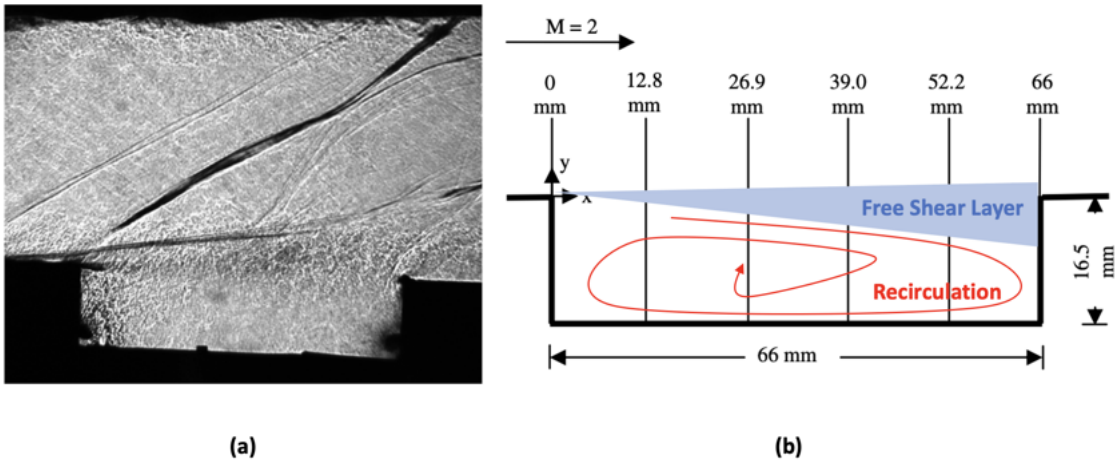

Fig. 39 (a) A schlieren image and (b) illustration of the cavity flow studied by Lahr *et al.* [90]. Adapted with from [90] © 2010 by the American Institute of Aeronautics and Astronautics. Work of the U.S. Government.

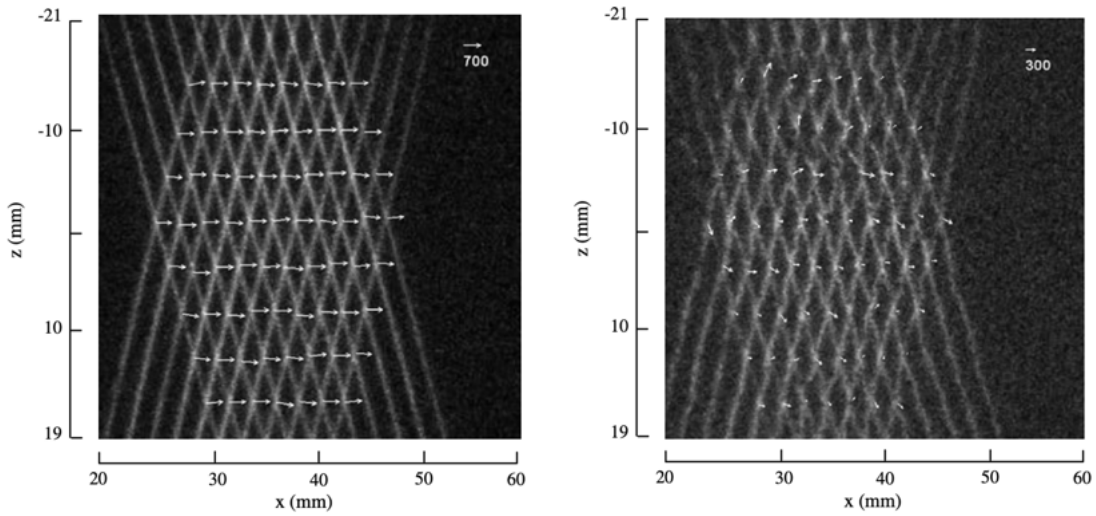

Fig. 40 Examples of mean and instantaneous images of the two-dimensional OH tagging used in the experiment by Lahr *et al.* [90]. Adapted from [90] © 2010 by the American Institute of Aeronautics and Astronautics. Work of the U.S. Government.

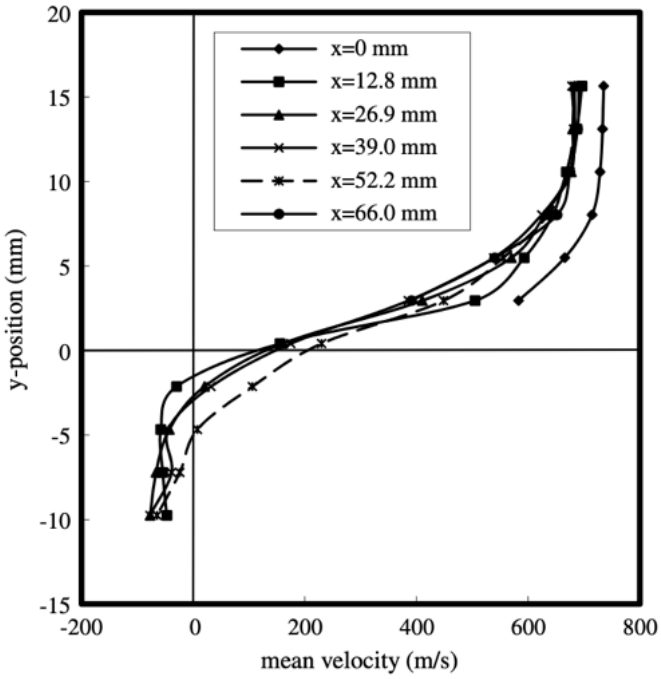

Fig. 41 Velocity profiles obtained by Lahr *et al.* [90] for the flow-field near the flame holder cavity in Fig. 39 using OH tagging. Adapted with from [90] © 2010 by the American Institute of Aeronautics and Astronautics. Work of the U.S. Government.

Another propulsion-related flow-field of interest for the Aerodynamic Measurement Technology community is a transverse jet in a supersonic or hypersonic crossflow. The two most common scenarios to encounter such a flow-field are: 1) fuel-oxidizer mixture injection into the core flow of scramjet combustors, and 2) control jets as part of either reaction or thrust vectoring systems. Such wide utilization and importance for high-speed propulsion and maneuvering applications make transverse jets in a high-speed crossflow an important area of both experimental and computational research for more than a few decades [136, 137]. In addition to a complicated shock structure with multiple recirculation regions, these jets are characterized by high frequencies of mixing processes, strong multi-dimensional vorticity, and overall highly transient behavior, setting high requirements for MTV applications. Recently, single-shot NiiFTI was applied to study the interaction of a Mach 3 overexpanded transverse jet of nitrogen and a "low-enthalpy" Mach 5.7 core flow, as shown in Fig. 42 (left) [75]. Due to the low temperature of both flows, the nitrogen jet was seeded with 2% nitric oxide. In this work, Leonov and Miles demonstrated the use of a tunable Nd:YAG 5th harmonic output at 213 nm for molecular tagging velocimetry for the first time. Despite negligibly low theoretical NO absorption of 213 nm radiation at temperatures below 300 K, NiiFTI benefited from the quasi-resonant two-photon ionization and proved to tag the flow with this excitation scheme effectively as represented with a sequence of raw NiiFTI images in Fig. 42 (right). Here NiiFTI was implemented at a 200 kHz laser repetition rate and benefited from a long fluorescence lifetime of around 40 μs. As a result, each camera frame in Fig. 42 shows multiple tagged lines corresponding to previous laser pulses convecting downstream despite having only a single camera exposure synchronized with the laser. Since each frame contained information about a few previously tagged lines, the authors were able to trace the evolution of each individual tagged fluid element across a number of frames and measure the velocity changes in space from Lagrangian stand-point. The results for one of the tagged fluid elements are presented in Fig. 43. Figure 43(a) shows line positions extracted from five consecutive images in red and normalized velocity vectors in blue. Figures 43(b-c) present extracted horizontal and vertical velocity components, respectively, in blue. Given successful velocity measurement at multiple spatial locations for a single fluid element, the authors were able to calculate flow acceleration similarly to the previous work by Danehy *et al.* [138], where the authors measured three components of velocity and acceleration using FLEET and stereoscopic imaging.

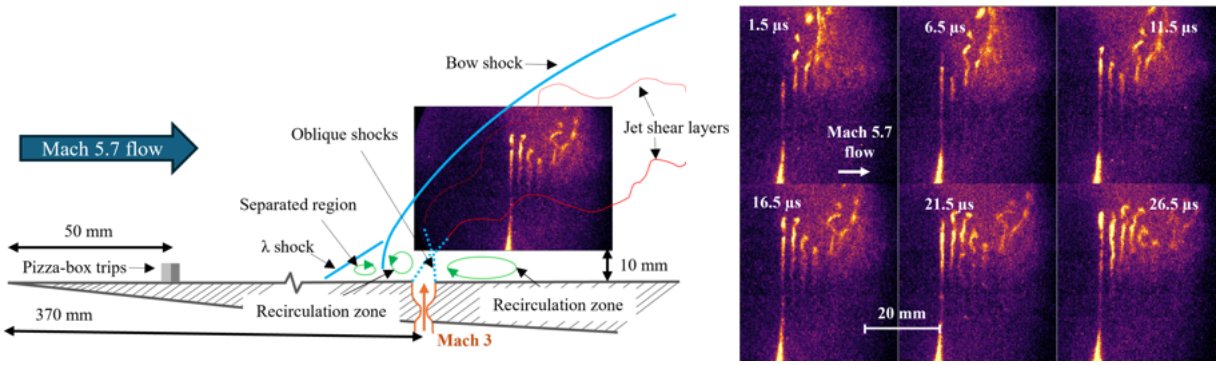

Fig. 42 Supersonic crossflow flow-field schematic with one of the raw images overlaid to show the measurement location (left); six consecutive representative images (right). Adapted with permission from [75] © Optica Publishing Group.

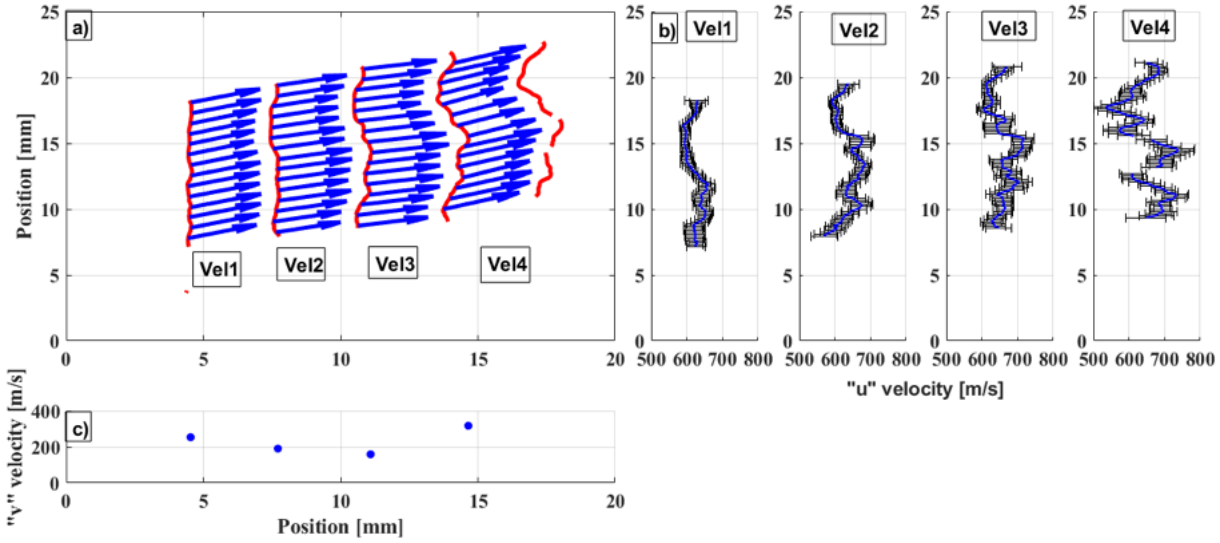

Fig. 43 Results for one of the flow tags: a) Measured velocity vectors (blue) overlapping the tagged line positions (red); b) measured horizontal "u" velocity component with appropriate confidence intervals; c) measured vertical "v" velocity component. Adapted with permission from [75] © Optica Publishing Group.

E. Shear Flows

Similarly to wakes, when high-speed geometries feature an inward-deflection of the flow along the surface it can lead to separation and an associated separated shear layer. Particularly for the semi-canonical cone-slice-ramp geometry studied at Sandia (Fig. 44), which features an expansion in the form of a planar slice along the axis of a cone followed by a 2D compression ramp, the expansion separates the flow due to the influence of the downstream ramp. For the case of a turbulent boundary layer, the separation itself can lead to relaminarization of the flow near the wall [139]. This presents challenging conditions for MTV, not only because the velocimetry is performed in proximity to a wall, but also because the flow features strong gradients in density and velocity across the shear layer that impacts the local signal-to-noise ratio. Profiles of streamwise velocity extracted along the wall-normal direction for three locations along the cone-slice-ramp geometry using FLEET are shown in Fig. 44. Although the reduced separation with increasing Reynolds number is evident from the profiles along the slice, the velocimetry was limited by the single-exposure multiple-gate approach, see Fig. 15(a), that prevented velocities below approximately half of the edge velocity from being resolved. In addition, the gradients in density adversely impacted the local signal-to-noise ratio near the wall: highlighting the challenging nature of MTV in shear layers with strong gradients.

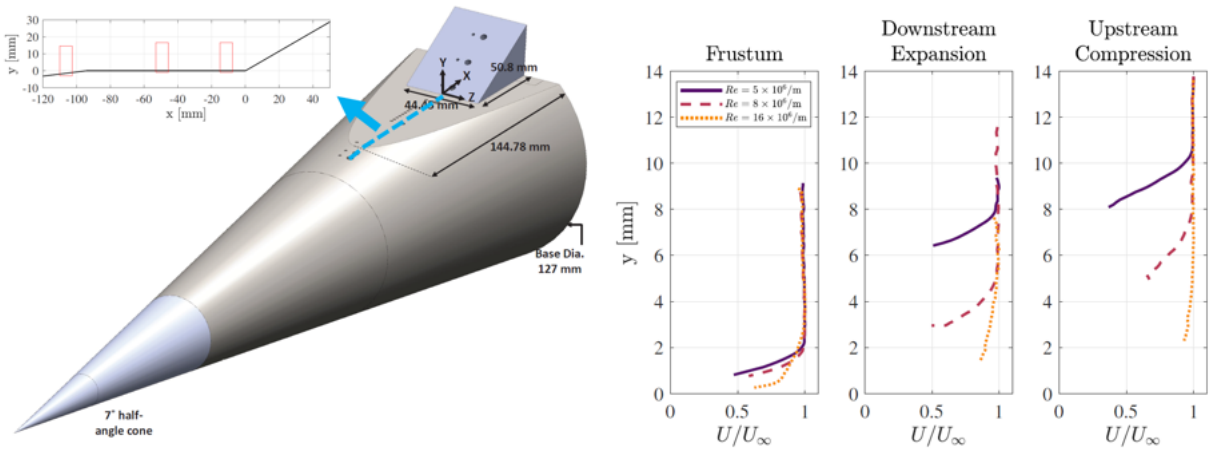

Fig. 44 The Sandia expansion-compression cone-slice-ramp geometry with measurement locations indicated (left) and extracted profiles of streamwise velocity from FLEET (right) at three Reynolds numbers corresponding to laminar (solid), transitional (dashed), and fully turbulent (dotted) boundary layers along the cone, from Carter *et al.* [127]. Adapted with permission from [127] © The American Institute of Aeronautics and Astronautics.

Another example of a high-speed shear flow is that of a turbulent shockwave-boundary layer interaction (SBLI), for example at a 2D compression corner. In Mustafa et al. [140, 141, 142], the authors quantify how compression-corner angle influences streamwise turbulent kinetic energy (sTKE) and coherent structure in Mach 2.8 flow. Krypton Tagging Velocimetry (KTV) measurements are acquired in the incoming turbulent boundary layer and over 8°, 16°, 24°, and 32° compression corners. Experiments employ a 99% N_2/1% Kr mixture in the AEDC Mach 3 Calibration Tunnel (M3CT) at $Re_\Theta = 1750$. They introduce a wall-normal integral measure, $\overline{\text{sTKE}}$, that combines the root-mean-squared streamwise fluctuations with the local shear-layer width to capture net turbulence amplification across geometries. To interrogate organization in the velocity field, they applied snapshot proper orthogonal decomposition (POD) to the KTV data, extract the dominant modes, and compare cases via mean-velocity maps conditioned on the largest positive and negative POD coefficients.

Fig. 45 shows sample KTV read exposures for Mach 2.8 shock-wave/turbulent boundary layer interaction. This is the visualization of the $5p[3/2]_1 \rightarrow 5s[3/2]_1^o$ (829.8 nm) transitions. Mach 2.8 flow is left to right and the walls in each corner flow are marked in black. Animations of instantaneous fluorescence exposures and corresponding velocity profiles are provided as supplementary material in [142].

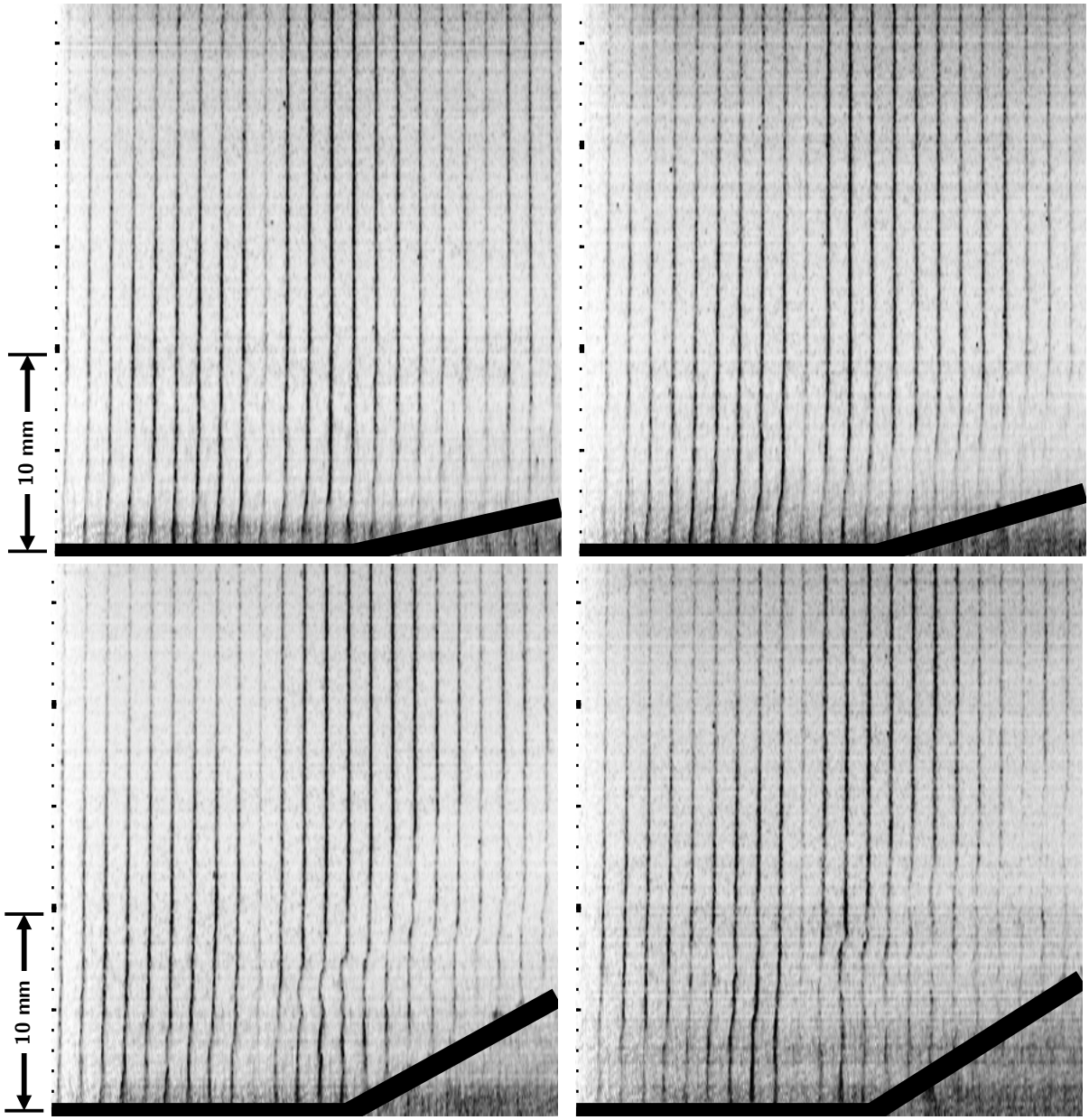

Fig. 45 Sample instantaneous shock-wave/turbulent boundary-layer interaction fluorescence exposures for the (a) 8 degree, (b) 16 degree, (c) 24 degree and (d) 32 degree corners, respectively. These are ostensibly boundary-layer profiles traces with a 500 ns prescribed delay between the write and read step. Major tick marks are 10 mm. Flow is left to right. Inverted intensity scale. Wall marked as black. Animations of instantaneous fluorescence exposures and corresponding velocity profiles are provided as supplementary material in [142].

VI. MTV Associated Challenges

While molecular tagging velocimetry is becoming more widespread in use for high-speed flow measurements, it still has many challenges to overcome before reaching the level of use and regularity of particle image velocimetry (PIV).

A. Gas Seeding

Molecular tagging velocimetry techniques that don't require seeding, such as FLEET in nitrogen/air tunnels and NO-MTV in arc jet tunnels, are highly desirable. However, most MTV techniques will require the seeding of some trace target species that will be excited by intense laser light. Most hypersonic facilities are, in fact, impulse facilities, which utilize pressurized tubes filled entirely with the test gas prior to the run. Here, the seeding can be relatively straightforward, but care has to be taken to avoid depletion of a tracer gas through chemical reaction (*e.g.* NO interacting with the oxygen in air and decreasing in concentration), and some tracer elements may not stay homogeneously mixed after long periods of time associated with pre-run experimental preparations (such as pumping the test article to vacuum). In some cases, seeded gases can pose occupational risk, such as NO (highly toxic) or acetone (flammable). Also, in hypersonic flows with sufficient enthalpy, chemical reactions can occur in stagnation regions or even upstream of the nozzle in the stagnation chamber. Unless chemically inert (such as krypton or molecular nitrogen), there is the potential for seeded gases to interfere with these chemical reactions and perhaps change the thermochemistry of the hypersonic flow. Therefore, among seeded MTV techniques, those that rely on seeding with an inert gas are more desirable.

For blowdown tunnels, gas seeding for MTV is similar to particle seeding practices for PIV, which are typically referred to as "much more art than science." The primary consideration for these types of facilities is seeding uniformity, which is very much dependent on the nozzle mass flow rate. Figure 46 shows an example of a seeding wand used in the 9" by 14" Texas A&M ACE tunnel, which is discussed by Buen *et al.* [53]. This seeding wand was placed upstream of the flow screen to minimize turbulence in the flow upstream of the nozzle.

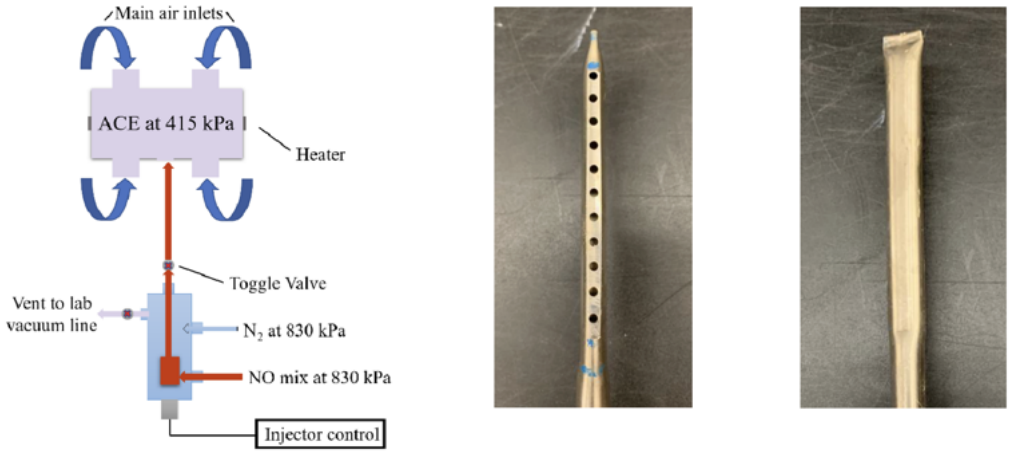

Fig. 46 Example of the gas seeding system used in the Texas A&M ACE tunnel, as described by Buen *et al.* [53]. Adapted with permission from [53] © 2020 by the American Institute of Aeronautics and Astronautics.

While the above concerns should be considered in any application, it is also important to note that most techniques require relatively low concentrations of the target molecules, approximately 1-2% by volume.

B. Increased Measurement Capabilities: Space and Time

Another challenge for MTV is increasing spatial measurement capabilities, which includes both higher-dimensional measurements (simultaneous 2-component velocity rather than only 1-component velocity) and measurements at multiple locations. Particle image velocimetry typically provides a global, planar snapshot of the velocity field in two components, which greatly increases its value for flow field measurements and enables derived quantities such as vorticity to be measured. Generally, MTV is not capable of providing the same level of spatial information as PIV. Some work has been done using arrays of MTV lines to get two velocity components in high-speed flows [90, 104, 105] (see for example, Fig. 40). Point array and multiline techniques have also been demonstrated for basic flows [126, 143, 144], and even tomographic measurements have been demonstrated [145]. However, even the processing of typical 1D MTV data is relatively underdeveloped compared to widely used PIV data processing packages, and these higher dimensional data sets are even more cumbersome to work with. Hence, more work is needed to develop experimental configurations that enable planar (or even volumetric) and 2-component (or even 3-component) measurements. Better data analysis

tools are also needed to make MTV data processing simpler, particularly for higher dimensional data sets.

While increasing spatial measurement capability is highly desirable, even just developing consistent and simple approaches to get surface normal velocity in a boundary layer will be beneficial, since this is precisely the type of measurements PIV cannot provide in high-speed flows due to particle response effects. Such measurements are extremely valuable for validating production and dissipation terms in turbulence models and validating conceptual frameworks such as the Morkovin hypothesis.

In consideration of time scales, it is important to note that many ground testing facilities in hypersonic flow research operate as impulse tunnels, including expansion and shock tunnels, which operate with durations on the order of milliseconds. With imaging being the primary mode of detecting MTV lines, there is a significant challenge in obtaining enough data for converged statistics during the steady flow period. Even with state-of-the-art pulse burst laser systems, this challenge remains, as the thermal stability and damage thresholds of laser components used in optical parametric oscillators (OPOs) limits burst durations to a few hundred pulses per burst at high pulse energies. While megahertz rate capabilities do exist, they cannot directly tackle this issue since the cameras needed to image at that rate only record for a limited number of frames with the current technology.

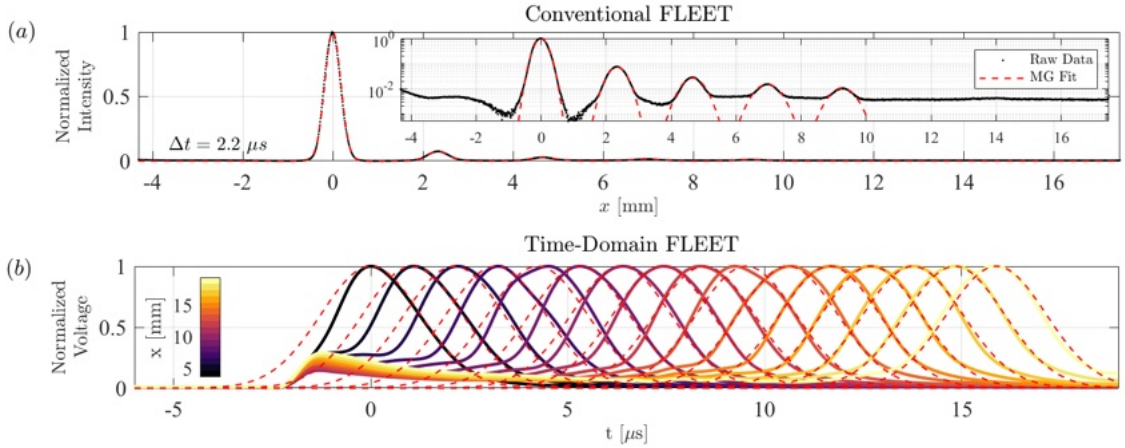

Fig. 47 Normalized vertically-binned ensemble-averaged conventional FLEET image of a Mach 8 freestream flow (a) and normalized intensity distributions of each of 16 streamwise-oriented photodiode array elements from the same flow (b) with multi-Gaussian (MG) fits shown in red dashed lines (adapted from [146]).

To overcome the limitations imposed by imaging at very high speeds, recent work by Carter *et al.* [147, 148] demonstrated the use of a linear photodiode array to track the advection of the excited gas at MHz rates by orienting the array along the streamwise direction. In their case, FLEET was used in a pure-nitrogen flow at Mach 8. A comparison between conventional MTV and the time-domain photodiode array method is shown in Fig. 47 in a uniform free-stream flow. The sequential-in-time peak locations of the photodiode elements demonstrates the feasibility of the time-domain approach, however two sources of significant uncertainty were noted that lead to substantial 7% disagreement with conventional image-based MTV. First, that the transfer function imposed by the image intensifier (that was placed in front of the photodiode) is unknown and likely introduced a bias due to the finite response time of the internal photocathode. Second, that the bi-exponential decay of the FLEET excitation may also impact the apparent peak location in time. The latter was approximated to impact the estimated freestream velocity by 1%, indicating that the image intensifier is dominating the uncertainty. Further disagreement was found when comparing conventional and time-domain measurements in the wake of a seven-degree cone at Mach 8 [146], indicating that flow accelerations are problematic for the photodiode elements whose "pixel" size is significantly larger than the pixels of a typical image sensor. Future efforts on so-called time-domain MTV are recommended to avoid using image intensifiers (*e.g.*, using avalanche photodiodes), as well as photodiodes with as small of a photosensitive area as possible. The use of microlenses in combination with photodiodes may also improve performance.

C. Laser-Surface Interactions

Most MTV-based boundary layer measurements are done with the intent to measure a wall-normal velocity profile, but depending on the laser excitation requirements for the trace species, the laser impingement on the surface can lead to significant local surface damage, creation of artificial flow disturbances, or creation of a weak plasma, as shown in Fig. 48. In this regard, single-photon MTV techniques such as NO-MTV are better suited for near-surface measurements, compared to multi-photon MTV techniques that require significant laser intensity to drive the excitation process. While this area remains a challenge, especially given the importance of near-wall data to CFD validation, a few strategies have been demonstrated. First, several researchers have aimed focused MTV excitation beams into small holes typically used for high-response pressure sensors in the surface of models to help mitigate surface interaction effects. This approach was successfully applied by Hill *et al.* [132], shown in Fig. 49, and Pehrson *et al.* [99]. While such open flows surely introduce some level of flow disturbances, simple RANS computations simulations suggest no significant impact on the local mean flow. However, holes can promote boundary layer instability and affect overall boundary layer transition dynamics. Another issue with this approach is that measurements become limited to regions on the model near the holes. Furthermore, some hypersonic impulse facilities may have appreciable movement during operation, which may cause the beam to miss the target hole, resulting in significant laser scatter and potentially model damage.

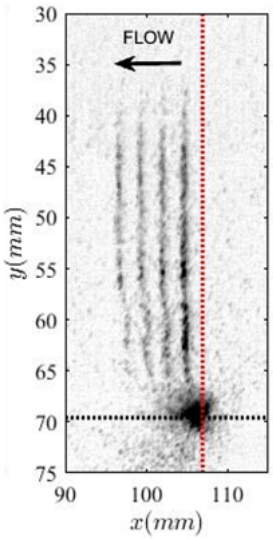

Fig. 48 An example of a laser-surface interaction in the work by Dogariu *et al* using FLEET velocimetry [103]. The black dotted line represents the model surface and the red dotted line represents the inbound laser. Adapted from [103] © 2019 by the American Institute of Aeronautics and Astronautics. Work of the U.S. Government.

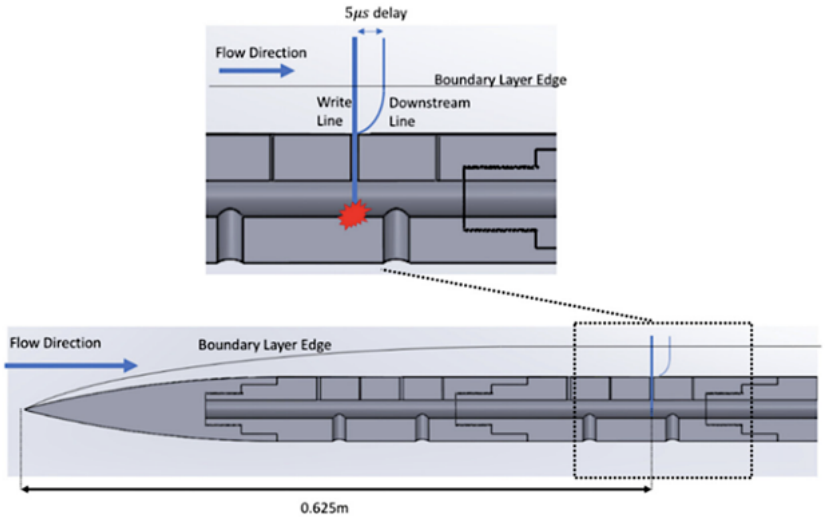

Fig. 49 An illustration from Hill *et al.* [132] demonstrating the use of a small hole in the model to terminate a FLEET excitation beam. Adapted with permission from [132] © 2021 Optical Society of America.

Another approach to avoiding laser-surface interactions applies specifically to axisymmetric flow-fields and models. As shown in Fig. 50, if the flow is truly axisymmetric, then an MTV line can be created tangent to the surface, and each point along the line can be mapped to a specific surface normal height using trigonometry. This approach was used by Dogariu *et al.* [103] for FLEET measurements on a cone in AEDC Tunnel 9, by Leonov *et al.* [73] for NiiFTI measurements of boundary layers on an ogive in Texas A&M's HXT, and by Webber *et al.* [101] for FLEET measurements of a laminar boundary layer on a hollow-cylinder mach in UTSI's Mach 7 Ludwieg tube. The technique has also been used successfully with krypton [125] and acetone [128] tagging velocimetry.

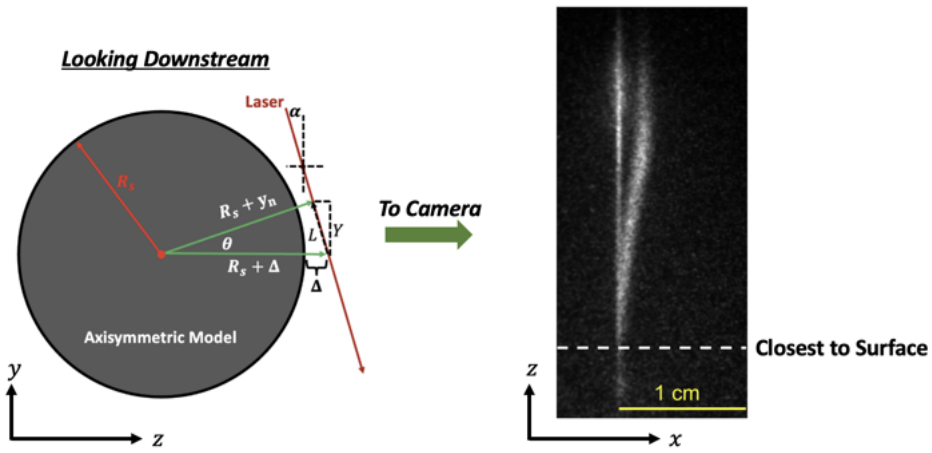

Fig. 50 The generalized geometry of tangent MTV and an example of a FLEET image acquired with this setup. Adapted with author permission from [102] © Nicholas Webber, Sophia Edwards, and Mark Gragston.

Equation 23 can be used to map a position Y on the line in the MTV image to a wall normal position y_n under the assumption that the surface offset Δ was measured as shown in Fig. 50, even with some angle α between the MTV line and vertical axis. R_s is the model radius and α is the angle of the beam relative to an ideal vertical orientation.

$$y_n = \sqrt{(R_s + \Delta)^2 + \frac{Y^2}{\cos^2(\alpha)} - 2(R_s + \Delta)Y\tan(\alpha)} - R_s \tag{23}$$

Note that Eq. 23 reduces to the simplified expressions given by Leonov *et al.* [73] if $\alpha = 0°$. Webber *et al.* [101] showed that this approach gives very good agreement with CFD values for velocity profile and skin-friction, as shown in Fig. 51. It was also shown that the results are highly dependent on the accuracy of the beam angle, thus, significant effort should be made to quantify this during alignment. Sensitivities of this technique are discussed by Webber *et al.* [149], where synthetic MTV data was used to better isolate parametric effects.

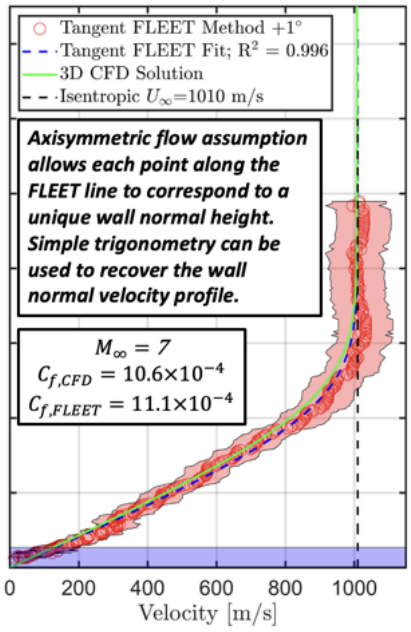

Fig. 51 A laminar velocity profile on a hollow cylinder in Mach 7 flow measured by Webber *et al.* [101] using the tangent method and compared to laminar CFD. Adapted with author permission from [101] © Nicholas Webber, Sophia Edwards, and Mark Gragston.

D. Broad Usage Barriers

Finally, a major challenge for MTV is associated with its ability to be integrated into standard usage for hypersonic ground testing at both the university scale and at research centers. Unlike PIV, which requires minimal technical knowledge of laser hardware and photophysical processes to obtain reasonable measurements, MTV is very specialized from a technical knowledge perspective. This is also true regarding data processing for MTV measurements, as discussed previously. Therefore, effort is needed to make MTV techniques more accessible to users with limited knowledge of laser systems and laser hardware (like optical parametric oscillators or "OPOs") and improving the data processing workflow (perhaps with robust, standardized software packages or with machine learning approaches that can process a wide array of data).

Also under this category is the barrier introduced by cost. Compared to PIV, MTV has significantly higher potential costs, which may include specialized laser systems (*e.g.*, burst-mode lasers with OPOs or femtosecond lasers), intensified cameras, and more. This cost must also be viewed in context of the cost of building, maintaining, and operating high-speed wind tunnels. Hence, it is generally expensive for users to acquire MTV measurement hardware while also running high-speed facilities, which has likely slowed the development and implementation of the technique. For investigators looking to start making use of MTV, lasers such a dual-head Nd:YAGs (that output a frequency-doubled 532 nm beam) that are commonly used for PIV can be frequency-quadrupled with a single additional BBO crystal and used for acetone MTV. Another emerging possibility is a frequency-quintupled laser via two additional BBO crystals for nitric oxide based MTV.

VII. Summary and Conclusions

Molecular tagging velocimetry has developed tremendously over the recent decades due to advances in both laser and imaging technology, but also because of continued research in developing new approaches. These advances have directly translated to improved velocimetry capabilities that support ground testing efforts related to high-speed and hypersonic flows and validation of computational tools.

Acknowledgments

The authors wish to acknowledge the many researchers who have worked to develop MTV methods and apply them for understanding various fluid dynamic phenomena. We highly encourage readers to use this document as a resource to help locate those works and cite them for proper recognition when appropriate.

Trade names and trademarks are used in this report for identification only. Their usage does not constitute an official endorsement, either expressed or implied, by the National Aeronautics and Space Administration.

References

[1] Brooks, J., Gupta, A., Smith, M., and Marineau, E., "Particle image velocimetry measurements of Mach 3 turbulent boundary layers at low Reynolds numbers," *Experiments in Fluids*, Vol. 59, No. 5, 2018, p. 83. https://doi.org/10.1007/s00348-018-2536-x.

[2] Brooks, J., "Development and Application of Mach 10 PIV in a Large Scale Wind Tunnel," Ph.D. thesis, University of Maryland, College Park, 2018. https://doi.org/10.13016/M23F4KR6C.

[3] Scarano, F., "Overview of PIV in Supersonic Flows," *Particle Image Velocimetry: New Developments and Recent Applications*, Springer Berlin Heidelberg, Berlin, Heidelberg, 2008, pp. 445–463. https://doi.org/10.1007/978-3-540-73528-1{_}24.

[4] Aultman, M. T., Disotell, K., and Duan, L., "The effect of particle lag on statistics of hypersonic turbulent boundary layers subject to pressure gradients," *AIAA SCITECH 2022 Forum*, 2022, p. 1062. https://doi.org/10.2514/6.2022-1062.

[5] Popovich, A., and Hummel, R., "A new method for non-disturbing turbulent flow measurements very close to a wall," *Chemical Engineering Science*, Vol. 22, No. 1, 1967, pp. 21–25. https://doi.org/10.1016/0009-2509(67)80100-3.

[6] Epstein, A. H., "Quantitative Density Visualization in a Transonic Compressor Rotor," *Journal of Engineering for Power*, Vol. 99, No. 3, 1977, pp. 460–475. https://doi.org/10.1115/1.3446531.

[7] Hiller, B., Booman, R. A., Hassa, C., and Hanson, R. K., "Velocity visualization in gas flows using laser-induced phosphorescence of biacetyl," *Review of Scientific Instruments*, Vol. 55, No. 12, 1984, pp. 1964–1967. https://doi.org/10.1063/1.1137687.

[8] Miles, R., Cohen, C., Connors, J., Howard, P., Huang, S., Markovitz, E., and Russell, G., "Velocity measurements by vibrational tagging and fluorescent probing of oxygen," *Optics Letters*, Vol. 12, No. 11, 1987, p. 861. https://doi.org/10.1364/OL.12.000861.

[9] Miles, R. B., Connors, J. J., Markovitz, E. C., Howard, P. J., and Roth, G. J., "Instantaneous profiles and turbulence statistics of supersonic free shear layers by Raman excitation plus laser-induced electronic fluorescence (Relief) velocity tagging of oxygen," *Experiments in Fluids*, Vol. 8, No. 1-2, 1989, pp. 17–24. https://doi.org/10.1007/BF00203060.

[10] Balla, R. J., "Iodine Tagging Velocimetry in a Mach 10 Wake," *AIAA Journal*, Vol. 51, No. 7, 2013, pp. 1783–1786. https://doi.org/10.2514/1.J052416.

[11] Miles, R. B., Grinstead, J., Kohl, R. H., and Diskin, G., "The RELIEF flow tagging technique and its application in engine testing facilities and for helium-air mixing studies," *Measurement Science and Technology*, Vol. 11, No. 9, 2000, p. 1272. https://doi.org/10.1088/0957-0233/11/9/304.

[12] Ribarov, L. A., Wehrmeyer, J. A., Batliwala, F., Pitz, R. W., and DeBarber, P. A., "Ozone Tagging Velocimetry Using Narrowband Excimer Lasers," *AIAA Journal*, Vol. 37, No. 6, 1999, pp. 708–714. https://doi.org/10.2514/2.799.

[13] Littleton, B., Bishop, A., McIntyre, T., Rubinsztein-Dunlop, H., and Barker, P., "Flow tagging velocimetry in a superorbital expansion tube," *Shock Waves*, Vol. 10, 2000, pp. 225–228. https://doi.org/10.1007/s001930050010.

[14] Dam, N., Klein-Douwel, R. J. H., Sijtsema, N. M., and ter Meulen, J. J., "Nitric oxide flow tagging in unseeded air," *Optics Letters*, Vol. 26, No. 1, 2001, p. 36. https://doi.org/10.1364/OL.26.000036.

[15] Zhang, S., Yu, X., Yan, H., Huang, H., and Liu, H., "Molecular tagging velocimetry of NH fluorescence in a high-enthalpy rarefied gas flow," *Applied Physics B*, Vol. 123, No. 4, 2017, p. 122. https://doi.org/10.1007/s00340-017-6703-1.

[16] Barker, P., Thomas, A., Rubinsztein-Dunlop, H., and Ljungberg, P., "Velocity measurements by flow tagging employing laser enhanced ionisation and laser induced fluorescence," *Spectrochimica Acta Part B: Atomic Spectroscopy*, Vol. 50, No. 11, 1995, pp. 1301–1310. https://doi.org/10.1016/0584-8547(95)01353-X.

[17] Krüger, S., and Grünefeld, G., "Applied Physics B Lasers and Optics Stereoscopic flow-tagging velocimetry," *Appl. Phys. B*, Vol. 69, 1999, pp. 509–512. https://doi.org/10.1007/s003409900146.

[18] Mills, J. L., Sukenik, C. I., and Balla, R. J., "Hypersonic Wake Diagnostics Using Laser Induced Fluorescence Techniques," *Proceedings of 42nd AIAA Plasmadynamics and Lasers Conference*, AIAA 2011-3459, Honolulu, Hawaii, 2011. https://doi.org/10.2514/6.2011-3459.

[19] Balla, R. J., and Everhart, J. L., "Rayleigh Scattering Density Measurements, Cluster Theory, and Nucleation Calculations at Mach 10," *AIAA Journal*, Vol. 50, No. 3, 2012, pp. 698–707. https://doi.org/10.2514/1.J051334.

[20] Parziale, N., Smith, M., and Marineau, E., "Krypton tagging velocimetry of an underexpanded jet," *Applied optics*, Vol. 54, No. 16, 2015, pp. 5094–5101. https://doi.org/10.1364/AO.54.005094.

[21] Parziale, N. J., Smith, M., and Marineau, E. C., "Krypton tagging velocimetry for use in high-speed ground-test facilities," *53rd AIAA Aerospace Sciences Meeting*, 2015, p. 1484. https://doi.org/10.2514/6.2015-1484.

[22] Mustafa, M., and Parziale, N., "Simplified read schemes for krypton tagging velocimetry in N2 and air," *Optics Letters*, Vol. 43, No. 12, 2018, pp. 2909–2912. https://doi.org/10.1364/OL.43.002909.

[23] Shekhtman, D., Parziale, N. J., and Mustafa, M. A., "Excitation line optimization for krypton tagging velocimetry and planar laser-induced fluorescence in 200-220 nm range," *AIAA Scitech 2021 Forum*, 2021, p. 1300. https://doi.org/10.2514/6.2021-1300.

[24] Shekhtman, D., "Multiphoton Processes for High-Speed Optical Diagnostics," Ph.D. thesis, Stevens Institute of Technology, 2022.

[25] Shekhtman, D., Mustafa, M. A., and Parziale, N. J., "Two-photon cross-section calculations for krypton in the 190-220 nm range," *Applied Optics*, Vol. 59, No. 34, 2020, pp. 10826–10837. https://doi.org/10.1364/AO.410806.

[26] Kramida, A., Ralchenko, Y., Reader, J., et al., "NIST atomic spectra database," *NIST standard reference database*, Vol. 78, 2018, pp. 21–22.

[27] Michael, J. B., Edwards, M. R., Dogariu, A., and Miles, R. B., "Femtosecond laser electronic excitation tagging for quantitative velocity imaging in air," *Applied optics*, Vol. 50, No. 26, 2011, pp. 5158–5162. https://doi.org/10.1364/AO.50.005158.

[28] Danehy, P. M., Burns, R. A., Reese, D. T., Retter, J. E., and Kearney, S. P., "FLEET velocimetry for aerodynamics," *Annual Review of Fluid Mechanics*, Vol. 54, No. 1, 2022, pp. 525–553. https://doi.org/annurev-fluid-032321-025544.

[29] Burns, R., Danehy, P. M., Jones, S. B., Halls, B. R., and Jiang, N., "Application of FLEET velocimetry in the NASA Langley 0.3-meter transonic cryogenic tunnel," *31st AIAA Aerodynamic Measurement Technology and Ground Testing Conference*, 2015, p. 2566. https://doi.org/10.2514/6.2015-2566.

[30] Zhang, Y., "The development and characterization of femtosecond laser velocimetry methods," Ph.D. thesis, Princeton University, 2018. URL http://arks.princeton.edu/ark:/88435/dsp01hd76s2776.

[31] Li, B., Zhang, D., Liu, J., Tian, Y., Gao, Q., and Li, Z., "A review of femtosecond laser-induced emission techniques for combustion and flow field diagnostics," *Applied Sciences*, Vol. 9, No. 9, 2019, p. 1906. https://doi.org/10.3390/app9091906.

[32] Peters, C. J., "Considerations for femtosecond laser electronic excitation tagging in high-speed flows," Ph.D. thesis, Princeton University, 2019. URL http://arks.princeton.edu/ark:/88435/dsp01fn107187q.

[33] Michael, J., Edwards, M., Dogariu, A., and Miles, R., "Velocimetry by femtosecond laser electronic excitation tagging (FLEET) of air and nitrogen," *50th AIAA aerospace sciences meeting including the new horizons forum and aerospace exposition*, 2012, p. 1053.

[34] Limbach, C. M., "Characterization of nanosecond, femtosecond and dual pulse laser energy deposition in air for flow control and diagnostic applications," Ph.D. thesis, Princeton University, 2015.

[35] Limbach, C. M., and Miles, R. B., "Rayleigh scattering measurements of heating and gas perturbations accompanying femtosecond laser tagging," *AIAA Journal*, Vol. 55, No. 1, 2017, pp. 112–120. https://doi.org/10.2514/1.J054772.

[36] Zhang, Y., Beresh, S. J., Casper, K. M., Richardson, D. R., Soehnel, M., and Spillers, R., "Tailoring FLEET for cold hypersonic flows," *AIAA Scitech 2020 Forum*, 2020, p. 1020. https://doi.org/10.2514/6.2020-1020.

[37] Peters, C. J., Burns, R. A., Miles, R. B., and Danehy, P. M., "Effect of low temperatures and pressures on signal, lifetime, accuracy and precision of femtosecond laser tagging velocimetry," *Measurement Science and Technology*, Vol. 32, No. 3, 2020, p. 035202. https://doi.org/10.1088/1361-6501/abc577.

[38] Wang, W., Choudhary, R., and Limbach, C., "Characterizing Femtosecond Laser Tagging Performance With A 1030 Nm Yb:KGW Laser And Application To Continuous 50 KHz Velocimetry," *21st International Symposium on Application of Laser and Imaging Techniques to Fluid Mechanics*, 2024. https://doi.org/10.55037/lxlaser.21st.227.

[39] Jiang, N., Mance, J. G., Slipchenko, M. N., Felver, J. J., Stauffer, H. U., Yi, T., Danehy, P. M., and Roy, S., "Seedless velocimetry at 100 kHz with picosecond-laser electronic-excitation tagging," *Optics letters*, Vol. 42, No. 2, 2017, pp. 239–242. https://doi.org/10.1364/OL.42.000239.

[40] Jiang, N., Halls, B. R., Stauffer, H. U., Danehy, P. M., Gord, J. R., and Roy, S., "Selective two-photon absorptive resonance femtosecond-laser electronic-excitation tagging velocimetry," *Optics Letters*, Vol. 41, No. 10, 2016, pp. 2225–2228. https://doi.org/10.1364/OL.41.002225.

[41] Zhang, Y., Danehy, P. M., and Miles, R. B., "Femtosecond laser tagging in R134a with small quantities of air," *AIAA Journal*, Vol. 57, No. 5, 2019, pp. 1793–1800. https://doi.org/10.2514/1.J057156.

[42] Gao, Q., Zhang, D., Li, X., Li, B., and Li, Z., "Femtosecond-laser electronic-excitation tagging velocimetry using a 267 nm laser," *Sensors and Actuators A: Physical*, Vol. 287, 2019, pp. 138–142. https://doi.org/10.1016/j.sna.2019.01.004.

[43] Pitz, R. W., and Danehy, P. M., "Molecular Tagging Velocimetry in Gases," *Optical Diagnostics for Reacting and Non-Reacting Flows: Theory and Practice*, AIAA, Reston, VA, 2023, Chap. 10, pp. 539–588. https://doi.org/10.2514/5.9781624106330.0539.0588.

[44] Pimentel, C. A. R., and Hetem Jr., A., "Computation of air chemical equilibrium composition until 30000K - Part I," *Journal of Aerospace Technology and Management*, Vol. 3, No. 2, 2011, pp. 111–126. https://doi.org/10.5028/jatm.2011.03021011.

[45] Lynch, K. P., Grasser, T., Spillers, R., Downing, C., Daniel, K. A., Jans, E. R., Kearney, S., Morreale, B. J., Wagnild, R., and Wagner, J. L., "Design and characterization of the Sandia free-piston reflected shock tunnel," *Shock Waves*, Vol. 33, No. 4, 2023, pp. 299–314. https://doi.org/10.1007/s00193-023-01127-4.

[46] Girard, J. J., Finch, P. M., Strand, C. L., Hanson, R. K., Yu, W. M., Austin, J. M., and Hornung, H. G., "Measurements of Reflected Shock Tunnel Freestream Nitric Oxide Temperatures and Partial Pressure," *AIAA Journal*, Vol. 59, No. 12, 2021, pp. 5266–5275. https://doi.org/10.2514/1.J060596.

[47] Leonov, B. S., Dean, T. S., Limbach, C. M., Bowersox, R. D., and Miles, R. B., "High-speed planar laser-induced fluorescence investigation of nitric oxide generated by hypersonic Mach reflections for computational fluid dynamics validation," *Physics of Fluids*, Vol. 35, No. 6, 2023. https://doi.org/10.1063/5.0150273.

[48] Jiang, N., Webster, M., Lempert, W. R., Miller, J. D., Meyer, T. R., Ivey, C. B., and Danehy, P. M., "MHz-rate nitric oxide planar laser-induced fluorescence imaging in a Mach 10 hypersonic wind tunnel," *Applied Optics*, Vol. 50, No. 4, 2011. https://doi.org/10.1364/AO.50.000A20.

[49] Bolderman, T., Maes, N., and Dam, N., "Nitric oxide laser-induced fluorescence using the fifth harmonic of a broad-band Nd:YAG laser," *Applied Physics B*, Vol. 130, No. 8, 2024, p. 148. https://doi.org/10.1007/s00340-024-08292-z.

[50] Leonov, B. S., Grunbok, C. J., and Miles, R. B., "Megahertz-rate NO planar laser-induced fluorescence of reacting flows using tunable 5th harmonic Nd:YAG with A-X and B-X excitation," *Optics Express*, Vol. 33, No. 6, 2025, p. 12336. https://doi.org/10.1364/OE.553172.

[51] Luque, J., and Crosley, D. R., "LIFBASE: Database and spectral simulation program (version 1.5)," *SRI international report MP*, Vol. 99, No. 009, 1999.

[52] Rodrigues, N. S., Jiang, N., Hsu, P., Roy, S., and Danehy, P. M., "Multiline molecular tagging velocimetry of nitric oxide at 100 kHz using an injection-seeded burst-mode OPO," *Applied Optics*, Vol. 63, No. 5, 2024, pp. 1247–1257. https://doi.org/10.1364/AO.507732.

[53] Buen, Z., Broslawski, C., Smotzer, M., Kuszynski, J., North, S. W., and Bowersox, R. D., "Towards vibrationally excited nitric oxide monitoring (Venom) in a laminar, hypersonic boundary layer," *AIAA 2020-1275. AIAA Scitech 2020 Forum*, 2020. https://doi.org/10.2514/6.2020-1275.

[54] Danehy, P. M., O'Byrne, S., Houwing, A. F. P., Fox, J. S., and Smith, D. R., "Flow-tagging velocimetry for hypersonic flows using fluorescence of nitric oxide," *AIAA Journal*, Vol. 41, No. 2, 2003, pp. 263–271. https://doi.org/10.2514/2.1939.

[55] Bessler, W. G., Schulz, C., Lee, T., Jeffries, J. B., and Hanson, R. K., "Strategies for laser-induced fluorescence detection of nitric oxide in high-pressure flames III Comparison of A–X excitation schemes," *Applied Optics*, Vol. 42, No. 24, 2003, p. 4922. https://doi.org/10.1364/ao.42.004922.

[56] Piper, L. G., and Cowles, L. M., "Einstein coefficients and transition moment variation for the NO(A 2+-X 2Π) transition," *The Journal of Chemical Physics*, Vol. 85, No. 5, 1986, pp. 2419–2422. https://doi.org/10.1063/1.451098.

[57] Paul, P. H., Gray, J. A., Durant, J. L., and Thoman, J. W., "Collisional quenching corrections for laser-induced fluorescence measurements of NO A2Sigma(+)," *AIAA Journal*, Vol. 32, No. 8, 1994, pp. 1670–1675. https://doi.org/10.2514/3.12158.

[58] Inman, J. A., Bathel, B. F., Johansen, C. T., Danehy, P. M., Jones, S. B., Gragg, J. G., and Splinter, S. C., "Nitric-Oxide Planar Laser-Induced Fluorescence Measurements in the Hypersonic Materials Environmental Test System," *AIAA Journal*, Vol. 51, No. 10, 2013, pp. 2365–2379. https://doi.org/10.2514/1.J052246.

[59] Rodrigues, N. S., Tyrrell, O. K., Rieken, E., Hollis, B. R., and Danehy, P. M., "FLEET and PLIF velocimetry within a Mach 10 hypersonic air flow," *AIAA SCITECH 2024 Forum*, 2024, p. 2323. https://doi.org/10.2514/6.2024-2323.

[60] Jans, E. R., Lynch, K. P., Daniel, K. A., and Kearney, S. P., "Nitric oxide molecular tagging velocimetry of a free-flight model in a reflected shock tunnel," *Optics Letters*, Vol. 50, No. 6, 2025, pp. 1839–1842. https://doi.org/10.1364/OL.557444.

[61] Jiang, N., Lempert, W. R., Switzer, G. L., Meyer, T. R., and Gord, J. R., "Narrow-linewidth megahertz-repetition-rate optical parametric oscillator for high-speed flow and combustion diagnostics," *Applied Optics*, Vol. 47, No. 1, 2008, pp. 64–71. https://doi.org/10.1364/AO.47.000064.

[62] Leonov, B. S., Limbach, C. M., Kochan, J. S., and Miles, R. B., "Effects of Cavity Length and Pump Pulse Duration on Burst-mode Optical Parametric Oscillator Conversion Efficiency," *AIAA 2024-2033. AIAA SCITECH 2024 Forum. January*, 2024. https://doi.org/10.2514/6.2024-2033.

[63] Webb, A. M., Crabtree, C. Q., Athmanathan, V., Meyer, T. R., Kearney, S. P., and Slipchenko, M. N., "High-efficiency narrow-bandwidth KTP optical parametric oscillator for kHz–MHz planar laser-induced fluorescence," *Optics Letters*, Vol. 49, No. 6, 2024, p. 1473. https://doi.org/10.1364/OL.510334.

[64] Orlemann, C., Schulz, C., and Wolfrum, J., "NO-flow tagging by photodissociation of NO2. A new approach for measuring small-scale flow structures," *Chemical Physics Letters*, Vol. 307, No. 1-2, 1999, pp. 15–20. https://doi.org/10.1016/S0009-2614(99)00512-6.

[65] Hsu, A. G., Srinivasan, R., Bowersox, R. D. W., and North, S. W., "Two-component molecular tagging velocimetry utilizing NO fluorescence lifetime and NO_2 photodissociation techniques in an underexpanded jet flowfield," *Applied Optics*, Vol. 48, No. 22, 2009, p. 4414. https://doi.org/10.1364/AO.48.004414.

[66] Jiang, N., Nishihara, M., and Lempert, W. R., "Quantitative NO2 molecular tagging velocimetry at 500 kHz frame rate," *Applied Physics Letters*, Vol. 97, No. 22, 2010. https://doi.org/10.1063/1.3522654.

[67] Sánchez-González, R., Srinivasan, R., Bowersox, R. D. W., and North, S. W., "Simultaneous velocity and temperature measurements in gaseous flow fields using the VENOM technique," *Optics Letters*, Vol. 36, No. 2, 2011, p. 196. https://doi.org/10.1364/ol.36.000196.

[68] Sánchez-González, R., Bowersox, R. D. W., and North, S. W., "Vibrationally excited NO tagging by NO(Aˆ2Σˆ+) fluorescence and quenching for simultaneous velocimetry and thermometry in gaseous flows," *Optics Letters*, Vol. 39, No. 9, 2014, p. 2771. https://doi.org/10.1364/ol.39.002771.

[69] Leonov, B. S., Moran, A. N., North, S. W., and Miles, R. B., "Burst-mode velocimetry of hypersonic flow by nitric oxide ionization induced flow tagging and imaging," *Optics Letters*, Vol. 49, No. 3, 2024, pp. 426–429. https://doi.org/10.1364/OL.503786.

[70] Karagulian, F., and Rossi, M. J., "The heterogeneous chemical kinetics of NO3 on atmospheric mineral dust surrogates," *Physical Chemistry Chemical Physics*, Vol. 7, No. 17, 2005, p. 3150. https://doi.org/10.1039/b506750m.

[71] Boivin, R. F., and Scime, E. E., "Control of nitrogen species in helicon plasmas," *Plasma Sources Science and Technology*, Vol. 14, No. 2, 2005, pp. 283–292. https://doi.org/10.1088/0963-0252/14/2/009.

[72] Jiang, N., Hsu, P. S., Roy, S., Wang, J., Hu, H., Rodrigues, N., and Danehy, P. M., "Long-lived nitric oxide molecular tagging velocimetry with 1+ 1 REMPI," *Optics Letters*, Vol. 49, No. 5, 2024, pp. 1297–1300. https://doi.org/10.1364/OL.514912.

[73] Leonov, B. S., Jiang, N., Siddiqui, F., Roy, S., and Miles, R. B., "Seedless velocimetry of high-enthalpy hypersonic boundary layers by nitric oxide ionization induced flow tagging and imaging at 100 kHz," *Optics Letters*, Vol. 50, No. 1, 2024, pp. 205–208. https://doi.org/10.1364/OL.537837.

[74] Leonov, B., Moran, A., White, J., Best, T., Dogariu, A., Tichenor, N., North, S., and Miles, R., "Nitric-oxide ionization induced Flow Tagging and Imaging for Near-surface Velocimetry in Hypersonic Boundary Layers," *AIAA 2024-4588. AIAA AVIATION 2024 Forum. July*, 2024. https://doi.org/10.2514/6.2024-4588.

[75] Leonov, B. S., and Miles, R. B., "Single-shot Nitric-oxide ionization induced Flow Tagging and Imaging in a cold hypersonic flow using 5th harmonic Nd:YAG laser at 200 kHz," *Optics Express*, Vol. 33, No. 17, 2025, p. 35737. https://doi.org/10.1364/OE.567227.

[76] Koch, J., and Hanson, R., *Ketone photophysics for quantitative PLIF imaging*, AIAA, 2001. https://doi.org/10.2514/6.2001-413.

[77] Damon, G. H., and Daniels, F., "The Photolysis of Gaseous Acetone and the Influence of Water1," *Journal of the American Chemical Society*, Vol. 55, No. 6, 1933, pp. 2363–2375. https://doi.org/10.1021/ja01333a022.

[78] Luckey, G. W., and Noyes, J., W. Albert, "The Fluorescence of Acetone Vapor," *The Journal of Chemical Physics*, Vol. 19, No. 2, 1951, pp. 227–231. https://doi.org/10.1063/1.1748166.

[79] Lozano, A., Yip, B., and Hanson, R. K., "Acetone: a tracer for concentration measurements in gaseous flows by planar laser-induced fluorescence," *Experiments in Fluids*, Vol. 13, 1992, pp. 369–376. https://doi.org/10.1007/bf00223244.

[80] Ambrose, D., Sprake, C., and Townsend, R., "Thermodynamic properties of organic oxygen compounds XXXIII. The vapour pressure of acetone," *The Journal of Chemical Thermodynamics*, Vol. 6, No. 7, 1974, pp. 693–700. https://doi.org/10.1016/0021-9614(74)90119-0.

[81] Brunzendorf, J., Höltkemeier-Horstmann, J., and and, D. M., "266 nm Laser-Induced Fluorescence Reference Spectra of Ketones and Aromatic Compounds," *Combustion Science and Technology*, Vol. 196, No. 13, 2024, pp. 2128–2137. https://doi.org/10.1080/00102202.2024.2378469.

[82] Tran, T., Kochar, Y., and Seitzman, J., *Measurement of Acetone Fluorescence and Phosphorescence at High Presssures and Temperatures*, AIAA, 2006. https://doi.org/10.2514/6.2006-831.

[83] Thurber, M. C., Grisch, F., Kirby, B. J., Votsmeier, M., and Hanson, R. K., "Measurements and modeling of acetone laser-induced fluorescence with implications for temperature-imaging diagnostics," *Appl. Opt.*, Vol. 37, No. 21, 1998, pp. 4963–4978. https://doi.org/10.1364/AO.37.004963.

[84] Lempert, W. R., Jiang, N., Sethuram, S., and Samimy, M., "Molecular Tagging Velocimetry Measurements in Supersonic Microjets," *AIAA Journal*, Vol. 40, No. 6, 2002, pp. 1065–1070. https://doi.org/10.2514/2.1789.

[85] Gragston, M., and Smith, C. D., "10 kHz molecular tagging velocimetry in a Mach 4 air flow with acetone vapor seeding," *Experiments in Fluids*, Vol. 63, No. 5, 2022, p. 85. https://doi.org/10.1007/s00348-022-03438-1.

[86] Andrade, A., Hoffman, E. N. A., LaLonde, E. J., and Combs, C. S., "Velocity measurements in a hypersonic flow using acetone molecular tagging velocimetry," *Optics Express*, Vol. 30, No. 23, 2022, pp. 42199–42213. https://doi.org/10.1364/OE.474841.

[87] Alfonso-Olmos, E., Keenoy, T., and Shekhtman, D., "Parametric study of acetone excitation for use in flow diagnostics," *Opt. Continuum*, Vol. 4, No. 3, 2025, pp. 675–686. https://doi.org/10.1364/OPTCON.555334.

[88] Garrard, G. D., "Hypersonic Test Capabilities at AEDC's Aerodynamic and Propulsion Test Unit," *53rd AIAA Aerospace Sciences Meeting*, 2015, p. 1784. https://doi.org/10.2514/6.2015-1784.

[89] Hodge, J., and Harvin, S., "Test capabilities and recent experiences in the NASA Langley 8-foot high temperature tunnel," *21st Aerodynamic Measurement Technology and Ground Testing Conference*, 2000, p. 2646. https://doi.org/10.2514/6.2000-2646.

[90] Lahr, M. D., Pitz, R. W., Douglas, Z. W., and Carter, C. D., "Hydroxyl-tagging-velocimetry measurements of a supersonic flow over a cavity," *Journal of Propulsion and Power*, Vol. 26, No. 4, 2010, pp. 790–797. https://doi.org/10.2514/1.47264.

[91] Tareq, M. M., "Near-Wall Measurements with High-Spatial Resolution Hydroxyl Tagging Velocimetry," Ph.D. thesis, The George Washington University, 2025.

[92] Pitz, R. W., Wehrmeyer, J. A., Ribarov, L. A., Oguss, D. A., Batliwala, F., DeBarber, P. A., Deusch, S., and Dimotakis, P. E., "Unseeded molecular flow tagging in cold and hot flows using ozone andhydroxyl tagging velocimetry," *Measurement Science and technology*, Vol. 11, No. 9, 2000, p. 1259. https://doi.org/10.1088/0957-0233/11/9/303.

[93] Pitz, R., *Hydroxyl Tagging Velocimetry*, AIAA, 2008. https://doi.org/10.2514/6.2008-3758.

[94] Ribarov, L., Wehrmeyer, J., Hu, S., and Pitz, R., "Multiline hydroxyl tagging velocimetry measurements in reacting and nonreacting experimental flows," *Experiments in Fluids*, Vol. 37, 2004, pp. 65–74. https://doi.org/10.1007/s00348-004-0785-3.

[95] Ribarov, L. A., Hu, S., Wehrmeyer, J. A., and Pitz, R. W., "Hydroxyl tagging velocimetry method optimization: signal intensity and spectroscopy," *Applied optics*, Vol. 44, No. 31, 2005, pp. 6616–6626. https://doi.org/10.1364/AO.44.006616.

[96] Ribarov, L., Wehrmeyer, J., Pitz, R., and Yetter, R. A., "Hydroxyl tagging velocimetry (HTV) in experimental air flows," *Applied Physics B*, Vol. 74, 2002, pp. 175–183. https://doi.org/10.1007/s003400100777.

[97] Pitz, R. W., Lahr, M. D., Douglas, Z. W., Wehrmeyer, J. A., Hu, S., Carter, C. D., Hsu, K.-Y., Lum, C., and Koochesfahani, M. M., "Hydroxyl tagging velocimetry in a supersonic flow over a cavity," *Applied optics*, Vol. 44, No. 31, 2005, pp. 6692–6700. https://doi.org/10.1364/AO.44.006692.

[98] Fisher, J. M., Brown, A. D., Lauriola, D. K., Slipchenko, M. N., and Meyer, T. R., "Femtosecond laser activation and sensing of hydroxyl for velocimetry in reacting flows," *Applied Optics*, Vol. 59, No. 34, 2020, pp. 10853–10861. https://doi.org/10.1364/AO.404788.

[99] Pehrson, J. C., Leonov, B. S., Melone, K., Lakebrink, M. T., Bowersox, R., Miles, R. B., and Limbach, C. M., "Hypersonic FLEET velocimetry and uncertainty characterization in a tripped boundary layer," *Measurement Science and Technology*, Vol. 35, No. 1, 2023, p. 015206. https://doi.org/10.1088/1361-6501/acf592.

[100] Zahradka, D., Parziale, N., Smith, M., and Marineau, E., "Krypton tagging velocimetry in a turbulent Mach 2.7 boundary layer," *Experiments in Fluids*, Vol. 57, 2016, pp. 1–14. https://doi.org/10.1007/s00348-016-2148-2.

[101] Webber, N., Edwards, S., and Gragston, M., "Axisymmetric Hypersonic Boundary-Layer Profile Measurements Using Tangentially Oriented FLEET Velocimetry," *AIAA Journal*, 2025, pp. 1–8. https://doi.org/10.2514/1.J065154.

[102] Webber, N., Edwards, S., and Gragston, M., "FLEET Velocimetry Measurements of Boundary Layer Transition on a Hollow Cylinder in Mach 7 Flow," *AIAA SCITECH 2026 Forum*, American Institute of Aeronautics and Astronautics, 2026.

[103] Dogariu, L. E., Dogariu, A., Miles, R. B., Smith, M. S., and Marineau, E. C., "Femtosecond laser electronic excitation tagging velocimetry in a large-scale hypersonic facility," *AIAA journal*, Vol. 57, No. 11, 2019, pp. 4725–4737. https://doi.org/10.2514/1.J057759.

[104] Gevelber, T., Schmidt, B., Mustafa, M., Shekhtman, D., and Parziale, N., "Determining velocity from tagging velocimetry images using optical flow," *Experiments in Fluids*, Vol. 63, No. 6, 2022, p. 104. https://doi.org/10.1007/s00348-022-03448-z.

[105] Mustafa, M. A., Parziale, N. J., Marineau, E. C., and Smith, M. S., "Two-dimensional krypton tagging velocimetry (KTV-2D) investigation of shock-wave/turbulent boundary-layer interaction," *2018 AIAA aerospace sciences meeting*, 2018, p. 1771. https://doi.org/10.2514/6.2018-1771.

[106] Gragston, M., "Computational Analysis of Motion Blur Correction for Molecular Tagging Velocimetry," *AIAA Journal*, 2025, pp. 1–11. https://doi.org/10.2514/1.J065232.

[107] Bathel, B. F., "Application of molecular tagging velocimetry to study laminar flow and laminar-to-turbulent transition in hypersonic boundary layers," Ph.D. thesis, Doctoral Dissertation,(University of Virginia, 2013), 2013.

[108] Bathel, B. F., Danehy, P. M., Inman, J. A., Jones, S. B., Ivey, C. B., and Goyne, C. P., "Velocity Profile Measurements in Hypersonic Flows Using Sequentially Imaged Fluorescence-Based Molecular Tagging," *AIAA Journal*, Vol. 49, No. 9, 2011, pp. 1883–1896. https://doi.org/10.2514/1.J050722.

[109] White, F. M., and Majdalani, J., *Viscous fluid flow*, Vol. 3, McGraw-Hill New York, 2006.

[110] Wei, T., Schmidt, R., and McMurtry, P., "Comment on the Clauser chart method for determining the friction velocity," *Experiments in fluids*, Vol. 38, 2005, pp. 695–699. https://doi.org/10.1007/s00348-005-0934-3.

[111] Sun, C.-C., and Childs, M. E., "A modified wall wake velocity profile for turbulent compressible boundary layers." *Journal of Aircraft*, Vol. 10, No. 6, 1973, pp. 381–383. https://doi.org/10.2514/3.44376.

[112] Smith, C. D., Lester, L. E., Siddiqui, F., and Gragston, M., "10 kHz acetone molecular tagging velocimetry in a Mach 4 Ludwieg tube," *AIAA SCITECH 2023 Forum*, 2023, p. 0630. https://doi.org/10.2514/6.2023-0630.

[113] Smits, A. J., and Dussauge, J.-P., *Turbulent shear layers in supersonic flow*, Springer Science & Business Media, 2006.

[114] Spalding, D. B., et al., "A single formula for the law of the wall," *Journal of Applied Mechanics*, Vol. 28, No. 3, 1961, pp. 455–458. https://doi.org/10.1115/1.3641728.

[115] Coles, D., "The law of the wake in the turbulent boundary layer," *Journal of Fluid Mechanics*, Vol. 1, No. 2, 1956, pp. 191–226. https://doi.org/10.1017/S0022112056000135.

[116] Kim, J., Simon, T., and Russ, S., "Free-stream turbulence and concave curvature effects on heated, transitional boundary layers," Tech. Rep. 19910018174, National Aeronautics and Space Administration, 1992.

[117] Wang, T., Keller, F. J., and Zhou, D., "Flow and thermal structures in a transitional boundary layer," *Experimental thermal and fluid science*, Vol. 12, No. 3, 1996, pp. 352–363. https://doi.org/10.1016/0894-1777(95)00126-3.

[118] Mustafa, M. A., Parziale, N. J., Smith, M. S., and Marineau, E. C., "Nonintrusive Freestream Velocity Measurement in a Large-Scale Hypersonic Wind Tunnel," *AIAA Journal*, Vol. 55, No. 10, 2017, pp. 3611–3616. https://doi.org/10.2514/1.J056177.

[119] Gopal, V., Palmquist, D., Maddalena, L., Dogariu, L. E., and Dogariu, A., "FLEET velocimetry measurements in the ONR-UTA arc-jet wind tunnel," *Experiments in Fluids*, Vol. 62, 2021, pp. 1–17. https://doi.org/10.1007/s00348-021-03306-4.

[120] Shekhtman, D., Mustafa, M. A., Parziale, N. J., Yu, W. M., and Austin, J. M., "Krypton Tagging Velocimetry (KTV) Investigation in the Caltech T5 Reflected-Shock Tunnel," *Proceedings of AIAA SciTech 2021*, AIAA-2021-1302, Virtual Event, 2021. https://doi.org/10.2514/6.2021-1302.

[121] Shekhtman, D., Yu, W., Mustafa, M., Parziale, N., and Austin, J., "Freestream velocity-profile measurement in a large-scale, high-enthalpy reflected-shock tunnel," *Experiments in Fluids*, Vol. 62, No. 5, 2021, p. 118. https://doi.org/10.1007/s00348-021-03207-6.

[122] Thurow, B., Jiang, N., and Lempert, W., "Review of ultra-high repetition rate laser diagnostics for fluid dynamic measurements," *Measurement Science and Technology*, Vol. 24, No. 1, 2013. https://doi.org/10.1088/0957-0233/24/1/012002.

[123] Slipchenko, M. N., Meyer, T. R., and Roy, S., "Advances in burst-mode laser diagnostics for reacting and nonreacting flows," *Proceedings of the Combustion Institute*, Vol. 38, No. 1, 2021, pp. 1533–1560. https://doi.org/10.1016/j.proci.2020.07.024.

[124] Jiang, N., Hsu, P. S., Grib, S. W., Slipchenko, M., Shekhtman, D., Parziale, N. J., Smith, M. S., Spicer, A. J., and Roy, S., "Mach 18 flow velocimetry with 100-kHz KTV and PLEET in AEDC Tunnel 9," *Applied Optics*, Vol. 62, No. 6, 2023, pp. A25–A30. https://doi.org/10.1364/AO.477203.

[125] Mustafa, M. A., Shekhtman, D., and Parziale, N. J., "Single-laser krypton tagging velocimetry investigation of supersonic air and N 2 boundary-layer flows over a hollow cylinder in a shock tube," *Physical Review Applied*, Vol. 11, No. 6, 2019, p. 064013. https://doi.org/10.1103/PhysRevApplied.11.064013.

[126] Siddiqui, F., and Gragston, M., "Multi-point FLEET velocimetry in a Mach 4 Ludwieg tube using a diffractive optical element," *Applied Optics*, Vol. 63, No. 4, 2024, pp. 1087–1093. https://doi.org/10.1364/AO.511803.

[127] Carter, D. W., Pehrson, J. C., Bhakta, R., Spillers, R., and Beresh, S. J., "Hypersonic FLEET Velocimetry on a Three-Dimensional Expansion-Compression Geometry," *AIAA SCITECH 2025 Forum*, 2025, p. 1838. https://doi.org/10.2514/6.2025-1838.

[128] Segall, B. A., Shekhtman, D., Hameed, A., Chen, J. H., and Parziale, N. J., "Profiles of streamwise velocity and fluctuations in a hypersonic turbulent boundary layer using acetone tagging velocimetry," *Experiments in Fluids*, Vol. 64, No. 6, 2023, p. 122. https://doi.org/10.1007/s00348-023-03647-2.

[129] Shekhtman, D., Hameed, A., Segall, B. A., Dworzanczyk, A. R., and Parziale, N. J., "Initial Shakedown Testing of the Stevens Shock Tunnel," *Proceedings of AIAA SciTech 2022*, AIAA 2022-1402, San Diego, California and Virtual Event, 2022. https://doi.org/10.2514/6.2022-1402.

[130] Segall, B. A., Keenoy, T. C., Parziale, N. J., and Shekhtman, D., "Towards Wall-Normal Fluctuation Measurements in a Mach 6 Turbulent Boundary Layer," *Proceedings of AIAA SciTech 2025*, AIAA-2025-2612, Orlando, Florida, 2025. https://doi.org/10.2514/6.2025-2612.

[131] Segall, B. A., Keenoy, T. C., Kokinakos, J. C., Langhorn, J. D., Hameed, A., Shekhtman, D., and Parziale, N. J., "Hypersonic Turbulent Quantities in Support of Morkovin's Hypothesis," *Nature Communications*, 2025.

[132] Hill, J. L., Hsu, P. S., Jiang, N., Grib, S. W., Roy, S., Borg, M., Thomas, L., Reeder, M., and Schumaker, S. A., "Hypersonic N2 boundary layer flow velocity profile measurements using FLEET," *Applied Optics*, Vol. 60, No. 15, 2021, pp. C38–C46. https://doi.org/10.1364/AO.417470.

[133] Webber, N., Edwards, S., and Gragston, M., "Hypersonic Transitional Boundary Layer Profile Measurements with Molecular Tagging Velocimetry," *Research Square - Preprint*, 2025.

[134] Andrade, A., Strasser, N. S., Posladek, K., Combs, C. S., and Glasby, R. S., "Hypersonic Wake Velocity Measurements Using Acetone Molecular Tagging Velocimetry," *AIAA Aviation Forum and Ascend 2024*, 2024, p. 4587. https://doi.org/10.2514/6.2024-4587.

[135] Zhang, Y., Richardson, D. R., Beresh, S. J., Casper, K. M., Soehnel, M., Henfling, J., and Spillers, R., "Hypersonic wake measurements behind a slender cone using FLEET velocimetry," *AIAA aviation 2019 Forum*, 2019, p. 3381. https://doi.org/10.2514/6.2019-3381.

[136] Firsov, A., Savelkin, K. V., Yarantsev, D. A., and Leonov, S. B., "Plasma-enhanced mixing and flameholding in supersonic flow," *Philosophical Transactions of the Royal Society A: Mathematical, Physical and Engineering Sciences*, Vol. 373, No. 2048, 2015. https://doi.org/10.1098/rsta.2014.0337.

[137] Erdem, E., and Kontis, K., "Experimental investigation of sonic transverse jets in Mach 5 crossflow," *Aerospace Science and Technology*, Vol. 110, 2021, p. 106419. https://doi.org/10.1016/j.ast.2020.106419.

[138] Danehy, P. M., Bathel, B. F., Calvert, N., Dogariu, A., and Miles, R. P., "Three-component velocity and acceleration measurement using FLEET," *AIAA 2014-2228. 30th AIAA Aerodynamic Measurement Technology and Ground Testing Conference. June*, 2014. https://doi.org/10.2514/6.2014-2228.

[139] Pandey, A., Casper, K. M., and Beresh, S. J., "Relaminarization effects in hypersonic flow on a three-dimensional expansion–compression geometry," *Journal of Fluid Mechanics*, Vol. 985, 2024, p. A25. https://doi.org/10.1017/jfm.2024.275.

[140] Mustafa, M. A., Hunt, M. B., Parziale, N. J., Smith, M. S., and Marineau, E. C., "Krypton Tagging Velocimetry (KTV) Investigation of Shock-Wave/Turbulent Boundary-Layer Interaction," *Proceedings of AIAA SciTech 2017*, AIAA-2017-0025, Grapevine, Texas, 2017. https://doi.org/10.2514/6.2017-0025.

[141] Mustafa, M. A., Parziale, N. J., Smith, M. S., and Marineau, E. C., "Amplification and structure of streamwise-velocity fluctuations in four shock-wave/turbulent boundary-layer interactions," *Proceedings of AIAA Aviation 2018*, AIAA-2018-3704, Atlanta, Georgia, 2018. https://doi.org/10.2514/6.2018-3704.

[142] Mustafa, M., Parziale, N., Smith, M., and Marineau, E., "Amplification and structure of streamwise-velocity fluctuations in compression-corner shock-wave/turbulent boundary-layer interactions," *Journal of Fluid Mechanics*, Vol. 863, 2019, pp. 1091–1122. https://doi.org/10.1017/jfm.2018.1029.

[143] Fisher, J. M., Meyer, T. R., and Slipchenko, M. N., "Grid-based femtosecond laser electronic excitation tagging for single-ended 2D velocimetry at kilohertz rates," *Applied Optics*, Vol. 60, No. 34, 2021, pp. 10714–10720. https://doi.org/10.1364/AO.432803.

[144] Zhang, Y., Marshall, G., Beresh, S. J., Richardson, D., and Casper, K. M., "Multi-line FLEET by imaging periodic masks," *Optics Letters*, Vol. 45, No. 14, 2020, pp. 3949–3952. https://doi.org/10.1364/OL.392779.

[145] Richardson, D., Zhang, Y., and Beresh, S. J., "Tomographic FLEET with a wedge array for multi-point three-component velocimetry," *Optics Letters*, Vol. 49, No. 4, 2024, pp. 846–849. https://doi.org/10.1364/OL.512052.

[146] Carter, D. W., and Beresh, S. J., "Linear Photodiode Arrays for Time-Domain FLEET Velocimetry in Hypersonic Flows," *21st International Symposium on Application of Laser and Imaging Techniques to Fluid Mechanics*, 2024. https://doi.org/10.55037/lxlaser.21st.11.

[147] Carter, D. W., Spillers, R., Pehrson, J. C., Bhakta, R., Richardson, D. R., and Beresh, S., "Development of time-domain femtosecond laser electronic excitation tagging via linear photodiode arrays," *AIAA SCITECH 2024 Forum*, 2024, p. 2324. https://doi.org/10.2514/6.2024-2324.

[148] Carter, D. W., and Beresh, S. J., "Time-domain velocimetry via femtosecond laser electronic excitation tagging," *Measurement Science and Technology*, Vol. 35, No. 11, 2024, p. 117005. https://doi.org/10.1088/1361-6501/ad7312.

[149] Webber, N., and Gragston, M., "Analysis of Tangent FLEET Velocimetry for High-Speed Axisymmetric Flow-Fields Using CFD Produced Synthetic Data," *AIAA SCITECH 2026 Forum*, American Institute of Aeronautics and Astronautics, 2026.